EUROPEAN ORGANIZATION FOR NUCLEAR RESEARCH

ALICE-PUBLIC-2021-004

ALICE physics projections for a short oxygen-beam run at the LHC

ALICE Collaboration*

Abstract

This document collects performance projections for a selection of measurements that can be carried out with a short O–O run during the LHC Run 3. The baseline centre-of-mass energy per nucleon–nucleon collision is $\sqrt{s_{\rm NN}} = 6.37$ TeV and measurement uncertainties are given for the integrated luminosity $L_{\rm int} = 1\ {\rm nb}^{-1}$. Some projections for p–O collisions are also included. These studies were presented at the CERN workshop on Opportunities of O–O and p–O collisions at the LHC [1, 2].

© 2021 CERN for the benefit of the ALICE Collaboration.
Reproduction of this article or parts of it is allowed as specified in the CC-BY-4.0 license.

---

*See Appendix A for the full list of Collaborations members.

Contents

1 Introduction

The observation in high-multiplicity proton–proton (pp) and proton–lead (p–Pb) collisions of several effects that closely resemble those seen in lead–lead (Pb–Pb) collisions, and which are attributed to collective behaviour in the quark–gluon plasma (QGP), has been one of the main unexpected findings of the LHC programme. These effects include azimuthal asymmetries in particle production and in the abundances and momentum distributions of the various hadron species, which are consistent with collective particle production patterns induced by interactions in presence of a QGP (see e.g. [3, 4]). However, measurements in high-multiplicity small-system collisions do not exhibit evidence within current experimental uncertainties of jet quenching arising from the in-medium interaction of energetic partons in dense matter, in sharp contrast to measurements in Pb–Pb collisions [5, 6]. Since jet quenching is a necessary consequence of QGP formation, this tension between physics pictures arising from measurements of soft and hard (high-Q^2) observables in small-system collisions is one of the key outstanding questions in the LHC heavy-ion programme.

In this context, a brief run with collisions of oxygen nuclei (^{16}O) during LHC Run 3 provides a significant and timely opportunity to explore the effects seen in high-multiplicity p–Pb collisions, with a system that has a similarly small number of participating nucleons and similar final–state multiplicity but with larger geometrical transverse overlap, thereby enhancing jet-quenching effects, which depend on path length.

In addition to searching for jet quenching effects, O–O collisions offer the possibility to study flow effects as well as particle and light-nucleus production in a multiplicity range that bridges pp and p–Pb on the low side, and Pb–Pb and Xe–Xe on the high side. Charm hadron and J/ψ production can likewise be used to search for the effects of a high-density strongly-interacting medium. The modest increase in the size of the particle production source with respect to pp and p–Pb collisions offers a new angle for the study of hadron–hadron interactions. Finally, a brief O–O run enables significant and interesting measurements of coherent and incoherent light vector meson production in ultra–peripheral collisions, and studies of diffractive processes.

The baseline centre-of-mass energy per nucleon–nucleon collision $\sqrt{s_{\rm NN}} = 6.37$ TeV of the run [7] is used for these projections [1]. Since the O–O collision energy in this baseline plan differs from that of the pp collision datasets collected in Runs 1–2 and foreseen for Run 3, the measurements that require comparison with pp collisions will have to use a reference from pp collisions constructed by interpolation between the recorded pp energies, or scaling the data from the closest available pp energy. Such interpolations are presented here for inclusive charged–particle, jet, D meson and J/ψ measurements. Discussion is underway concerning a run with O–O collision energy the same as that of the Pb–Pb in Run 3, for which a dedicated pp reference will be collected. This option would require longer accelerator preparation time for the O–O run [7].

The integrated luminosity expected for the O–O run ranges between the target requested by the experiments of 0.5 nb^{-1} and about 1 nb^{-1}, depending on the duration of the O–O fills in the LHC. The projections in this document assume an integrated luminosity of 1 nb^{-1}.

Selected projections for p–O collisions at $\sqrt{s_{\rm NN}} = 9$ TeV, which are proposed by the LHCb and LHCf Collaborations, are also included.

2 Search for jet quenching effects in O–O collisions

Jet quenching measurements in heavy–ion collisions are usually carried out as a function of event centrality. For such measurements, observables based on inclusive hadron or jet yields require the association of

---

[1] The baseline plan for the short O–O run utilizes the same beam optics configuration as that for the preceding Pb–Pb campaign in Run 3, which will have either $\sqrt{s_{\rm NN}} = 5.02$ TeV (corresponding to 6.37 TeV for O–O) or 5.5 TeV (corresponding to 7 TeV for O–O). In practice, this difference has negligible impact on the projections presented in this report.

event activity (EA) with collision geometry, in order to calculate the geometric scaling factor $\langle T_{\mathrm{AA}} \rangle$ for a specific centrality selection using Glauber theory. In ALICE, EA is measured using charged-particle multiplicity or total energy registered in a forward detector.

However, for small collision systems, the correlation between EA and collision geometry is weak, with significant contribution to EA from non-geometric sources such as conservation laws. The definition of centrality classes in small systems is therefore biased, imposing a limit on the systematic precision of jet quenching measurements carried out using observables based on inclusive yield suppression for centrality-selected data. Since jet quenching effects are expected to be small in small systems (see e.g. Ref. [8]), the limit in systematic precision imposed by these biases for inclusive observables may prevent conclusive observations from such measurement channels. It is therefore crucial to explore approaches that do not rely upon the assumption that EA is correlated with collision geometry. ALICE will address this issue in two ways in the O–O run:

- Comparison of inclusive hadron and jet transverse-momentum (p_{T}) differential cross sections $\mathrm{d}\sigma/\mathrm{d}p_{\mathrm{T}}$ in zero-bias O–O collisions (0–100% centrality) to those in pp collisions [9, 10], utilizing the A^2 scaling of high-Q^2 production cross sections in zero-bias A–A collisions. Inclusive yield modification due to jet quenching is then measured via suppression of R_{AA} relative to unity, where
$$R_{\mathrm{AA}}(p_{\mathrm{T}}) = \frac{1}{A^2} \frac{\mathrm{d}\sigma_{\mathrm{AA}}/\mathrm{d}p_{\mathrm{T}}}{\mathrm{d}\sigma_{\mathrm{pp}}/\mathrm{d}p_{\mathrm{T}}}. \tag{1}$$
The new capability of ALICE in Run 3 for continuous readout is essential for recording a strictly zero-bias event population (Sect. 4.1).

- Utilization of semi-inclusive observables such as hadron+jet coincidences [5]. Semi-inclusive observables are equivalent to the ratio of two hard cross sections, meaning that $\langle T_{\mathrm{AA}} \rangle$ cancels identically and does not play a role in the measurement. No assumption about the correlation between EA and collision geometry is therefore required in this approach (Sect. 4.2).

Jet quenching effects may be significantly larger in central than in zero-bias O–O collisions, due to the larger size of the collision zone. This increase in signal may be important for conclusive experimental observations; at minimum, centrality-selected analyses provide systematically different approaches to the search for jet quenching effects. Therefore, inclusive and coincidence measurements will also be carried out for high-EA (high centrality) selected data, which requires the assessment of selection bias and the additional systematic uncertainty that such a selection introduces.

Theoretical efforts are currently underway to assess the effects of nuclear modification of Parton Distribution Functions (nPDFs), and its uncertainties, on the experimental observables of jet quenching in small systems that are discussed here. Nuclear PDF effects are themselves interesting and important. However, disentangling nPDF and jet quenching effects will require a comprehensive approach from both the theoretical and experimental communities.

3 Cross section normalisation and event classification

In Run 3, most ALICE detector systems will support a continuous readout mode, in which data are shipped to the acquisition with no requirement of a trigger signal. The system is designed to perform efficiently for a data rate equivalent to a Pb–Pb interaction rate of 50 kHz [11]. For the expected instantaneous luminosity of O–O and p–O collisions in a pilot run during Run 3 [7], this continuous readout mode will be fully exploited.

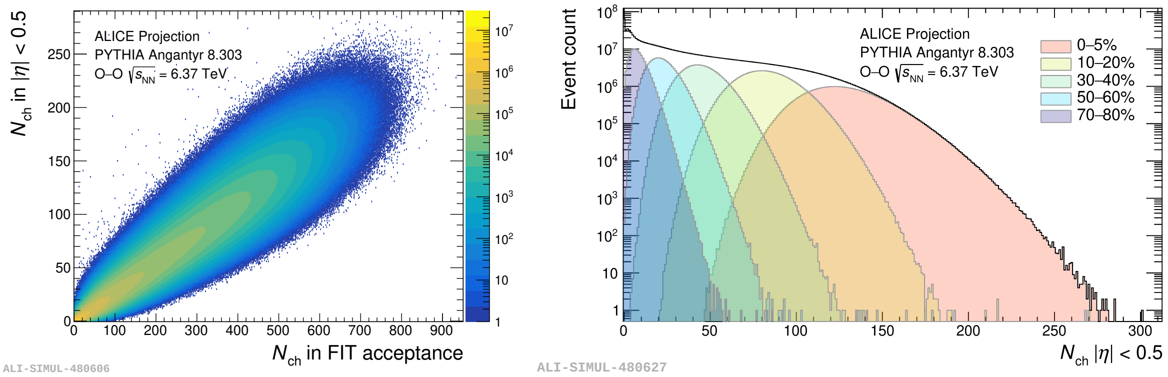

Fig. 1: Left: correlation between midrapidity and FIT-detector-acceptance charged-particle multiplicity obtained in PYTHIA Angantyr O–O simulations at $\sqrt{s_{\rm NN}}$ = 6.37 TeV. Right: midrapidity multiplicity distributions for event classes determined using sharp selections in the charged-particle multiplicity measured in the FIT detector acceptance.

When the centrality-integrated "zero-bias" nuclear modification factor $R_{\rm AA}$ is evaluated according to Eq. 1, the inclusive cross section for O–O collisions is measured, in contrast to the yield per minimum-bias nuclear collision in the standard definition of $R_{\rm AA}$ [2]. In the continuous readout mode, where a hardware minimum bias trigger is not required, the definition of Eq. 1 has a clear advantage, since it is not affected by the uncertainties deriving from the selection of minimum-bias hadronic events. However, this approach requires precise measurement of the integrated luminosity for both the O–O and pp datasets, for precise normalisation of the cross sections in the ratio. As discussed below, the target precision for this normalisation is about 2%. Such precision in integrated luminosity is achievable by means of a van der Meer scan [12], utilizing the cross section for a suitable reference process, which is then applied for luminosity normalisation. During Run 2, ALICE measured luminosity with a precision of about 2% for both p–Pb and Pb–Pb collisions [13, 14]. Similar precision may be achieved for p–O and O–O collisions, providing that sufficient time is allocated for the van der Meer scan. The typical duration of a van der Meer scan in ALICE is two to three hours. In addition, some cancellation of luminosity uncertainties in the ratio of O–O (or p–O) to pp cross sections may be possible. The projections presented in this document assume an integrated luminosity uncertainty of 2.5% for O–O and p–O collisions, and uncertainty of 3% in the inclusive cross section ratio for O–O (or p–O) relative to pp collisions.

For centrality-selected measurements, event selection will be performed using the signals measured in the FIT detectors, covering the pseudorapidity ranges $2.2 < \eta < 5.0$ and $-3.3 < \eta < -2.1$ (approximately, because the detector is not circular on the negative η side). Such a selection will correlate with the midrapidity charged-particle multiplicity density, as seen in PYTHIA Angantyr [15] O–O simulations in Fig. 1, and will result in significantly different charged-particle multiplicity distributions at midrapidity. Though the correlation between multiplicities measured in different rapidities is not as strong as in Pb–Pb collisions, it is still more pronounced than in p–Pb collisions, allowing for more reliable centrality estimation.

In order to study the nuclear modification factor in central O–O collisions, a crucial ingredient will be the precision with which Glauber quantities such as the average number of binary collisions, $\langle N_{\rm coll}\rangle$, and the average nuclear overlap function, $\langle T_{\rm AA}\rangle$, will be calculated. To estimate the associated uncertainties, the FIT detector signals were emulated using Glauber simulations coupled to an $N_{\rm ancestor}$ model in which each ancestor produces charged particles following a negative binomial distribution, similar to what was done in Pb–Pb collisions [17]. Final-state charged-particle multiplicity selections were then performed

---

[2] The "standard definition" reads $R_{\rm AA} = \frac{1}{\langle T_{\rm AA}\rangle}\frac{{\rm d}N_{\rm AA}/{\rm d}p_{\rm T}}{{\rm d}\sigma_{\rm pp}/{\rm d}p_{\rm T}}$, where ${\rm d}N_{\rm AA}/{\rm d}p_{\rm T}$ denotes the ($p_{\rm T}$-differential) yield per minimum bias A–A collision, $\langle T_{\rm AA}\rangle$ is the nuclear overlap function, and $\langle\ldots\rangle$ denotes the average over events in a centrality bin.

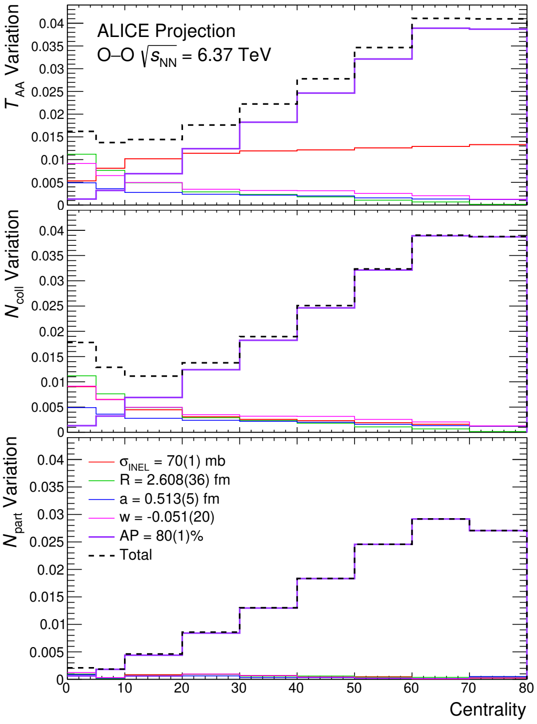

ALI-SIMUL-480461

Fig. 2: Estimated relative uncertainties on $\langle N_{\rm part}\rangle$, $\langle N_{\rm coll}\rangle$ and $\langle T_{\rm AA}\rangle$ as a function of centrality in O–O collisions at $\sqrt{s_{\rm NN}}$ = 6.37 TeV obtained using Glauber Monte Carlo, the ancestor model and the uncertainties in the Oxygen 3pF from Ref. [16]. R, a and w denote the parameters of the 3pF; AP denotes the fit anchor point; $\sigma_{\rm INEL}$ denotes the inelastic nucleon–nucleon cross section.

using this model and the corresponding $\langle N_{\rm part}\rangle$ and $\langle N_{\rm coll}\rangle$ were calculated using several variations of the Oxygen three-parameter (R, a, w) Fermi function (3pF) in the Glauber Model according to Ref. [16]. The nucleon–nucleon inelastic cross section at this centre-of-mass energy was taken to be $\sigma_{\rm INEL} = (70 \pm 1)$ mb [18, 19] and an uncertainty on the anchor point of the fit of the FIT multiplicity distribution was estimated by varying the anchor point (AP) by $\pm 1\%$ around the central values of 80%. The deviations observed in the $\langle N_{\rm part}\rangle$ and $\langle N_{\rm coll}\rangle$ in these calculations are shown in Fig. 2 and are of no more than 3% for the $\langle N_{\rm part}\rangle$ and 4% for the $\langle N_{\rm coll}\rangle$ and $\langle T_{\rm AA}\rangle$ in peripheral collisions, with considerably smaller values for progressively more central collisions. The calculation of a nuclear modification factor in the centrality interval 0–30% will have a $T_{\rm AA}$ normalisation uncertainty of about 1.5%.

Multiplicity fluctuations play an important role for centrality-selected measurements in O–O collisions. This is illustrated in Fig. 3, which shows the average charged-particle multiplicity divided by twice the average number of participant nucleons, $2\langle N_{\rm ch}\rangle/\langle N_{\rm part}\rangle$, measured in Xe–Xe and Pb–Pb collisions together with O–O predictions at $\sqrt{s_{\rm NN}}$ = 6.37 TeV. To highlight the effect of multiplicity fluctuations, PYTHIA Angantyr calculations are shown for two different selections: using a charged-particle multiplicity measurement at forward/backward rapidity and a selection on $N_{\rm part}$. While in Pb–Pb the difference between these two options is rather small, the multiplicity-based selection introduces a rapid increase in the case of very central Xe–Xe collisions. This behaviour is significantly more pronounced for O–O collisions, which only follow the trend from the other collision systems when using a $N_{\rm part}$ selection that can be tested only in simulations.

In addition, fluctuations may also have significant impact in the measurement of the nuclear modification factor. This can be estimated calculating the $R_{\rm AA}$ with a multiplicity-based centrality selection in HG-PYTHIA, a model in which PYTHIA is coupled to Glauber Monte Carlo such that it perfectly respects $N_{\rm coll}$-scaling [22]. The result, shown in Fig. 4 (left), suggests that deviations of $R_{\rm AA}$ from unity may

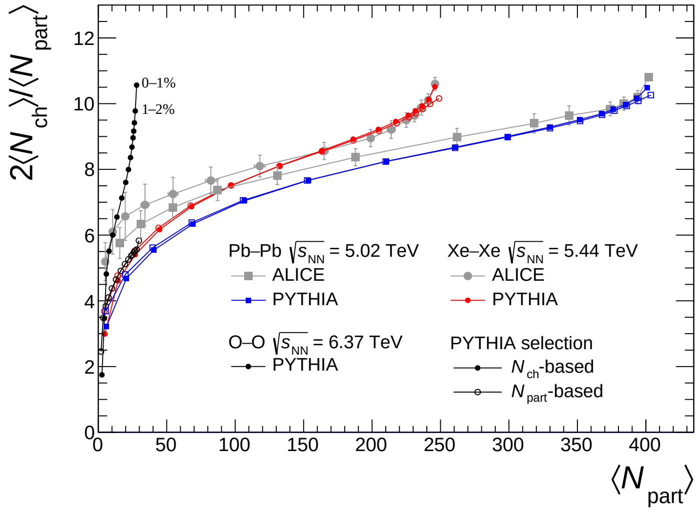

Fig. 3: Average charged-particle multiplicity per nucleon participant pair in O–O (projected using PYTHIA Angantyr), Xe–Xe and Pb–Pb collisions [20, 21]. For all collision systems, PYTHIA predictions are shown using two different event selection criteria: based on FIT-detector-acceptance charged-particle multiplicity and a $N_{\rm part}$ selection.

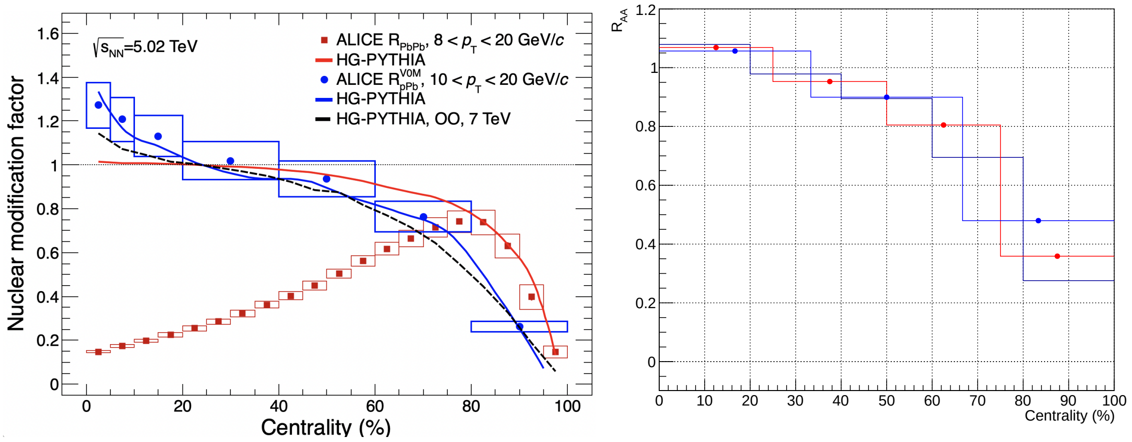

Fig. 4: Left: Estimate of the impact of centrality selection bias on the nuclear modification factor in O–O collisions (black dashed line), compared to p–Pb (blue line and data) and Pb–Pb collisions (red line and data), for the interval $8 < p_{\rm T} < 20$ GeV/c. The estimate was obtained with the HG-PYTHIA model [22]. Right: HG-PYTHIA estimate for O–O collisions with wide centrality classes. The three colours represent different possible choices of centrality classes.

arise simply because of event selection biases in very peripheral events, with an effect of up to -50% being observed in 80–90% collisions. Similarly to the rapid increase observed in Fig. 3, very central O–O collisions may also exhibit an R_{AA} above unity, though the effect at high momentum is significantly weaker than for integrated yields and is about $+15\%$ in 0–10% collisions. This upward bias in central collisions can be reduced to about 7% ($R_{\mathrm{AA}} \approx 1.07$) using a wider centrality class like 0–30%, as shown in Fig. 4 (right). This motivates the choice of this class, in addition to 0–100%, for the R_{AA} projections presented in the following.

The estimates of charged-particle multiplicity at midrapidity in O–O collisions that are used in the projections throughout this note are based on Fig. 3.

4 Projections for the jet quenching search

4.1 Inclusive charged-particle yield suppression

In heavy-ion collisions, energetic partons produced in the collision traverse the QGP and interact with it. This interaction generates observable modifications in the distributions of jets and hadrons relative to vacuum production in pp collisions (“jet quenching”). Among these effects is the medium-induced transport of energy to large angles relative to the jet axis, resulting in suppression in the rate of high p_{T} hadrons ($p_{\mathrm{T}} >$ few GeV$/c$) that are fragments of the jet close to its axis. For inclusive hadron production this suppression is measured using R_{AA} (Eq. 1). The inclusive yield of hadrons in AA collisions scales with the nuclear overlap function, $\langle T_{\mathrm{AA}} \rangle$, when compared to the corresponding inclusive production cross section in pp collisions, σ_{pp}. In the absence of nuclear effects, $R_{\mathrm{AA}} = 1$.

As noted in the Introduction, a reference spectrum from pp collisions at the same $\sqrt{s}$ as the O–O data may not be available, necessitating determination of the pp reference for R_{AA} measurements using interpolation or scaling of pp data at different centre-of-mass energies. In order to obtain the reference charged-particle inclusive p_{T} spectrum at $\sqrt{s} = 6.37\,\mathrm{TeV}$, the following approach is adopted. First, the Run 1 and 2 measurements in pp collisions at $\sqrt{s} = 2.76$, 5.02 and 7 TeV [6, 23] are parametrised as a function of $\sqrt{s}$ for each p_{T} bin. From this parametrisation, ratios of p_{T} spectra at $\sqrt{s} = 6.37$ and $5.02\,\mathrm{TeV}$ are calculated. The charged-particle spectrum measured at $\sqrt{s} = 5.02\,\mathrm{TeV}$ in Run 3 (first year, according to present plans) will be scaled by this ratio to obtain the reference at $\sqrt{s} = 6.37\,\mathrm{TeV}$.

At low p_{T} (< 10 GeV$/c$), the parametrisation uses the function $f(\sqrt{s}) = \alpha\sqrt{s}^{\beta}$, where α and β are free fit parameters. The systematic uncertainties related to the interpolation procedure are calculated by propagating the uncertainties of the fit parameters.

At high p_{T} (10–50 GeV$/c$), the aforementioned procedure becomes unreliable because the $\sqrt{s}$-dependence of the spectra becomes large. In this range, a combination of an empirical fit to the spectra and of perturbative QCD (pQCD) calculations is considered, as detailed in the following. The empirical fit uses the x_{T} quantity, defined as $x_{\mathrm{T}} = p_{\mathrm{T}}/(2\sqrt{s})$. The functional form for the fit is:

$$\sqrt{s}^{n} \frac{\mathrm{d}^2\sigma_{\mathrm{pp}}}{\mathrm{d}\eta\,\mathrm{d}x_{\mathrm{T}}}(x_{\mathrm{T}}, \sqrt{s}) = k \times x_{\mathrm{T}}^{a+b\sqrt{s}+cx_{\mathrm{T}}+dx_{\mathrm{T}}\sqrt{s}}\,, \tag{2}$$

where n, k, a , b, c, and d are free fit parameters. Eq. (2) provides a good description of the measured spectra for $p_{\mathrm{T}} > 10$ GeV$/c$, as shown in Fig. 5 (left).

The x_{T} function in Eq. (2) with the parameters from the fit is then used to calculate the cross section ratio at $\sqrt{s} = 6.37$ and $5\,\mathrm{TeV}$. This ratio is shown in Fig. 5 (right) by the green line, with the band around the line illustrating the propagated fit parameter uncertainties. This ratio from the x_{T} fit is found to be very close to the ratio obtained with NLO pQCD calculations using the BKK fragmentation functions [10] (red band in the figure, obtained from variation of the perturbative scales [10]); the two ratios differ by

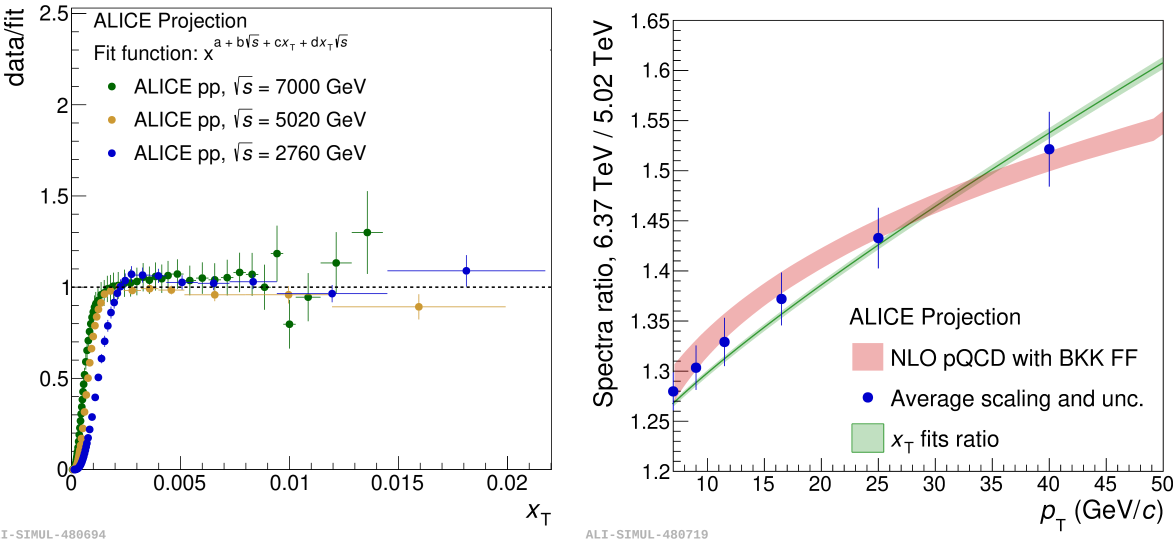

ALI-SIMUL-480694 ALI-SIMUL-480719

Fig. 5: Left: data-to-fit ratios of x_T-fits to charged-particle cross sections measured in pp collisions at 2.76, 5.02 and 7 TeV. Right: $d\sigma_{pp}/dp_T$ ratios at $\sqrt{s} = 6.37$ and 5 TeV from the interpolation procedure (green band), in comparison to the NLO pQCD calculations [10] (red band). Blue circles represent the average between interpolation and pQCD calculation and the blue bars represent their envelope.

only 2% at 10 GeV/c and 4% at 50 GeV/c. The central value of the scaling factor is chosen as the average of ratios from x_T fits and from the pQCD calculation.

The systematic uncertainty of the ratio consists of three components. First, the uncertainties on the ratios resulting from the x_T fitting procedure are estimated by propagating the parameter uncertainties. Note that part of the parameter uncertainties are correlated with $\sqrt{s}$ and thus partially cancel in the ratio. Second, the pQCD calculation has a significant uncertainty originating from the choice of perturbative scale (red band). Thus, half of the band width is taken as another source of the systematic uncertainty on the averaged ratio. Finally, half of the difference between the ratio of x_T fits and the pQCD ratio is taken as an additional source of systematic uncertainty. These uncertainties are shown in Fig. 6 (left) by the blue lines: the solid blue line is their quadratic sum for $p_T > 10$ GeV/c, while at lower p_T the interpolation uncertainty is obtained by propagating the parameter uncertainties of the interpolation function $f(\sqrt{s}) = \alpha\sqrt{s}^{\beta}$.

The other sources of uncertainties on the pp reference spectrum are those related to the measurement at 5.02 TeV (e.g. from the corrections for efficiency and subtraction of secondary particles), and those related to the cross section normalisation. For the former, shown by the red line in Fig. 6 (left), the systematic uncertainties on the measurement in pp collisions at 5.02 TeV (2017 run) [6] is used, noting that they are not expected to change significantly for a measurement in Run 3. For the latter, a value of 2.5% is considered, which is a typical uncertainty from van der Meer scans, as discussed in Sec. 3.

Figure 6 (right) reports the estimated uncertainties on R_{AA} for 0–100%. The total interpolation (or scaling) uncertainty is shown by the magenta line, which ranges between 2 and 3%. The measurement systematic uncertainty on the ratio of spectra in O–O and pp (blue line) is obtained by assuming that half of the measurement-related systematic uncertainty is fully correlated between pp and O–O measurement and cancels in the ratio, and half is uncorrelated and adds quadratically in the ratio. The uncertainty on the ratio of the vdM-determined cross sections in O–O and pp is also assumed to partly cancel in the ratio, as discussed in Sec. 3, resulting in a normalisation uncertainty on R_{AA} of 3%. The systematic uncertainties on R_{AA} in 0–30% O–O collisions are also estimated, noting the two key differences as compared to the 0–100% case. First, σ_{OO} becomes irrelevant and thus only the normalization uncertainty of 2.5% originating from pp reference is included. Second, uncertainty of 2.5% on the average nuclear overlap

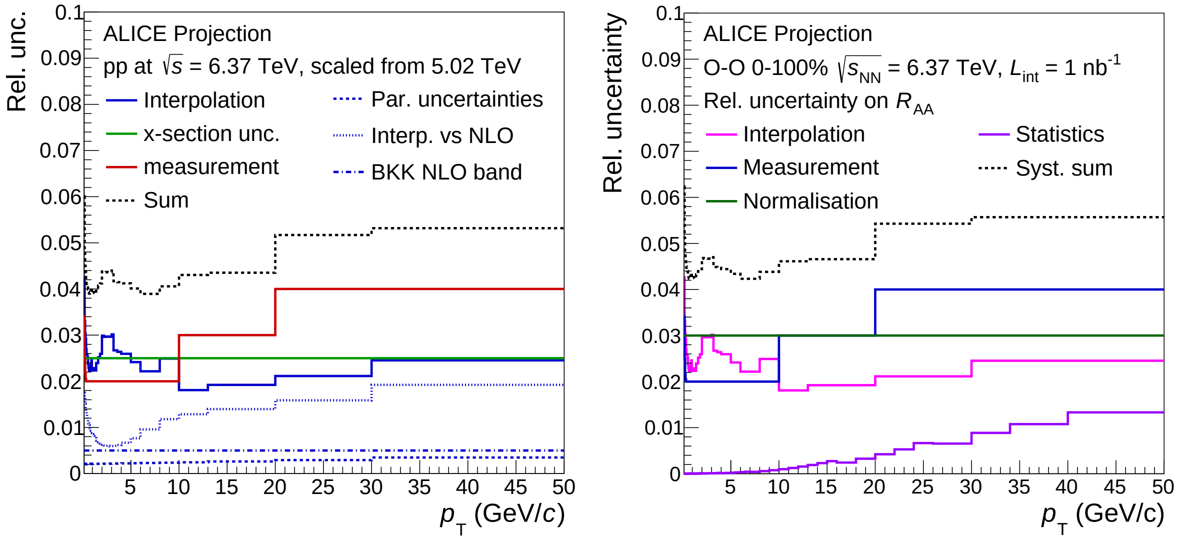

Fig. 6: Summary of systematic uncertainties on pp reference spectra ratio (left) and 0–100% R_{AA} (right). The purple line in the right panel also shows the estimated statistical uncertainty on the R_{AA}.

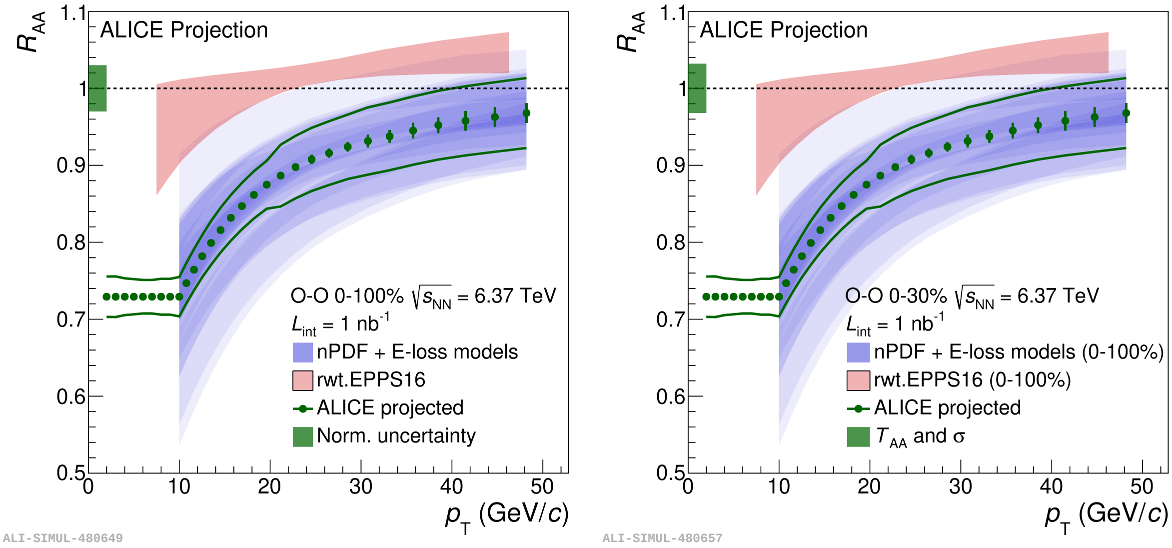

Fig. 7: Charged-particle R_{AA} in 0–100% (left) and 0–30% (right) O–O collisions at $\sqrt{s_{NN}} = 6.37$ TeV. Central values are calculated as averaged values of different energy loss models, shown by the blue bands. Energy loss model calculations and nPDF baseline with EPPS16 from [10]. Note that the model calculations and nPDF baseline calculated for 0–100% are also shown, for illustration, for 0–30%.

function is assigned, as discussed in Sec. 3. Note that an assessment of the selection bias discussed in Sec. 3 would result in an additional systematic uncertainty. This is not included in the projections, but should be considered for the interpretation of the future measurements.

Finally, the statistical uncertainties on R_{AA} are calculated considering integrated luminosities of 1 nb^{-1} for O–O and 3 pb^{-1} for pp collisions (ALICE plans to collect a sample of 3 pb^{-1} of pp collisions at 5.02 TeV during the first year of Run 3, to be used as a reference for the first Pb–Pb run). The calculated statistical uncertainty is found to be much smaller than the systematic uncertainties ($< 1.5\%$) up to the highest p_T interval considered, $40 < p_T < 50$ GeV$/c$ (purple line in Fig. 6 (right)).

The projections for the charged-particle R_{AA} as a function of p_T for 0–100% and 0–30% O–O collisions at $\sqrt{s_{NN}} = 6.37$ TeV are shown in Fig. 7 together with comparison to various energy loss models and to the baseline without energy loss and with only nuclear-modified parton distributions functions EPPS16 (all calculations are described in [10]). In the p_{T} range 20–25 GeV/c, where the uncertainties of the baseline without energy loss are smallest (about 2%), the uncertainties of the projection are about 5.5%, which includes the reference scaling uncertainty and the normalisation uncertainty. The possibility to observe a reduction of R_{AA} caused by energy loss will depend on the actual size of the effect.

4.2 Semi–inclusive hadron–jet recoil distributions

This section reports on the search for jet-quenching effects in O–O collisions using semi–inclusive hadron–jet distributions, which measure properties of jets recoiling from a high-p_{T} trigger hadron (denoted as trigger track or TT). The method applies a data–driven approach to remove the yield due to jet candidates that are uncorrelated with the high-p_{T} hadron trigger. Such uncorrelated backgrounds arise from multiple hard interactions in the same nuclear collision and from collision pileup in the detector. In the high multiplicity environment of nuclear collisions, uncorrelated jet background can also arise from purely combinatorial jets, whose constituents are generated by multiple independent soft interactions. A detailed description of the analysis method can be found in Ref. [5], where it was applied to search for jet quenching in p–Pb collisions.

This approach utilises two exclusive trigger hadron p_{T} intervals, which in this analysis have values 12–20 GeV/c and 6–7 GeV/c. These trigger hadron p_{T} intervals are denoted $\mathrm{TT_{Sig}}$ and $\mathrm{TT_{Ref}}$, respectively. Trigger hadrons have pseudorapidity $|\eta| < 0.9$. If multiple TT candidates are found in an event, one is selected by random. Jets are reconstructed from charged-particle tracks having $p_{\mathrm{T}} > 0.15$ GeV/c and $|\eta| < 0.9$ using the anti-k_{T} algorithm [24] with resolution parameter $R = 0.4$. The four-momenta of particles were combined using the boost invariant p_{T} recombination scheme. Jet p_{T} is corrected for the underlying event on an event-wise basis using the area-based approach [25].

Recoil jets in the azimuth opposite the TT are selected according to $|\Delta\varphi_{\mathrm{TT,jet}}| > \pi - 0.6\,\mathrm{rad}$ and $|\eta_{\mathrm{jet}}| < 0.5$; all recoil jets in the event are counted. The p_{T} spectrum of recoil jets for each TT bin is normalized per trigger, forming a semi-inclusive distribution. The observable Δ_{recoil} is then constructed [26],

$$\Delta_{\mathrm{recoil}} = \frac{1}{N_{\mathrm{trig}}} \frac{\mathrm{d}N_{\mathrm{jet}}}{\mathrm{d}p_{\mathrm{T,jet}}^{\mathrm{ch}}}\bigg|_{\mathrm{TT_{Sig}}} - c_{\mathrm{Ref}} \times \frac{1}{N_{\mathrm{trig}}} \frac{\mathrm{d}N_{\mathrm{jet}}}{\mathrm{d}p_{\mathrm{T,jet}}^{\mathrm{ch}}}\bigg|_{\mathrm{TT_{Ref}}}, \tag{3}$$

where the subtraction removes the jet yield which is uncorrelated to TT, and c_{Ref} is a factor close to unity that is determined from the data.

The semi-inclusive distribution in each term of Eq. 3 is equivalent to the ratio of the cross section to produce a high-p_{T} hadron together with a jet ($\sigma^{AA\to\mathrm{h+jet}+X}$) and the inclusive cross section to produce a high-p_{T} hadron in AA collision ($\sigma^{AA\to\mathrm{h}+X}$). In the absence of nuclear effects, the nuclear cross section corresponds to the product of the pp cross sections and the nuclear thickness function $\langle T_{AA}\rangle$,

$$\frac{1}{N_{\mathrm{trig}}^{AA}} \frac{\mathrm{d}N_{\mathrm{jet}}^{AA}}{\mathrm{d}p_{\mathrm{T,jet}}^{\mathrm{ch}}}\bigg|_{p_{\mathrm{T,trig}}\in\mathrm{TT}} = \frac{1}{\sigma^{AA\to\mathrm{h}+X}} \frac{\mathrm{d}\sigma^{AA\to\mathrm{h+jet}+X}}{\mathrm{d}p_{\mathrm{T,jet}}^{\mathrm{ch}}}\bigg|_{p_{\mathrm{T,h}}\in\mathrm{TT}} = \frac{1}{\langle T_{AA}\rangle\sigma^{\mathrm{pp}\to\mathrm{h}+X}} \frac{\langle T_{AA}\rangle\mathrm{d}\sigma^{\mathrm{pp}\to\mathrm{h+jet}+X}}{\mathrm{d}p_{\mathrm{T,jet}}^{\mathrm{ch}}}\bigg|_{p_{\mathrm{T,h}}\in\mathrm{TT}}. \tag{4}$$

The rightmost expression in Eq. 4 shows that the factors $\langle T_{AA}\rangle$ in numerator and denominator cancel identically. This approach therefore does not require calculation of the geometric Glauber scaling factor $\langle T_{\mathrm{AA}}\rangle$, thereby avoiding the assumption that EA is correlated with collision geometry. This approach applies even for centrality-selected data; it has been used to provide a constraint on jet quenching effects in high-EA relative to low-EA p–Pb collisions corresponding to medium-induced energy transport outside a cone of radius $R = 0.4$ of less than 400 MeV/c (90% CL) [5]. A suitable choice of ratios of Δ_{recoil} measurements results in significant cancellation of systematic uncertainties, yielding an observable that is systematically very precise. The measurement in [5] is strongly statistics-dominated, with systematic uncertainty ≈ 50 MeV/c for the limit on out-of-cone energy transport.

For O–O projections the differential h+jet production cross section, $\mathrm{d}\sigma^{\mathrm{pp}\to\mathrm{h+jet}+X}/\mathrm{d}p_{\mathrm{T,jet}}^{\mathrm{ch}}$, is generated for pp collisions using PYTHIA 8.234, Monash tune [27]. A projection for the semi-inclusive h+jet measurement for zero-bias (0–100%) O–O collisions at $\sqrt{s_{\mathrm{NN}}} = 6.37$ TeV is first made, to be compared to that for pp collisions at the same $\sqrt{s_{\mathrm{NN}}}$. For this purpose, the differential cross section generated by PYTHIA for pp collisions is scaled by the expected luminosity and A^2 (i.e. no jet quenching is assumed in O–O collisions) to give the projected mean number of counts per bin. The number of entries in each $p_{\mathrm{T,jet}}^{\mathrm{ch}}$ bin is then smeared, using a Poisson distribution to model statistical fluctuations. Scaling the PYTHIA-generated differential cross section by the integrated luminosity is equivalent to the experimental procedure of dividing the h+jet coincidence yield by the inclusive yield of the hadron trigger, with the additional assumption that the statistical jitter due to the inclusive trigger yield is negligible compared to that of the coincidence yield; in practice, this is an excellent approximation.

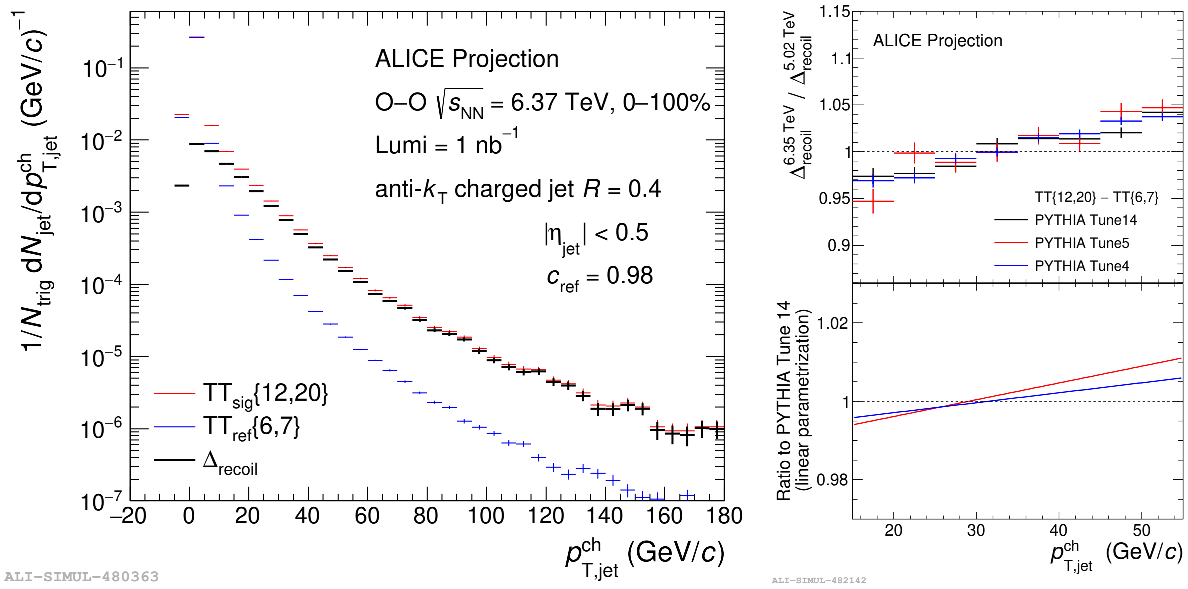

Fig. 8: Left panel: Per-trigger normalized yields of recoil jets associated to 12–20 GeV/c and 6–7 GeV/c trigger tracks. The corresponding Δ_{recoil} spectrum is in black. Recoil distributions were generated using PYTHIA 8 Monash tune. The statistical precision corresponds to O–O luminosity of 1 nb^{-1}. Right plot,top panel: $\Delta_{\mathrm{recoil}}^{\mathrm{pp}}|_{\sqrt{s}=6.37\,\mathrm{TeV}}/\Delta_{\mathrm{recoil}}^{\mathrm{pp}}|_{\sqrt{s}=5.02\,\mathrm{TeV}}$ ratios calculated with various PYTHIA8 tunes. Right plot, bottom panel: Linear parametrization of the double ratios obtained from the data shown in the top panel where the reference shape is given by the PYTHIA8 Monash. These parametrizations indicate how large an extrapolation error can be expected for a generator–based correction that extrapolates the shape of the Δ_{recoil} pp reference spectrum measured at $\sqrt{s} = 5.02$ TeV to $\sqrt{s} = 6.37$ TeV.

Figure 8 left panel, shows the projected recoil jet distributions for $\mathrm{TT_{sig}}\{12,20\}$ and $\mathrm{TT_{ref}}\{6,7\}$ GeV/c, together with the corresponding Δ_{recoil} distribution [5], for 0–100% O–O collisions at $\sqrt{s_{\mathrm{NN}}} = 6.37$ TeV with integrated luminosity of 1 nb^{-1}. As noted, no jet quenching is assumed in O–O collisions. The statistical sensitivity of the measurement to jet quenching effects is then determined by comparison of the ratio of the statistically-smeared O–O and pp spectra to unity.

In order to assess the statistical sensitivity to the magnitude of medium-induced energy transport to large angles, the assumption is made that the average magnitude of energy transported out-of-cone is independent of $p_{\mathrm{T,jet}}^{\mathrm{ch}}$. In the $p_{\mathrm{T,jet}}^{\mathrm{ch}}$ range 15–55 GeV/c, the Δ_{recoil} distributions of pp and O–O are approximated well by exponential functions, $\Delta_{\mathrm{recoil}}^{\mathrm{pp}} = a\exp\left[-p_{\mathrm{T,jet}}^{\mathrm{ch}}/b\right]$ and $\Delta_{\mathrm{recoil}}^{\mathrm{O-O}} = a\exp\left[-\left(p_{\mathrm{T,jet}}^{\mathrm{ch}} + \bar{s}\right)/b\right]$ respec-

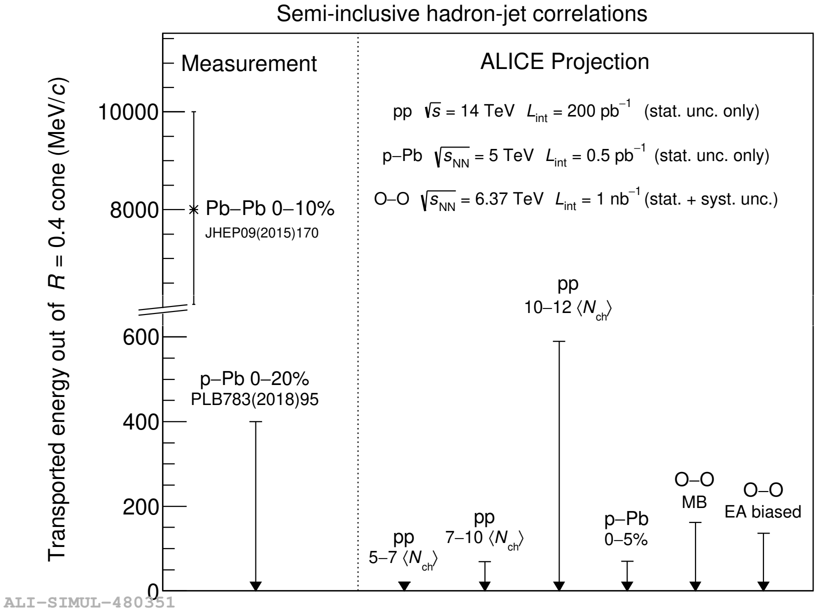

Fig. 9: $\Delta_{\rm recoil}$ spectrum shifts and limits from Run 1 and 2, and projection of 90% confidence level limits on minimal detectable medium-induced energy transport to angles $R > 0.4$ in small systems in Run 3 and 4 [28].

tively, with common fit parameters a and b. The ratio of the two functions is then expressed in terms of an average shift $\bar{s}$ in $p_{\rm T,jet}^{\rm ch}$ between the pp and O–O distributions, $\Delta_{\rm recoil}^{\rm O-O}\,/\,\Delta_{\rm recoil}^{\rm pp} = \exp\left(-\bar{s}/b\right)$, where the slope parameter b is determined by a fit of the $\Delta_{\rm recoil}^{\rm pp}$ spectrum and has value ≈ 11 GeV/c. Integrated luminosities of $1\,{\rm nb}^{-1}$ for the O–O dataset and $3\,{\rm pb}^{-1}$ for the pp dataset are considered (the latter corresponds to the target for the pp run at $\sqrt{s} = 5.02$ TeV that will be collected just before the first Pb–Pb run of Run 3). The statistical uncertainty of the energy shift is then about 0.037 GeV/c.

The reference pp spectrum at 6.37 TeV is obtained by scaling the measured pp spectrum at $\sqrt{s} = 5.02\,{\rm TeV}$. The systematic uncertainty of the extrapolated reference spectrum is obtained by comparing the $\Delta_{\rm recoil}^{\rm pp}|_{\sqrt{s}=6.37\,{\rm TeV}}/\Delta_{\rm recoil}^{\rm pp}|_{\sqrt{s}=5.02\,{\rm TeV}}$ ratios calculated by different PYTHIA8 tunes and is about 1%, see Fig. 8 (right). This translates to 0.11 GeV/c uncertainty on the shift.

Using the p–Pb analysis [5], the overall systematic uncertainty on $\bar{s}$ for the O–O measurements is estimated to be about 0.05 GeV/c. Since the $\Delta_{\rm recoil}$ distribution is well-approximated by an exponential function with $b \approx 11$ GeV/c (see above), this corresponds to a relative uncertainty in the ratio $\Delta_{\rm recoil}^{\rm O-O}\,/\,\Delta_{\rm recoil}^{\rm pp}$ of $0.05/11 \approx 0.5\%$. This small systematic uncertainty arises from the cancellation of many effects in the ratio. The dominant contributions to the systematic uncertainty in [5] arise from unfolding (relative contribution $\approx 40\%$), background density estimate ($\approx 35\%$), and tracking efficiency ($\approx 20\%$), with smaller contributions from $c_{\rm Ref}$ and binning effects.

Based on the statistical and systematic uncertainties of the energy shift, the one-sided 90% confidence level limit [5] for the minimum spectrum shift that can be detected at this level of precision is 0.162 GeV/c. From the theoretical standpoint, nuclear parton distribution function effects for this observable are expected to be smaller than for $R_{\rm AA}$, because it is the ratio of related quantities. However, residual nPDF effects may remain, and a quantitative theoretical assessment of such effects is needed.

A similar projection for the sensitivity to jet quenching effects can be obtained also from EA-selected O–O events. In this case the reference spectrum is taken from low-EA O–O collisions and no extrapolation of the pp spectrum is needed, thereby eliminating that source of systematic uncertainty. The expected systematic uncertainty is therefore ~ 0.05 GeV/c. Taking low-EA reference to be 50% of the events with the lowest EA and the high-EA signal to be 20% of the events with the highest EA, for $1\,{\rm nb}^{-1}$ O–O luminosity the statistical precision of the spectrum shift would be 0.094 GeV. The corresponding one–sided 90% confidence limit on the energy shift is 0.14 GeV/c. Figure 9 shows the measured energy shift or limits from Pb–Pb and p–Pb collisions in Runs 1–2, together with projections for different systems planned for measurements in Runs 3–4 [28].

A schematic comparison between the limits obtained from the inclusive charged-particle jet yield suppression and the semi-inclusive analysis can be made using an expression[3] that relates the spectrum shift with the nuclear modification factor, $R_{\mathrm{AA}} = (1+\bar{s}/p_{\mathrm{T}})^{-5.1}$. At p_{T} = 20 GeV/c, a spectrum shift of 160 MeV/c corresponds to R_{AA} of 0.96, which is closer to unity than most of the model predictions depicted in the band in Fig. 7. The semi-inclusive analysis therefore provides a precise measurement of the energy shift.

5 D meson nuclear modification factor and elliptic flow

The measurement of D-meson R_{AA} in O–O collisions will proceed similarly to the measurements of the nuclear modification factors in p–Pb and Pb–Pb collisions performed with Run 1 and Run 2 data (see e.g. [29, 30]). The analysis procedure consists of reconstructing the decay vertices of D-meson hadronic decay channels and exploiting their displacement from the primary vertex to reduce the combinatorial background. The signal raw yield (S) is extracted in each p_{T} interval considered via a fit to the invariant-mass distribution. The D-meson p_{T}-differential spectrum $\mathrm{d}N/\mathrm{d}p_{\mathrm{T}}$ is obtained by correcting the raw yield for the reconstruction, selection acceptance-times-efficiency (acc $\times\,\varepsilon$) and feed-down from beauty-hadron decays. The corrected spectrum is then divided by a pp-reference cross section scaled by the nuclear-overlap function, $\langle T_{\mathrm{AA}}\rangle$, to calculate R_{AA} in the selected centrality class. As for the case of charged particles, R_{AA} can be measured in zero-bias (0–100%) O–O collisions by normalising the spectrum in O–O to cross section per binary collision using the measured luminosity and dividing by A^2 (see Eq. (1)).

The statistical and systematic uncertainties on the D-meson R_{AA} in 0–100% O–O collisions at $\sqrt{s_{\mathrm{NN}}}$ = 6.37 TeV were estimated with the following procedure and assumptions. The statistical uncertainty on the D^0-meson $\mathrm{d}N/\mathrm{d}p_{\mathrm{T}}$ was estimated from the inverse of the expected statistical significance of the signal raw yield, $S/\sqrt{S+B}$, where B is the amount of combinatorial background with invariant mass M in the interval $|M - M_{\mathrm{D}^0}| < 3\ \sigma$ (σ represents the resolution on the signal invariant mass). The signal raw yield per event was calculated as the product of the expected p_{T}-differential spectrum $\mathrm{d}N/\mathrm{d}p_{\mathrm{T}}|_{\mathrm{O–O}}$ and an acceptance-times-efficiency factor ((acc $\times\,\varepsilon)_{\mathrm{O–O}}$. The spectrum was obtained by multiplying the D^0-meson cross section measured in pp collisions at $\sqrt{s} = 7$ TeV by the O–O average nuclear-thickness function $\langle T_{\mathrm{AA}}\rangle$, and by the R_{AA} predicted by R. Katz *et al.* [31] by interfacing the DAB-MOD model [32] with Trento [33] initial conditions and the v-USPhydro [34,35] code for a viscous-hydrodynamic medium expansion. The DAB-MOD model has two options for the heavy-quark evolution in the medium: one ("Energy loss") is based on a parametrisation of energy loss, including energy loss fluctuations, which is expected to work better for $p_{\mathrm{T}} > 6$ GeV/c, the second ("Langevin") is a relativistic Langevin model based on an input drag or diffusion coefficient, which is better suited for $p_{\mathrm{T}} < 6$ GeV/c. The predictions from the Langevin and Energy-loss options were used at low and high p_{T}, with an interpolation between the two in the interval $4 < p_{\mathrm{T}} < 6$ GeV/c to ensure a smooth transition of the R_{AA} p_{T} trend. In order to define reasonable values for $\varepsilon \times \mathrm{acc}_{\mathrm{O–O}}$ and for the background B, assumptions must be made about the expected amount of combinatorial background and the analysis selections that will be applied to reduce it, also taking into account that, after the ALICE long-shutdown 2 (LS2) upgrade, credit to the new ITS, the resolution on the track position at the primary vertex will improve by a factor 3–6. The combinatorial background depends mainly on the event multiplicity and p_{T}-differential spectrum of charged particles.

---

[3] This expression is obtained as a ratio of the AA high-p_{T} power-law spectrum $\mathrm{d}N/\mathrm{d}p_{\mathrm{T}} \sim (1/p_{\mathrm{T}})^n$ to the pp high-p_{T} $\mathrm{d}N/\mathrm{d}p_{\mathrm{T}} \sim (1/p_{\mathrm{T}}+\bar{s})^n$, assuming that the two spectra are shifted by $\bar{s}$ along the p_{T} axis. The exponent $n = 5.1$ is obtained by fitting the charged-particle p_{T} spectrum in pp collisions at $\sqrt{s} = 5.02$ TeV.

Given that the charged-particle multiplicity in 0–100% O–O collisions is similar to that in 0–10% p–Pb collisions, it is reasonable to consider selections similar to those applied for the measurement of the D^0 $Q_{\text{p–Pb}}$ in 0–10% p–Pb collisions [30] as a starting point for the analysis in O–O collisions. The $Q_{\text{p–Pb}}$ was measured in five centrality classes using the same analysis selections. The signal efficiency was found to be independent of the collision centrality. This indicates that effects related to the dependence of the primary-vertex reconstruction on the charged-particle multiplicity as well as occupancy effects on the tracking were not significant in the multiplicity range spanned, thus, can be neglected also for O–O estimates. For similar selections, one can assume that the different spatial resolution of ITS1 and ITS2 may result only on a modest modification of the signal $\varepsilon \times$ acc, because the distribution of the selection variables is determined by a convolution of a detector-resolution term with the intrinsic distribution. Although this expectation is not general and many exceptions are present, however, it supports the use of $(\varepsilon \times \mathrm{acc})_{\text{O–O}}$=$(\varepsilon \times \mathrm{acc})_{\text{0-10\% p–Pb}}$ as a reasonable working point. Considering that a dedicated optimisation of the selections will be done, also exploiting machine-learning classification techniques not used for the $Q_{\text{p–Pb}}$ analysis, this assumption is expected to yield a conservative estimate of the expected performance.

In order to estimate the background in O–O collisions from that in 0–10% p–Pb collisions, the variation of the background in the five centrality classes in which the $Q_{\text{p–Pb}}$ was measured was studied. It was verified that, with good approximation, B scales with N_{part}^2 for $p_{\mathrm{T}} < 5$ GeV/c, while at higher p_{T} it scales with N_{coll}. This trend can be explained by considering that at low p_{T} the background candidates are formed by tracks with moderate/low p_{T}, whose amount scales with $N_{\text{ch}} \propto N_{\text{part}}$ and the number of random associations of physically uncorrelated particles, not coming from the same hard scattering, exceeds that of pairs of particles from the same jet or hard scattering. Vice-versa, the latter contribution dominates at high p_{T} and the background scales with the number of jets, which scales as $R_{\text{AA}} \times N_{\text{coll}}$. The p_{T} at which the transition occurs is system dependent. However, the low and high p_{T} scaling factors obtained for scaling 0–10% p–Pb to 0–100% O–O are not too different, because of the similar N_{coll} and N_{part} values of the two collision systems. Therefore, a smooth transition between them around $p_{\mathrm{T}} = 5$ GeV/c was assumed. The improvement on background rejection provided by the new ITS was estimated to be within a factor 2 and 5, the latter value determined from the studies on the variation of the signal-to-background ratio in Pb–Pb collisions reported in the Technical Design Report of the new ITS [36]. Given that also this factor can vary significantly with collision system, the value 2 was chosen for the estimate of the R_{AA} in O–O, to explore a pessimistic scenario as a default one. The same factor was used also for the interval $p_{\mathrm{T}} < 1$ GeV/c in which the p–Pb analysis was performed without topological selections, assuming that the new ITS will improve the low-p_{T} reach of the analysis with vertex reconstruction.

The values of S and B obtained were then scaled by the number of events (1.3×10^9) corresponding to an integrated luminosity $L_{\text{int}} = 1\ \text{nb}^{-1}$ and an inelastic O–O cross section $\sigma_{\text{O–O}} = 1.3$ b to calculate the statistical significance. The statistical uncertainty obtained is smaller than 1% in the interval $1 < p_{\mathrm{T}} < 12$ GeV/c, negligible with respect to the systematic uncertainties described in what follows. Given that this conclusion was obtained with rather conservative assumptions, a further refinement of the estimate was deemed unnecessary.

The systematic uncertainty on the O–O $\mathrm{d}N/\mathrm{d}p_{\mathrm{T}}$ was estimated on the basis of the values reported in most recent ALICE measurements in pp and p–Pb collisions [30, 37–39]. The main systematic uncertainties expected are those deriving from the invariant-mass fit ("yield extraction"), from the $(\varepsilon \times \mathrm{acc})_{\text{O–O}}$ correction for the topological selections ("Cut variation") and tracking efficiency, and from the subtraction of the feed-down from b-hadron decays. For most of these uncertainties, the upgraded detector will not allow for a drastic reduction. However, the smaller values reported in the cited articles were chosen for the yield-extraction and the cut-variation uncertainties assuming that the high-statistics samples of pp, p–Pb, and Pb–Pb collisions that will be collected in run 3 will allow for a better evaluation of these uncertainties, ultimately resulting in dedicated correction procedures. The usage of data-driven methods

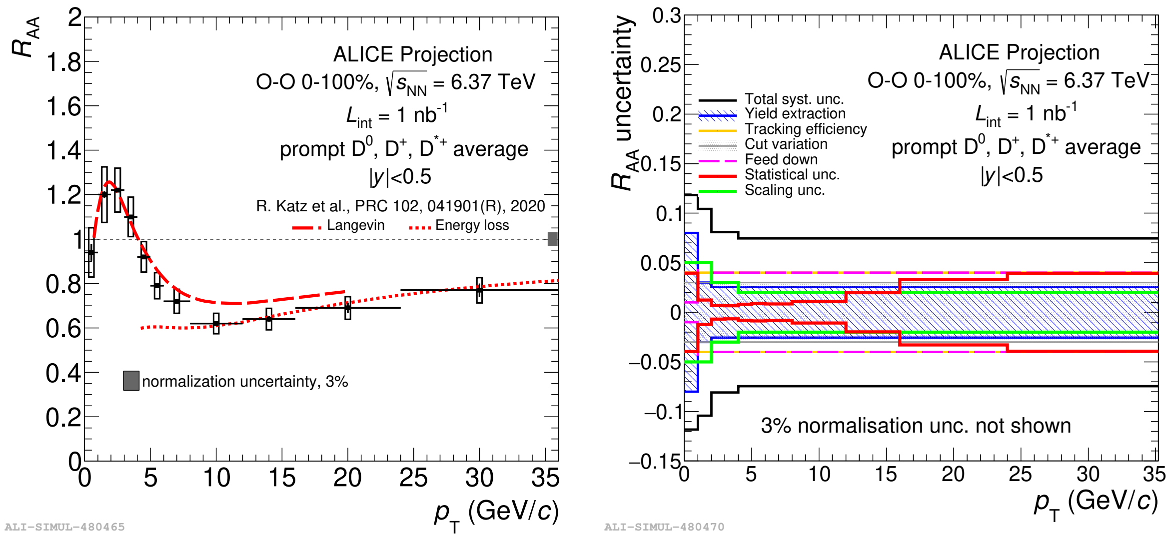

Fig. 10: Expected performance on the D-meson R_{AA} in 0–100% O–O collisions (left panel) and breakdown of its uncertainties (right panel).

in O–O collisions and the precise measurement of the cross section of D mesons from beauty-hadron decay in pp collisions at $\sqrt{s} = 5$ TeV, similarly to what was done in [37], should allow to limit also the uncertainty on the feed-down subtraction. The uncertainty on the tracking efficiency was assumed to be 2% per track.

For the computation of the D^0-meson R_{AA}, it was assumed that the pp cross-section reference will be obtained by scaling in $\sqrt{s}$ the D^0-meson cross section that will be measured with high precision in Run 3 from a sample of $L_{int} = 6$ pb^{-1} of pp collisions at $\sqrt{s} = 5$ TeV. The ratio of the cross sections predicted at $\sqrt{s} = 6.37$ TeV and $\sqrt{s} = 5.02$ TeV with the FONLL calculation [40, 41], which well reproduces D-meson cross sections at central and forward rapidity at several collision energies, from $\sqrt{s} = 2.76$ TeV to $\sqrt{s} = 13$ TeV [38, 39, 42–45], can be used to scale the cross section measured at $\sqrt{s} = 5$ TeV. The uncertainty on the scaling factor was estimated from the uncertainty on the ratios of the FONLL cross sections at $\sqrt{s} = 8, 7$ and 5 TeV ($\sigma_{8\ \mathrm{TeV}}/\sigma_{5\ \mathrm{TeV}}$, $\sigma_{7\ \mathrm{TeV}}/\sigma_{5\ \mathrm{TeV}}$, and $\sigma_{8\ \mathrm{TeV}}/\sigma_{7\ \mathrm{TeV}}$), obtained by varying the calculation parameters (charm-quark mass, factorisation and renormalisation scales, and PDFs) and assuming, for each variation, the deviations obtained at the numerator and denominator as fully correlated. The resulting uncertainty decreases from 5% for $p_T < 1$ GeV/c to 2% for $p_T > 4$ GeV/c. The statistical uncertainty on the pp reference will be negligible with respect to that on the O–O dN/dp_T. For the systematic uncertainties, values similar to those estimated for O–O collisions can be assumed. However, the systematic uncertainties on the pp and O–O collision measurements will be correlated and partly cancel in the R_{AA}. In particular, a 50% correlation was assumed on the uncertainties on the cut variation and the tracking efficiency, with the implicit assumption that the detector conditions will be similar during the pp and O–O data taking periods. For the feed-down subtraction, the uncertainty was estimated directly on the R_{AA} based on previous measurements in p–Pb collisions [30]. Finally, a 3% uncertainty, independent of p_T, due to the uncertainty on the pp-reference luminosity was considered.

The D-meson R_{AA} will be obtained as a weighted average of the D^0-, D$^+$- and D^{*+}-meson measurements, using the species-uncorrelated part of the uncertainty, which includes the statistical uncertainty and yield-extraction systematic uncertainty, as weight. Figure 10 shows the expected performance on the D-meson R_{AA} (left panel) and the breakdown of its uncertainties (right panel). The measurements of D$^+$ and D^{*+} R_{AA} will have uncertainties similar to those of the D^0 R_{AA} with slightly worse values for the statistical and tracking-efficiency contributions. It was assumed that by measuring the three D-meson species and averaging their R_{AA} a reduction of the species-uncorrelated part of the systematic uncertainty by a factor

$1/\sqrt{2}$ can be achieved with respect to the measurement of the D^0 meson only. The $1/\sqrt{2}$ factor was chosen to take into account that the uncertainty on the D^0 meson measurement might be slightly smaller than that on D^+ and D^{*+} measurements. This choice, although it is based on Run 1 and Run 2 analysis experience, is likely a conservative one because even for D^+ and D^{*+} the statistical uncertainty will probably be smaller than the uncertainty on the yield extraction, which will be similar for the three D-meson species. The other sources of systematic uncertainties were considered as fully correlated in the average.

Two-particle correlations (2PC) can be used for the D-meson v_2 measurements in rapidity interval $|y| < 0.5$ in O–O collisions. With this technique, the D-meson v_2 is obtained by fitting the azimuthal-correlation function of D mesons and charged particles (indicated by the symbol "ch" in what follows), i.e. the distribution of the azimuth difference $\Delta\varphi = \varphi_{\mathrm{ch}} - \varphi_{\mathrm{Dmeson}}$ normalised by the yield of D mesons, after the contributions of background D-meson candidates and of the jets are subtracted. The performance was studied for the D^0 meson and assumptions were made on the reduction of the uncertainties derived by averaging the D^0, D^+ and D^{*+} measurements. The procedure adopted for estimating the performance for the D^0 meson consists in studying the distribution of the v_2 residuals ($v_{2\mathrm{fit}} - v_{2\mathrm{input}}$) obtained by repeating the analysis procedure several times, where $v_{2\mathrm{input}}$ is the value set as input to generate the distributions of pseudodata. The procedure includes the subtraction of jet and background contributions on template distributions of the signal and background correlation functions and defined independently for 0–80% and 80–100% collisions. The correlation function in 80–100% is used to subtract the jet contribution. All template distributions are smeared each time according to Poisson statistics. From a Gaussian fit to the v_2-residual distribution the statistical uncertainty on the D^0 v_2 measurement is estimated. Systematic uncertainties can be investigated as well, as described below.

In each considered D^0-meson p_{T} interval, the azimuthal-correlation function of D^0 candidates with invariant mass $|M - M_{\mathrm{D}^0}| < 2\,\sigma$ and charged particles with $p_{\mathrm{T}} > 0.3$ GeV$/c$ and pseudorapidity η such that $|\Delta\eta| = |\eta_{\mathrm{ch}} - \eta_{\mathrm{D}}| < 1$ was assumed to be composed of the following terms

$$\left.\frac{\mathrm{d}N^{\mathrm{ch.}}}{\mathrm{d}\Delta\varphi}\right|^{\mathrm{Sig+Bkgr}} = \frac{S}{T}\left(\left.\frac{\mathrm{d}N^{\mathrm{ch.}}}{\mathrm{d}\Delta\varphi}\right|^{\mathrm{Sig}}_{\mathrm{jet}} + b(1 + v_{2\Delta}^{\mathrm{Sig}}\cos(2\Delta\varphi))\right) + \frac{B}{T}\left(\left.\frac{\mathrm{d}N^{\mathrm{ch.}}}{\mathrm{d}\Delta\varphi}\right|^{\mathrm{Bkgr}}_{\mathrm{jet}} + b(1 + v_{2\Delta}^{\mathrm{Bkgr}}\cos(2\Delta\varphi))\right). \tag{5}$$

In the above equation, S and B are the signal and background yields in the selected invariant-mass window, $T = S + B$, the "jet" correlation functions represent the near-side ($\Delta\varphi \sim 0$) and away-side ($\Delta\varphi \sim \pi$) correlation peaks, typically induced by charged particles in the jets originated by the same hard-scattering that produced the signal (Sig) or background (Bkgr) D-meson candidate. These peaks emerge on top of a baseline of height b, that is modulated by a flow term, $v_{2\Delta}^{\mathrm{Sig\ [Bkgr]}}\cos(2\Delta\varphi)$, with $v_{2\Delta}^{\mathrm{Sig\ [Bkgr]}} = v_2^{\mathrm{Sig\ [Bkgr]}} \cdot v_2^{\mathrm{ch}}$. The data-like signal+background template (Sig+Bkgr) of the azimuthal correlation function is obtained by summing a signal and a background template resulting by adding a v_2-modulated baseline to a template representing the jet correlation function. The signal jet correlation function was obtained from Monte Carlo simulations of pp collisions at $\sqrt{s} = 6.5$ TeV performed with the Monash 2013 [27] tune of PYTHIA8.243 event generator [46], which reproduces well the azimuthal correlation functions of D mesons and charged particles measured in pp collisions at $\sqrt{s} = 5.02$ and 7 TeV as well as in p–Pb collisions at $\sqrt{s_{\mathrm{NN}}} = 5.02$ TeV [47, 48]. The baseline, estimated as the average of the two lower values in the transverse region far from the peaks, was subtracted. The jet correlation function for the background was obtained by scaling the signal one, after subtracting the baseline, by a factor of two, to account for the typically larger associated yield of background candidates. The peak widths, which also are different for signal and background, were not modified because the high S/B ratio expected should make the measurement performance not too sensitive to the shape of the background correlation peaks. The same jet correlation functions were used for 0–80% and 80–100% O–O collisions. The values b of the baselines in Eq. (5) were estimated by scaling, with N_{part}, the values measured in 0–20% (60–100%) p–Pb collisions for 0–80% (80–100%) O–O collisions. For 0–80% collisions $v_2^{\mathrm{ch}} = 0.07$ was assumed for charged

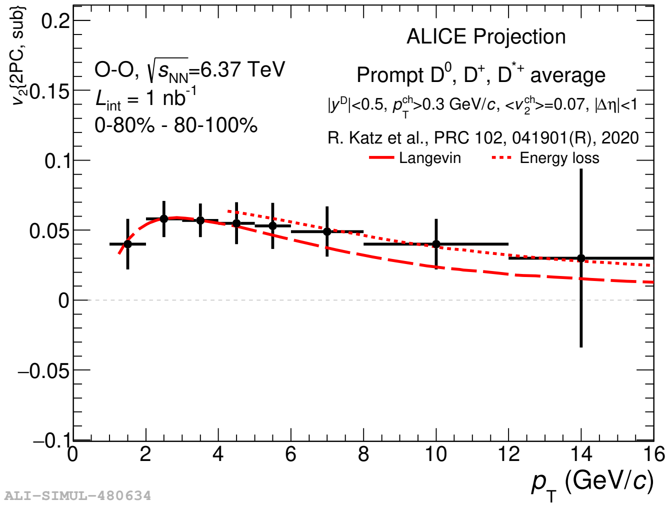

Fig. 11: Projection for the measurement of D-meson v_2 in 0–80% O–O collisions with two-particle azimuthal correlation (2PC) method and subtraction of the non-flow correlation from 80–100% central collisions.

particles, while the values predicted in [31] for 30–50% O–O collisions were assumed for $v_2^{\rm Sig}$ (shown in Fig. 11). For background D-meson candidates both $v_2^{\rm Bkgr} = v_2^{\rm ch}$ and $v_2^{\rm Bkgr} = (v_2^{\rm ch})^2$ were tested. The signal and background yields, S and B, for 0–80% O–O were estimated similarly to the $R_{\rm AA}$ case. For the background yields in 80–100% O–O the values observed in 60–100% p–Pb collisions were used as a starting point. Different from the $R_{\rm AA}$ case, a factor 5 reduction of the background (with credit to the new ITS) was used because the systematic uncertainties of the Monte Carlo corrections are typically smaller or negligible for v_2, allowing for the usage of more "aggressive" selections to reduce the statistical uncertainty. A pure-background template representing the correlation function obtained from sideband candidates with invariant mass $4\ \sigma < |M - M_{\rm D^0}| < 8\ \sigma$ is also constructed. Except for the different normalisation, this template is identical to that representing the background correlation function in the invariant-mass signal peak. It should be noted that the charged-particle tracking efficiency and the pair acceptance were not accounted for. They both imply a reduction of the number of reconstructed pairs but the effect is expected to be smaller than 20% for $|\Delta\eta| < 1$. The four templates (signal+background and sidebands in 0–80% and 80–100%) obtained are smeared independently according to Poisson statistics. Then, for both 0–80% and 80–100% centrality ranges, the sideband templates are subtracted from the signal+background templates. The background yield B used to normalise the sideband template to the background in the invariant-mass peak region was smeared to reflect the statistical uncertainty expected on its determination from the invariant-mass fit. The resulting distribution in 80–100%, after calculating and subtracting its baseline, is subtracted from that in 0–80% in order to remove the jet contribution. The remaining distribution is fitted with the function $b_{\rm fit}(1 + v_{2\Delta\,\rm fit}^{\rm Sig})$. The $v_{2\Delta\,\rm fit}^{\rm Sig}$ value is divided by $v_2^{\rm ch}$, assumed to be known with negligible uncertainty from independent measurements, to obtain $v_{2\rm fit}$. The smearing and fitting procedure is repeated 200 times.

The statistical uncertainty estimated from the $(v_{2\rm fit} - v_{2\rm input})$ residual distribution for the D^0 meson is divided by a factor $\sqrt{2}$ (in analogy to what was done for $R_{\rm AA}$) to account for the improvement in precision from averaging the measurement of D^0, D$^+$, and D^{*+} mesons. The projection for the D-meson average v_2 measurement is shown in Fig. 11. The main source of systematic uncertainty is expected to be the D-meson yield extraction, which affects the background subtraction. It was verified that by changing the value of the background yield used to normalise the sideband templates before subtraction within the expected yield-extraction uncertainty the effect on $v_{2\rm fit}$ was smaller than the estimated statistical uncertainty. It must be noted that in the above procedure the feed-down contribution was neglected. This contribution is not expected to affect significantly the estimate of the statistical uncertainty but it can be a source of systematic uncertainty. This should be further studied in the future. However, it is reasonable to assume that selections aimed at reducing significantly the non-prompt D-meson fraction can be applied with relatively high efficiency for the prompt component.

6 J/ψ production

The study of the J/ψ production in heavy-ion collisions provides an important insight into the properties of the QGP. In the QGP medium, the color force responsible for the binding of heavy-quarks is expected to experience a Debye-like screening, leading to a suppression of the J/ψ production compared to binary-scaled proton–proton collisions [49]. While this original idea is based on purely-real model potentials, more recent developments [50] have demonstrated that the heavy-quark potential at first non-trivial order in resummed perturbation theory gives rise also to an imaginary part. The latter can be interpreted as related to the dissociation originating from the inelastic scatterings of the $c\bar{c}$ pair with the constituents of the deconfined medium or to colour rotations of the pair leading to its dissociation. At the LHC energies, the large production cross section of charm quarks leads to the (re)generation of J/ψ via statistical recombination at the phase boundary [51] or through coalescence of charm quarks in the QGP medium [52]. Furthermore, if charm quarks thermalise in the QGP, the regenerated J/ψ would inherit their flow and thus participate in the collective motion of the system [53]. The simultaneous study of the production yields and the elliptic flow of J/ψ in collisions with oxygen nuclei can represent a powerful tool for investigating whether a deconfined medium is formed in small collision systems.

The expected yields of reconstructed inclusive J/ψ via the dielectron decay channel at midrapidity ($|y| < 0.9$) are estimated in O–O collisions at $\sqrt{s_{\mathrm{NN}}} = 6.37$ TeV and in p-O collisions at $\sqrt{s_{\mathrm{NN}}} = 9$ TeV as follows. The corresponding p_{T}-differential cross sections in proton–proton collisions, obtained through an interpolation procedure similar to the one described in Ref. [54], are scaled by the number of nucleon–nucleon collisions in the centrality classes 0–10% and 10–40%, estimated using a Glauber Monte Carlo model [19]. Due to the lack of available models, the nuclear modification factor R_{OO} is assumed to be the same as the one measured in most peripheral Pb–Pb collisions at $\sqrt{s_{\mathrm{NN}}} = 5.02$ TeV [55]. The $R_{\mathrm{pO}} = 1$ hypothesis is considered for p–O collisions. An acceptance-times-efficiency p_{T}-independent correction factor of 10% is used in the simulation. This value corresponds to the average one observed in the Pb–Pb Run 2 analyses. In order to estimate the expected performance of the signal extraction, an assumption is needed also for the signal-to-background ratio. In particular, the ratio in most central O–O collisions is assumed to be the same as the one observed in most peripheral Pb–Pb collisions at $\sqrt{s_{\mathrm{NN}}} = 5.02$ TeV. Instead, for semi-central and minimum bias O–O collisions, an average between the values in p–Pb collisions and most peripheral Pb–Pb collisions, both at $\sqrt{s_{\mathrm{NN}}} = 5.02$ TeV, is employed. A similar procedure is used for p–O collisions, where the signal-to-background ratio is obtained via an interpolation between the corresponding values in p–Pb and proton–proton collisions.

The expected systematic uncertainties of the measured yields in O–O and p–O collisions are estimated conservatively by assuming a similar performance as in Run 2 measurements in Pb–Pb and p–Pb collisions at $\sqrt{s_{\mathrm{NN}}} = 5.02$ TeV. Three main contributions have been considered:

- uncertainty from tracking, currently mainly dominated by the ITS-TPC matching efficiency. In O–O collisions it ranges between 5% and 10%, depending on p_{T} and centrality. In p–O collision it is at most 3%;
- particle identification (PID) of electrons, based on $\mathrm{d}E/\mathrm{d}x$ measurements in the TPC, assuming a data driven approach for determining the PID efficiency: this technique, used in Run 2 analyses, leads to a reduction of the corresponding systematic uncertainty compared to the one obtained when PID efficiency is evaluated based on Monte Carlo simulations. The corresponding value is below 1% for $p_{\mathrm{T}} < 5$ GeV/c and it increases at higher p_{T}, reaching 5% at $p_{\mathrm{T}} = 11$ GeV/c;

- signal extraction from the invariant-mass fit, estimated from proton–proton collisions at $\sqrt{s}$ = 13 TeV, where this systematic uncertainty is the lowest among all Run 2 analyses. It is about 2.5% at low p_{T} and 1.5% above 5 GeV/c.

The performance expected for the J/ψ R_{AA} measurement at midrapidity in O–O collisions at $\sqrt{s_{\mathrm{NN}}}$ = 6.37 TeV, assuming $L_{\mathrm{int}} = 1$ nb^{-1}, is shown in Fig. 12 for the centrality ranges 0–10% (left panel) and 10–40% (right panel). The error bars represent the statistical uncertainties, whereas boxes represent the systematic uncertainties on the yields measured in O–O collisions. The red shadowed area represents the uncertainty of the pp reference, as derived from the interpolation procedure. Inclusive J/ψ cross section measurements from PHENIX at $\sqrt{s}$ = 0.2 TeV [56], CDF at $\sqrt{s}$ = 1.96 TeV [57] and ALICE at $\sqrt{s}$ = 2.76, 5.02 and 7 TeV [58–60] are included in the interpolation procedure. Furthermore, preliminary J/ψ cross section measurements performed by ALICE at midrapidity at $\sqrt{s}$ = 13 TeV were also used. The resulting systematic uncertainty of the pp reference is about 4% below 6 GeV/c, and about 9% at higher p_{T}. The grey box plotted around unity on the right-hand side of each panel corresponds to the expected normalisation uncertainty from the estimation of the average nuclear overlap function.

The projections for the inclusive J/ψ production cross section in minimum bias p–O collisions at $\sqrt{s_{\mathrm{NN}}}$ = 9 TeV, corresponding to $L_{\mathrm{int}} = 5$ nb^{-1}, are shown in Fig. 13. The left-hand panel shows the relative uncertainties expected on the cross section measurement. Error bars (boxes) represent the expected statistical (systematic) uncertainties. The global systematic uncertainty of 2.5% on the normalisation, related to the luminosity determination via van der Meer scans, is represented by the shadowed area. The expected value of the inclusive J/ψ cross section in p–O collisions can be obtained by scaling the corresponding cross section in proton–proton collisions at the same centre-of-mass energy by the average number of binary collisions. The expected cross section for inclusive J/ψ in p–O collisions at $\sqrt{s_{\mathrm{NN}}}$ = 9 TeV is shown in the right-hand panel of Fig. 13, with statistical and systematic uncertainties, represented respectively by error bars and boxes. The normalisation uncertainty is quoted on the plot and not included in the boxes.

A similar strategy is adopted for the estimation of the expected yield for J/ψ decaying to a $\mu^{+}\mu^{-}$ pair in the forward rapidity region ($2.5 < y < 4$). For the dielectron channel, the p_{T}-differential proton–proton cross section at $\sqrt{s}$ = 6.37 and 9 TeV is obtained via an interpolation procedure. In p–O collisions, the nuclear modification factor and the acceptance-times-efficiency are assumed to be the same as in p–Pb collisions, while the signal-to-background ratio is evaluated as the average of the ratios obtained in pp [62] and p–Pb [63] collisions. In O–O collisions, $R_{\mathrm{AA}} = 0.8$ is assumed, considering that in the most peripheral Pb–Pb collisions the nuclear modification factor does not exhibit a clear p_{T} dependence and amounts to about 0.7 [64]. The J/ψ raw yields as a function of p_{T} are evaluated based on the hypothesis that the signal-to-background ratio in central O–O collisions is the same as in peripheral Pb–

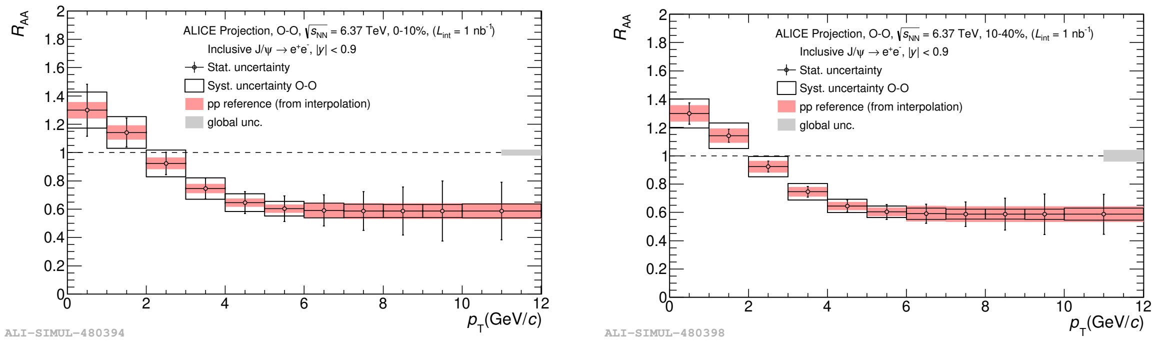

Fig. 12: Projections for inclusive J/ψ R_{AA} at midrapidity in central (left) and semi-central (right) O–O collisions at $\sqrt{s_{\mathrm{NN}}}$ = 6.37 TeV, for $L_{\mathrm{int}} = 1$ nb^{-1}.

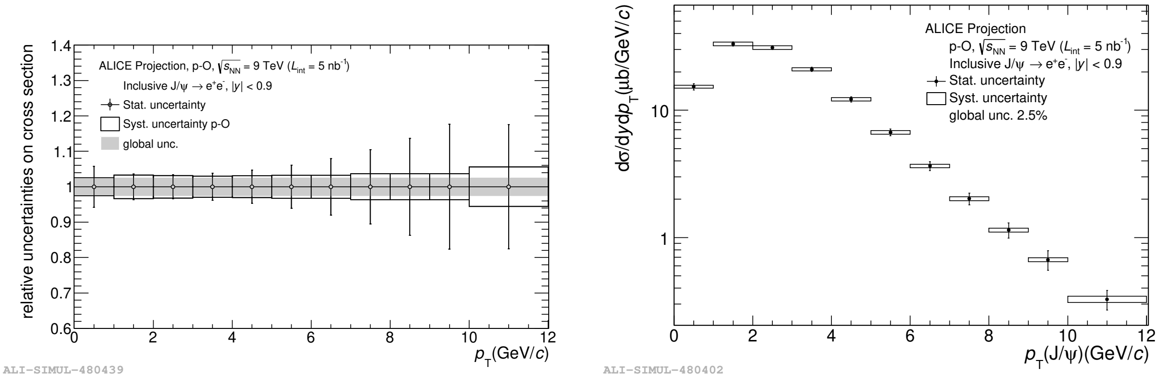

Fig. 13: Projections for inclusive J/ψ production cross section at midrapidity in minimum bias p–O collisions at $\sqrt{s_{\mathrm{NN}}} = 9$ TeV, for $L_{\mathrm{int}} = 5$ nb^{-1}. The left-hand panel shows the relative uncertainties on the measured cross section. The right-hand panel shows the expected cross section with uncertainties.

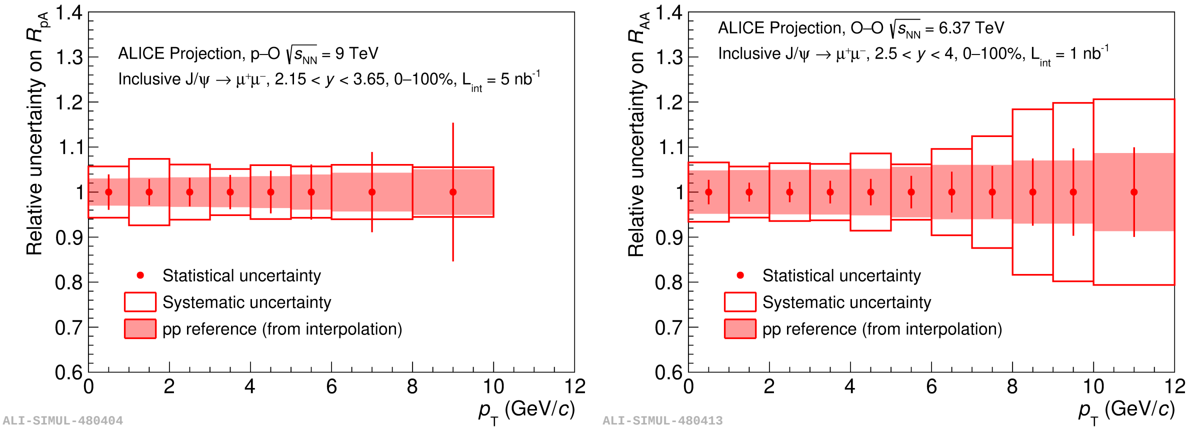

Fig. 14: Relative uncertainties on the J/ψ nuclear modification factor in p–O collisions ($2.15 < y < 3.65$, 0–100%) at $\sqrt{s_{\mathrm{NN}}} = 9$ TeV (left panel) and in O–O collisions ($2.5 < y < 4$, 0–100%) at $\sqrt{s_{\mathrm{NN}}} = 6.37$ TeV. The error bars and open boxes represent the statistical and systematic uncertainties, respectively. The uncertainties of the pp reference are represented by the shaded boxes.

Pb collisions (40-90%), while for semi-central ones it corresponds to the average of peripheral Pb–Pb and p–Pb collisions. Since the acceptance-times-efficiency can be sensitive to the p_{T} trigger threshold, two different possibilities are tested, adopting the p–Pb ($p_{\mathrm{T}} > 0.5$ GeV/c) and Pb–Pb ($p_{\mathrm{T}} > 1$ GeV/c) as well as the J/ψ yield is obtained as their average.

The main sources of systematic uncertainty on the nuclear modification factor in p–O and O–O collisions are not expected to vary significantly with respect to Run 2, with the exception of the one associated to the proton–proton reference, evaluated here with an interpolation procedure. In particular, the ALICE data collected in pp collisions at 7, 8 and 13 TeV [65] are fitted bin-by-bin in p_{T} using an exponential, a power law and a linear function and the values at 6.37 and 9 TeV are obtained as the average of the three results. The uncertainty from the interpolation procedure ranges between 3 and 5% and between 5 and 8% for p–O and O–O collisions respectively. In Fig. 14 the expected uncertainties on the nuclear modification factor in the two colliding systems are shown. It should be noted that in both cases the statistical error represent the dominant contribution to the overall uncertainty.

Figure 15 shows together the projected J/ψ production measurements at central and forward rapidity in minimum-bias O–O collisions: R_{AA} is reported in the left-hand panel (using measurements in central Pb–Pb collisions as central values for illustration) and the yield is reported in the right-hand panel

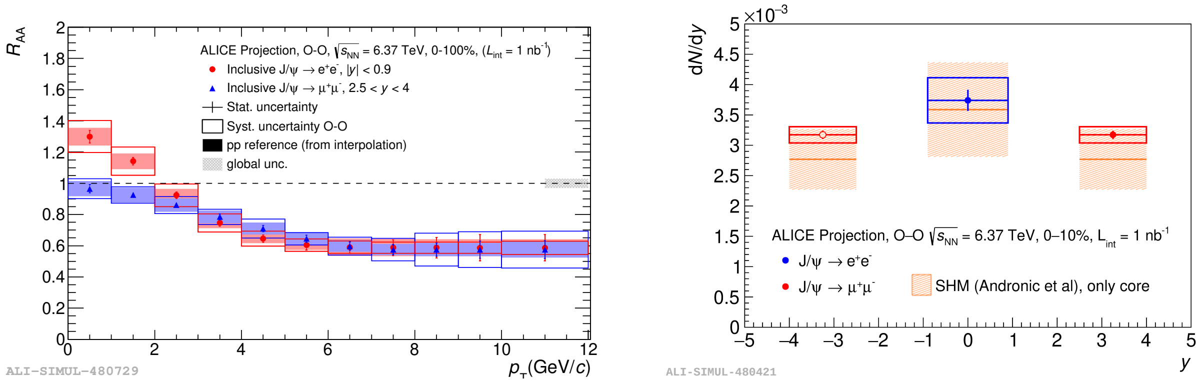

Fig. 15: Left: projections for inclusive J/ψ $R_{\rm AA}$ at mid and forward rapidity in minimum-bias O–O collisions at $\sqrt{s_{\rm NN}}$ = 6.37 TeV, for $L_{\rm int} = 1$ nb^{-1}. Right: projections for inclusive J/ψ yields reconstructed at mid and forward rapidity in 0–10% most central O–O collisions at $\sqrt{s_{\rm NN}}$ = 6.37 TeV, assuming $L_{\rm int} = 1$ nb^{-1}. The corresponding predictions from Standard Hadronization Model (SHM) [61], which include only the contributions from the "core", are superimposed.

and compared with the predictions of the Statistical Hadronization Model (SHM, core only, for illustration) [61].

7 Strangeness and light nuclei production

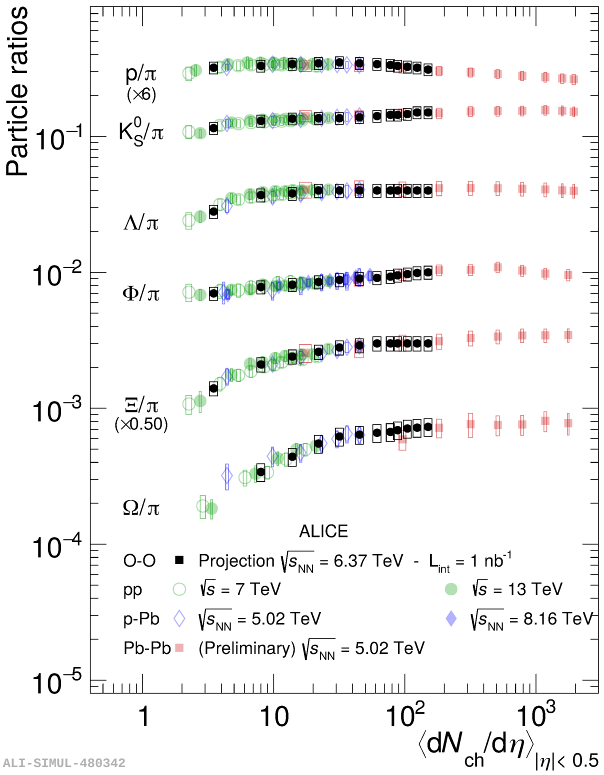

Fig. 16: Projected measurement of ratios to pions for protons, K^0_S, Λ, ϕ, Ξ, Ω, as a function of multiplicity at midrapidity in O–O collisions, for $L_{\rm int} = 1$ nb^{-1}, compiled with Run 1 and Run 2 measurements [3, 66–76].

Strangeness and light nuclei production studies in nucleus–nucleus collisions are of primary interest for the determination of the hadrochemistry of the formed medium and for the study of hadronization per se. We have shown that hadron relative yields (e.g. ratio to pions) evolve coherently across different colliding systems once the final state multiplicity emerging from the collision is used as a reference. The oxygen run will allow us to cover final state multiplicities spanning from few particles at midrapidity (lower than the average multiplicity registered in pp at the same energy) up to the values measured in semi-peripheral Pb–Pb interactions, thus offering the unique opportunity to study the evolution of hadrochemistry in the whole range of variability below the flattening in semicentral and central Pb–Pb collisions. Moreover, the expected integrated luminosity will enable the study of deuteron (d), Helium-3 (^{3}He) and hypertriton ($^3_\Lambda$H) production with good precision.

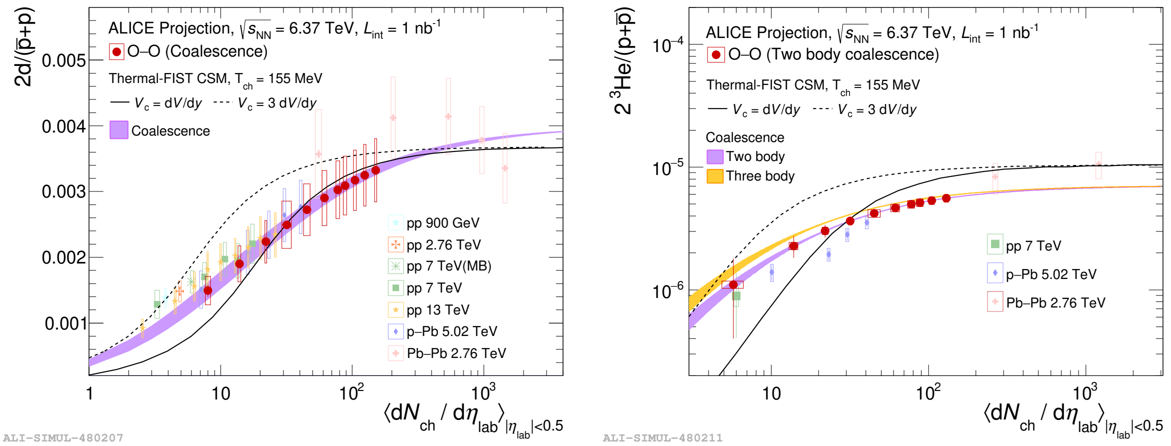

Fig. 17: Projected d/p ratio (left) and ^{3}He/p (right) as a function of $\langle dN_{ch}/d\eta \rangle_{|\eta|<0.5}$ for the $L_{int} = 1$ nb^{-1} O–O data sample at $\sqrt{s_{NN}} = 6.37$ TeV (red symbols). The scaled statistical uncertainties and the systematic uncertainties are shown as lines and boxes, respectively. The published results in pp, p–Pb and Pb–Pb collisions at different energies are included for comparisons. Predictions from thermal [77] and from coalescence model [78] are shown as lines and bands, respectively.

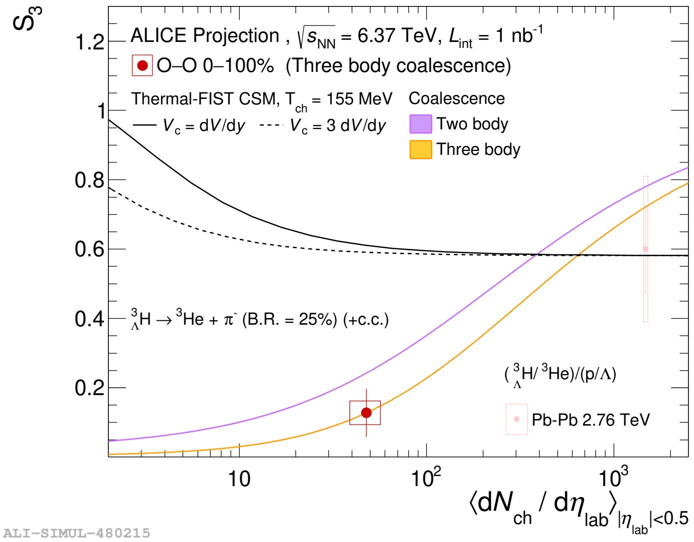

Fig. 18: Projected S_3 ratio as a function of $\langle dN_{ch}/d\eta \rangle_{|\eta|<0.5}$ for the $L_{int} = 1$ nb^{-1} O–O data sample at $\sqrt{s_{NN}} = 6.37$ TeV (red symbols). The scaled statistical uncertainties and the systematic uncertainties are shown as lines and boxes, respectively. The published results in Pb–Pb collisions at different energies are included for comparisons. Predictions from thermal [77] and from two and three body coalescence model [78] are shown as lines and bands, respectively.

7.1 Strangeness production

Light flavour particles (including hyperons) will be studied as a function of the charged-particle multiplicity at central rapidity. The expected statistical uncertainties for $L_{\mathrm{int}} = 1\ \mathrm{nb}^{-1}$ in each p_{T} and multiplicity range were estimated through interpolation from previous measurements in pp and p–Pb collisions at different energies [3, 66–72], exploiting the striking observation at the LHC that hadrochemistry is energy-independent if studied as a function of the multiplicity. Invariant mass distributions containing less than 100 counts were discarded. Integration of the p_{T} distributions and extrapolation to the unmeasured low-p_{T} part lead to the extraction of the integrated yields. As can be seen in Fig. 16, the statistical uncertainty is negligible, with the only exception of the lowest multiplicity class for the Ω baryon. The systematic uncertainties for this projection were assumed to be the same as in former analyses of Run 2 data.

7.2 Light (hyper)nuclei production

Projections for the production of (anti)deuteron, $(^{3}\overline{\mathrm{He}})^{3}\mathrm{He}$ and $(^{3}_{\Lambda}\overline{\mathrm{H}})^{3}_{\Lambda}\mathrm{H}$ as a function of the midrapidty multiplicity were also estimated. The projections are shown in terms of ratios to protons (plus antiprotons) in Fig. 17 for deuteron and $^{3}\mathrm{He}$ and in terms of S_3 in Fig. 18 for $^{3}_{\Lambda}\mathrm{H}$. The double-ratio of yields S_3 is defined as:

$$S_3 = \frac{^{3}_{\Lambda}\mathrm{H}}{^{3}\mathrm{He}} \times \frac{\mathrm{p}}{\Lambda}\,. \tag{6}$$

The projections were obtained as follows. The theoretical expectations for the yields in O–O collisions were taken from the coalescence model for d/p ratio, from three body coalescence for $^{3}\mathrm{He}$/p ratio and S_3 [78]. These models were chosen because they predict the lowest yields. The reconstruction efficiency was assumed to be the same as for the measurements on Run 2 data, because also in Run 3 the same detectors will be used for particle identification and tracking. The statistical uncertainties were computed for $L_{\mathrm{int}} = 1\ \mathrm{nb}^{-1}$. The systematic uncertainties were assumed to be the same as in the Run 2 measurements.

8 Flow observables

Measurements of the anisotropic particle flow is a powerful tool to study the properties of the QGP created in ultra-relativistic heavy-ion collisions. The observation of long-range two- and multi-particle correlations in pp and p–Pb collisions suggests the emergence of anisotropic flow also in these small collision systems. Measurements of long-range two-particle correlations involving identified particles show a characteristic mass-dependence of v_2 at low p_{T} [79], which in heavy-ion collisions is interpreted as a consequence of the interplay between elliptic flow and radial flow [80]. In high-multiplicity pp and p–Pb collisions, the measured 4-particle and 6-particle cumulants reach negative and positive values, respectively, which confirms the collective nature of the observed phenomena [4]. The collectivity is further studied using correlations of flow coefficients via symmetric cumulants [81]. The results show negative correlation between v_2^2 and v_3^2 and positive correlation between v_2^2 and v_4^2, showing similar magnitudes of correlation strengths in pp, p–Pb and Pb–Pb collisions [4]. The similarity of the observed long-range two- and multi-particle correlations in small and large collisions systems suggests that the same underlying mechanism drives the collective phenomena. Recent theoretical developments and experimental data indicate that the high-multiplicity pp and p–Pb collisions are dominated by final-state effects, including possible formation of QGP-droplets. Meanwhile for the low-multiplicity collisions, it is argued that initial-momentum correlations arising from gluon saturation might play an important role [82].

The study of O–O collisions can have a huge impact on the overall understanding of the collectivity in small collision systems. The O–O collisions reach multiplicities up to those of peripheral Pb–Pb and Xe-Xe collisions, which enables the initial-geometry scanning across different collision systems. The O–O collisions have also a significant overlap with pp and p–Pb collisions down to very low multiplicities and thus can shed more light on the nature of these fluctuation-dominated regions. For example, searches of the initial-momentum anisotropy can be performed with the proposed O–O run.

8.1 Two-particle correlations

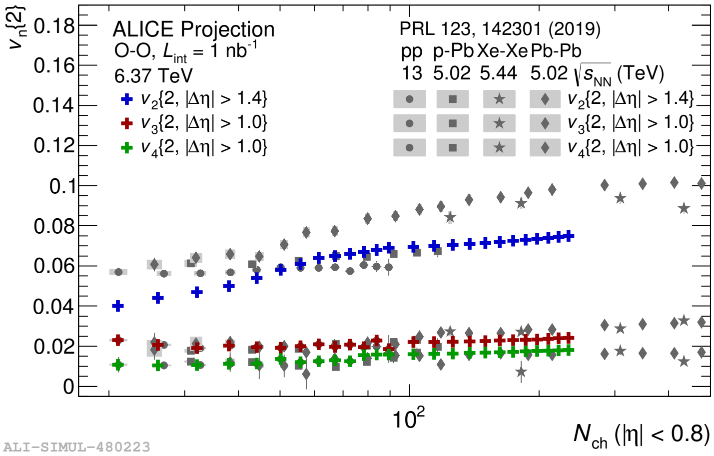

Fig. 19: Projected v_2, v_3 and v_4 coefficients as a function of $N_{\rm ch}$ for the $L_{\rm int} = 1$ nb^{-1} O–O data sample at $\sqrt{s_{\rm NN}}$ = 6.37 TeV. Only the expected statistical uncertainties are shown. The published results in pp, p–Pb, Xe–Xe and Pb–Pb collisions from Ref. [4] are presented for comparison.

Figure 19 shows the projection for v_2, v_3 and v_4 coefficients in O–O collisions at $\sqrt{s_{\rm NN}}$ = 6.37 TeV, corresponding to 1 nb^{-1} integrated luminosity. The pseudorapidity separations are the same as those used in the published measurements in pp, p–Pb, Xe–Xe and Pb–Pb collisions [4]. The central values of these projected results are taken from IP-Glasma+MUSIC+UrQMD model predictions for O–O collisions [82]. The statistical uncertainties for $N_{\rm ch} < 100$ are obtained from pp data scaled according to the number of events in each multiplicity bin estimated from the PYTHIA Angantyr model [15]. For the higher $N_{\rm ch}$, the statistical uncertainties are calculated by using the relative statistical uncertainty from the low-multiplicity region and scaling it by the number of events in each high-multiplicity bin. As it can be seen, the expected precision of the v_n measurement in O–O collisions is excellent and will allow to bridge the results from the fluctuation-dominant region to the geometry-dominant region.

8.2 Multi-particle cumulants

Measurement of multi-particle cumulants is useful to gain further insight into flow phenomena in small collision systems, given the strong suppression of non-flow contamination from resonance decays and jets. The possible observation of alternating signs of 4-, 6-, 8-, 10- and 12-particle cumulants of v_2 and hence real-valued v_2 of higher-order cumulants would further confirm the existence of collective effects [83]. Moreover, the higher-order cumulants of v_2 provides unique information on the probability density distribution (p.d.f.) of the v_2 coefficient and thus put tight constraints on the event-by-event fluctuations of the initial-state ellipticity in small systems. Figure 20 shows the projected uncertainties of the multi-particle cumulants $v_2\{m\}$ ($m = 4, 6, 8, 10, 12$) for a sample of $L_{\rm int} = 1$ nb^{-1} O–O collisions at $\sqrt{s_{\rm NN}}$ = 6.37 TeV. The current results from pp, p–Pb, Xe–Xe and Pb–Pb collisions are also shown for comparison [4]. The central values of $v_2\{m\}$ for O–O projected results are based on the mean values of measurements of $v_2\{m\}$ in Pb–Pb collisions at $\sqrt{s_{\rm NN}}$ = 5.02 TeV for centrality ranges of 60–65%, 65–70%, 70–75% and 75–80%. The statistical uncertainty is calculated based on the Pb–Pb data scaled according to the number of events in each multiplicity bin of O–O collisions estimated from PYTHIA Angantyr simulations [15]. The figure shows that the measurements in O–O collisions would cover the

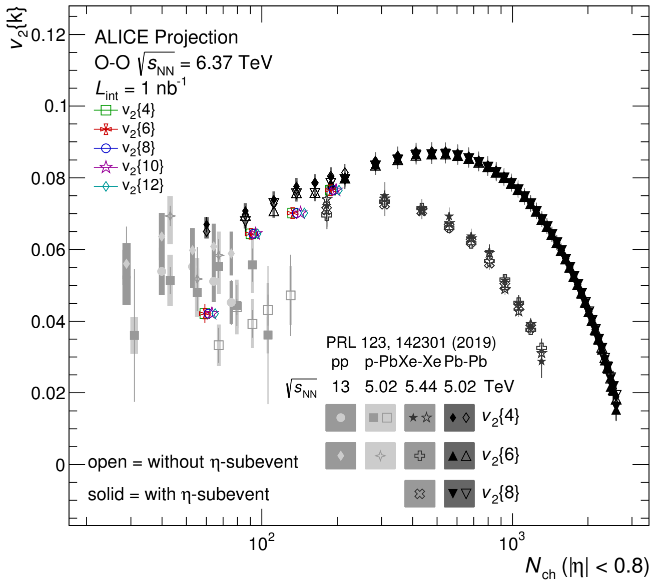

ALI-SIMUL-480242

Fig. 20: Projected multi-particle cumulants of v_2 as a function of N_{ch} for the $L_{int} = 1$ nb^{-1} O–O data sample at $\sqrt{s_{NN}} = 6.37$ TeV. Only the scaled statistical uncertainties are shown.The published results in pp, p–Pb, Xe–Xe and Pb–Pb collisions from [4] are presented for comparisons.

multiplicity range between pp, p–Pb and heavy-ion collisions, with precision which will be sufficient for quantitative comparisons.

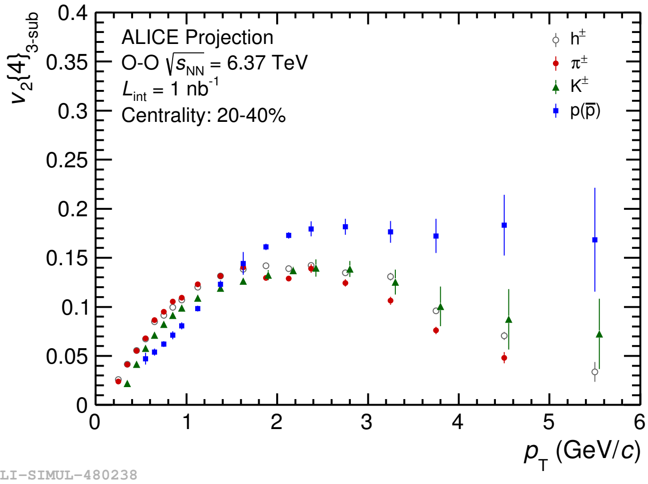

ALI-SIMUL-480238

Fig. 21: Projected $v_2\{4\}$ with three-subevent method in centrality 20–40% for the $L_{int} = 1$ nb^{-1} O–O data sample at $\sqrt{s_{NN}} = 6.37$ TeV. Only the expected statistical uncertainties are shown.

8.3 Identified particles v_2

The proposed O–O run with integrated luminosity of 1 nb^{-1} will allow measurements of the p_T-differential v_2 of identified hadrons. The goal of these measurements will be to investigate possible mass ordering at low p_T and baryon vs meson grouping at intermediate p_T. In order to suppress the non-flow contamination in the v_2 measurements, four-particle cumulants with 3-subevent method is proposed. The corresponding projections are shown in Fig.21. The central values of the $v_2\{4\}_{3-\text{sub}}$ coefficients are taken from the results in Pb–Pb collisions at $\sqrt{s_{NN}} = 5.02$ TeV in the multiplicity range

$63 < N_{\mathrm{ch}}(|\eta| < 0.8) < 112$. The statistical uncertainties are scaled according to the expected number of events in O–O collisions for a 1 nb^{-1} and multiplicities estimated using the PYTHIA Angantyr model [15]. As it can be seen, these measurements will provide an excellent opportunity to examine both the hydrodynamic nature of the collectivity and the particle production via quark coalescence in the small O–O collision system [84].

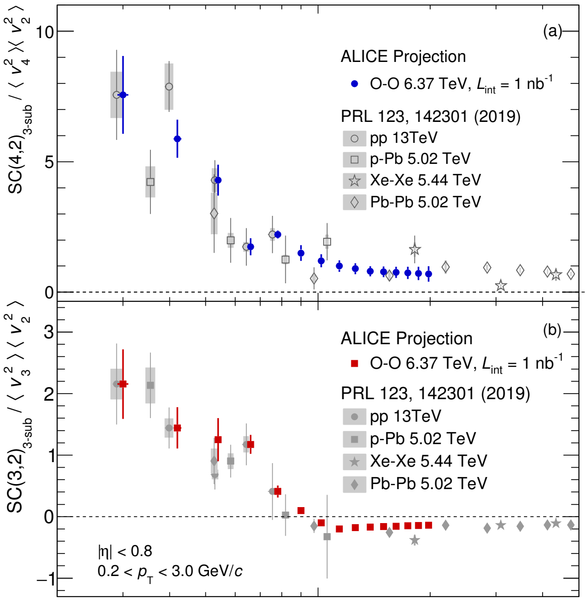

ALI-SIMUL-480219

Fig. 22: Projected normalized symmetric cumulant $NSC(m,n)$ as a function of N_{ch} for the $L_{\mathrm{int}} = 1$ nb^{-1} O–O data sample at $\sqrt{s_{\mathrm{NN}}} = 6.37$ TeV. Only the statistical uncertainties are shown.The published results in pp, p–Pb, Xe–Xe and Pb–Pb collisions from Ref. [4] are presented for comparison.

8.4 Symmetric cumulants

Further information on the origin of the collective effects can be obtained from the study of normalized symmetric cumulants $NSC(m,n)$, which quantify the correlation between v_n^2 and v_m^2. Figure 22 presents the projected results of multiplicity dependence of $NSC(4,2)$ and $NSC(3,2)$ with the three-subevent method [85]. For $N_{\mathrm{ch}} < 80$, the central values are taken from the published measurements in pp collisions at $\sqrt{s}$ = 13 TeV, while the values at higher multiplicities are based on IP-Glasma+MUSIC+UrQMD predictions for O–O collisions [82]. The statistical uncertainties are based on the ones obtained in pp collisions scaled according to the expected number of O–O collisions estimated from PYTHIA Angantyr model [15]. The expected precision of the measurement of the symmetric cumulants in O–O collisions will allow quantitative comparisons with the results in pp, p–Pb, Xe–Xe and Pb–Pb collisions at the same multiplicity. In addition, the measurement will confirm or infirm the sign inversion of $NSC(3,2)$ at N_{ch} of about 100, which can be interpreted as a signature of the transition from fluctuation-dominated regime to geometry-dominated regime.

8.5 Correlation between $\langle p_{\mathrm{T}} \rangle$ and v_2 coefficient

The Pearson Correlation Coefficient, $\rho(v_2^2, \langle p_{\mathrm{T}} \rangle)$, which measures the correlation between v_2^2 and $\langle p_{\mathrm{T}} \rangle$ [86], can be useful to investigate different roles of initial-state momentum anisotropies and final-state effects in the observed flow in small collision systems. The IP-Glasma+Music+UrQMD model that includes contributions from both initial-momentum correlations from gluon saturation and final-state hydrodynamic response to the initial geometry predicts a characteristic sign inversion of $\rho(v_n^2, \langle p_{\mathrm{T}} \rangle)$ as a function

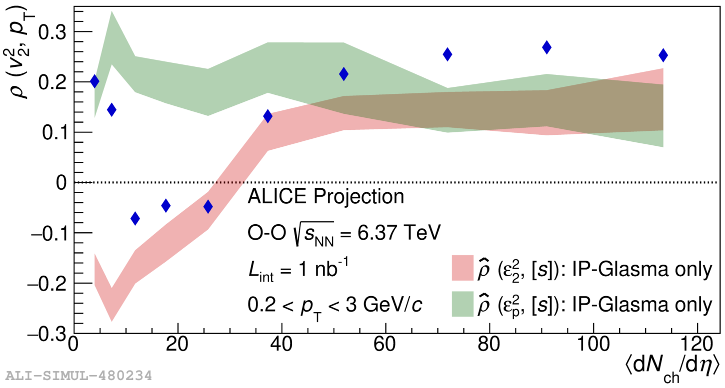

Fig. 23: Projected Pearson Correlation Coefficient of mean transverse momentum and v_2 coefficient, $\rho(v_n^2, \langle p_T \rangle)$, as a function of N_{ch} for the $L_{int} = 1$ nb^{-1} O–O data sample at $\sqrt{s_{NN}} = 6.37$ TeV. Only the statistical uncertainties are shown. The estimations of the initial geometry (red shadowed band) and the initial momentum anisotropy (green shadowed band) using IP-Glasma model are presented for comparison. Both of the estimations are based on the calculation using the average event entropy density [s].

of multiplicity. As shown in Fig.23, the contribution of the initial-momentum anisotropy from gluon saturation [87], represented by the green shadowed band, is positive for the entire multiplicity range. In contrast, the contribution of the initial-spatial anisotropy, represented by the red shadowed band, is positive at high multiplicities but reaches negative values at low multiplicities. The combination of these two contributions leads to a double sign inversion of $\rho(v_n^2, \langle p_T \rangle)$, which is predicted for all nucleus–nucleus systems, e.g. Pb–Pb, Xe–Xe and O–O collisions. The observation of the double sign inversion in Pb–Pb and Xe–Xe collisions is challenging as it is expected to occur in very peripheral collisions. Instead, measurements in the semi-peripheral O–O collisions can have better sensitivity. This is illustrated in the $\rho(v_n^2, \langle p_T \rangle)$ projections using three-subevent method for the $L_{int} = 1$ nb^{-1} O–O data sample at $\sqrt{s_{NN}} = 6.37$ TeV shown in Fig. 23. The central values are the IP-Glasma+Music+UrQMD predictions for O–O collisions [82]. The statistical uncertainties are based on the Pb–Pb results scaled according to the number of O–O collisions estimated from the PYTHIA Angantyr model [15] for $L_{int} = 1$ nb^{-1} data sample. Given the presented projections, the O–O data can have a significant impact in the search for signatures of initial-momentum anisotropy from gluon saturation. Nevertheless, it is worth noting that the measurement of $\rho(v_n^2, \langle p_T \rangle)$ at low multiplicity could be potentially biased by non-negligible non-flow effects from back-to-back (mini)jets [88, 89].

9 Hadron–hadron interaction with femtoscopy techniques

The measured correlation function for hadron-hadron pairs represents a powerful tool to investigate the underlying interaction among particles [90–94]. It has already been shown in recent theoretical work [95–97] that the shape and the strength of the interaction signal in the correlation function is modified by the emitting source size, which is in turn related to the colliding system. Several features of the strong interaction, such as bound states, spin dependence, coupled-channel and annihilation dynamics, can be investigated by studying the correlation function in different colliding systems. An O–O run with an integrated luminosity of 0.5–1 nb^{-1} will allow us to address these topics. Based on data obtained in ALICE pp, p–Pb and Pb–Pb collisions, on the scaling of the source size with the charged multiplicity [98–100], the average radii obtained in O–O collisions will be of the order of 2.5 fm for minimum-bias collisions and ranging from 3 to 1.5 fm for central (0–20%) and peripheral (60–100%) events. A detailed study, using EPOS simulations [101], on the obtained source size in O–O collisions has been performed and validates the above-mentioned values. The values of the source sizes used for the following projections are reported in Table 1.

Table 1: Estimated source radii for O–O collisions.

Centrality	$(\mathrm{d}N_{\mathrm{ch}}/\mathrm{d}\eta)^{1/3}$	r_0 (fm)
0–100%	3.7	2.5
0–20%	4.7	3
20–40%	4.1	2.8
40–60%	3.4	2.5
60–100%	2.3-2.8	1.5

The yields of the considered pairs were estimated in comparison to results obtained in pp high-multiplicity collisions at $\sqrt{s}$ = 13 TeV. For $L_{\mathrm{int}} = 1$ nb^{-1}, the number of events in comparison with pp high-multiplicity collisions at $\sqrt{s}$ = 13 TeV is equal to a factor $\alpha_{\mathrm{evt}} = 1.3$, and the same value is expected in terms of multiplicity. To translate the latter into number of pairs, a study on the number of pairs per event as a function of $N_{\mathrm{ch}}(|\eta| < 0.8)$ was performed, leading to an increase of 1.47 with respect to the pp sample: $N^{\mathrm{O-O}}_{\mathrm{pairs}} = 1.47 \times N^{\mathrm{pp}}_{\mathrm{pairs}}$. The expected final number of pairs hence reads $N^{\mathrm{O-O}}_{\mathrm{pairs}} = 1.3 \times 1.47 \times N^{\mathrm{pp}}_{\mathrm{pairs}} = 1.9 \times N^{\mathrm{pp}}_{\mathrm{pairs}}$, with a reduction factor of $1/1.38$ ($\approx 30\%$) in the statistical uncertainties.

In the following, projections are reported for the O–O run for different pairs, focusing on three main categories:

1. coupled-channels and annihilation dynamics:
   - p–Λ (Fig. 24);
   - baryon-antibaryon (B–$\overline{\mathrm{B}}$) pairs, here p–$\overline{\mathrm{p}}$ (Fig. 25), p–$\overline{\Lambda}$ and Λ–$\overline{\Lambda}$ (Fig. 26);
   - K$^-$p (Fig. 27);
2. presence of bound states: p–Ω^- (Fig. 28);
3. spin dependence of the interaction: Λ–d (Fig. 29).

Starting from the theoretical predictions that better described the available two-particle correlation data for the specific pair, the projections were obtained by sampling along this curve with a Gaussian distribution. The width of the latter is given by the statistical uncertainties obtained in pp high-multiplicity collisions at $\sqrt{s}$ = 13 TeV multiplied by the expected improvements in the O–O run ($\times 1/1.38$). Details on the theoretical models can be found in the caption of each figure below.

The study of B–$\overline{\mathrm{B}}$ interactions in O–O collisions will allow to investigate the annihilation dynamics, largely present in these systems, and the possible existence of bound states [102, 103]. Predictions on such bound states are present in literature, arising from the attractive elastic term, but no clear experimental evidence has been found so far [104–107]. The inelastic term due to the annihilation processes can eventually wash out the bound spectrum hence the understanding of the strength and range of annihilation in these systems is fundamental. The correlation functions obtained for p–$\overline{\mathrm{p}}$, p–$\overline{\Lambda}$ and Λ–$\overline{\Lambda}$ pairs at the intermediate source sizes expected in O–O collisions will be less affected by the annihilation channels and will provide additional constraints on the current knowledge of B–$\overline{\mathrm{B}}$ interaction. Having at hand the same pairs measured in different colliding systems (pp, Pb–Pb and O–O), probing a wide range of source sizes, can improve the current understanding of B–$\overline{\mathrm{B}}$ interaction, also for systems as p–$\overline{\Lambda}$ and Λ–$\overline{\Lambda}$ where data are currently scarce or not present.

The study of K$^-$–p⊕K$^+$–$\overline{\mathrm{p}}$ in O–O collisions will allow to investigate the dynamic of coupled channels from small to large source radii in the same collisions system, allowing for a more precise determination of the interaction among these particles.

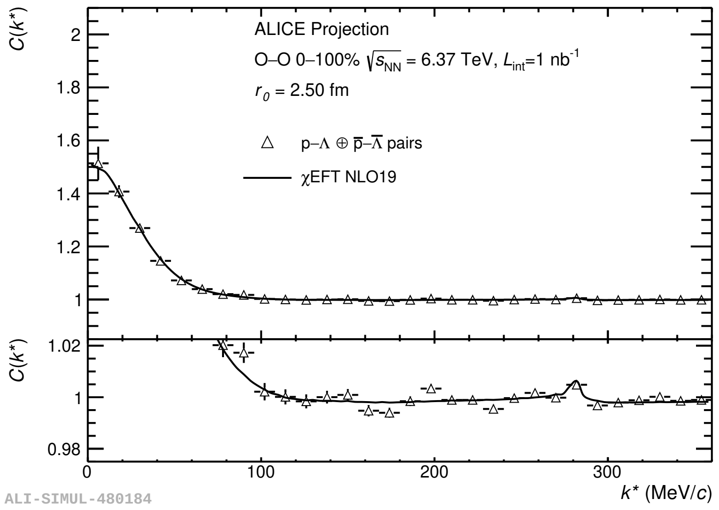

Fig. 24: Projected correlations for the $L_{\rm int} = 1$ nb^{-1} O–O data sample at $\sqrt{s_{\rm NN}}$ = 6.37 TeV for p–Λ pairs. The projections are obtained assuming a correlation signal driven only by the final state interaction, which is evaluated using a next-to-leading order χEFT potential [108]. The uncertainties are only statistical. In complete contrast to pp collisions, in O–O reactions the kinematic cusp at the threshold of the NΣ has a very small amplitude. An experimental verification will help to gain further insight into the properties of the NΣ ↔NΛ coupled system.

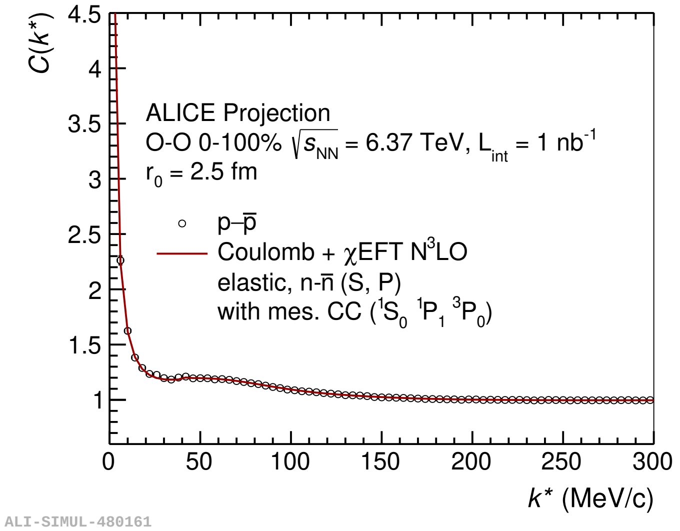

Fig. 25: Projected correlations for the $L_{\rm int} = 1$ nb^{-1} O–O data sample at $\sqrt{s_{\rm NN}}$ = 6.37 TeV for p–p̄ pairs. Only the scaled statistical uncertainties are shown. The projections have been obtained assuming a χEFT potentials with the elastic interaction and the coupled-channel n–n̄ included [109]. The annihilation mesonic channels has been taken into account using the Migdal-Watson approximation [110].

The study of the p–Ω^- interaction in O–O collisions would allow us to investigate on the existence of a bound state, as predicted by Lattice QCD calculations [113] and meson exchange models [114]. While no signal of the presence of such a bound state has been found in the studies performed using pp data in Run 2 [92], the larger source size expected in O–O collisions should accentuate the depletion in the correlation function caused by the presence of the bound state [115], which could be unequivocally detected by ALICE data, as shown in Fig. 28.

The study of Λ–d correlations is especially relevant for the investigation of the spin dependence, as two

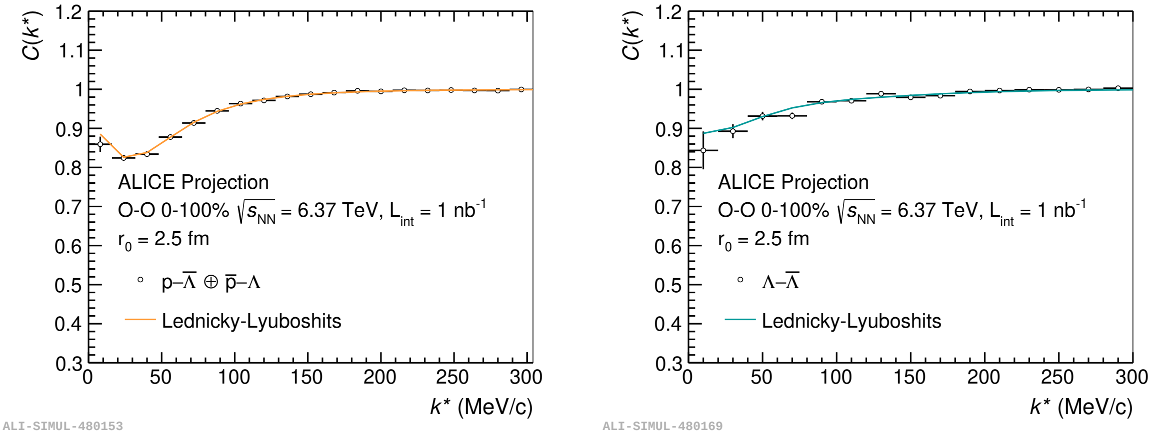

Fig. 26: Projected correlations for the $L_{\mathrm{int}} = 1$ nb^{-1} O–O data sample at $\sqrt{s_{\mathrm{NN}}} = 6.37$ TeV for p–$\overline{\Lambda}$ (left) and Λ–$\overline{\Lambda}$ (right) pairs. Only the scaled statistical uncertainties are shown. The projections have been obtained using the Lednický–Lyuboshits analytical formula. For Λ–$\overline{\Lambda}$ interaction the scattering parameters obtained in Pb–Pb femtoscopic measurements have been assumed [111]. For the p–$\overline{\Lambda}$ modeling, the Imf_0 obtained in Pb–Pb has to be increased by a factor 5.3 to take into account the large coupling to annihilation channels.

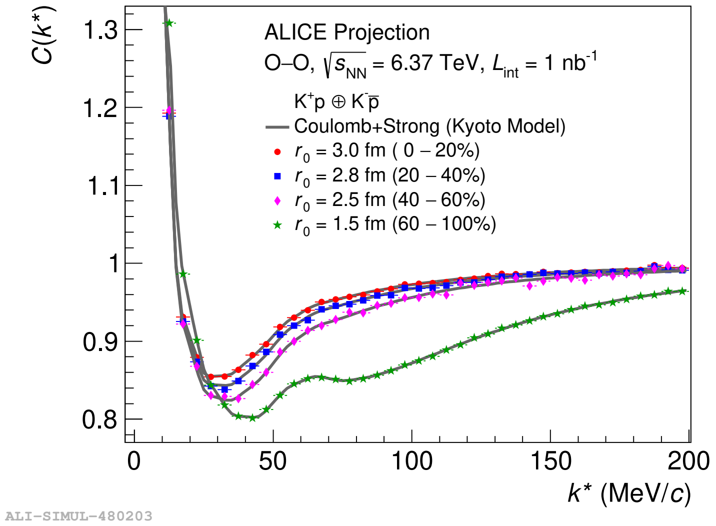

Fig. 27: Projected correlations for the $L_{\mathrm{int}} = 1$ nb^{-1} O–O data sample at $\sqrt{s_{\mathrm{NN}}} =$ 6.37 TeV for K$^-$–p$\oplus$K$^+$–$\overline{\mathrm{p}}$ pairs for difference centrality intervals. The corresponding source radii are obtained from EPOS simulations and shown in Tab. 9. The projections have been obtained using the theoretical correlation function [97] which are able to describe the data measured in pp collisions [112]. In the figure, the data are shown after the unfolding for detector resolution and particle identification. Only the scaled statistical uncertainties are shown.

spin states contribute, the spin-doublet state $(^2S_{1/2})$ and the spin-quartet state $(^4S_{3/2})$, the latter also depending on the spin-triplet ΛN interaction. Figure 29 shows the projection of Λ–d correlations in O–O collisions together with several predictions from [116] using the Lednický–Lyuboshits approach. The predicted data points are centred on the prediction using only the spin-doublet state. The uncertainties are statistical only and obtained from an ongoing analysis in high-multiplicity pp collisions at $\sqrt{s} = 13$ TeV by multiplication with 1/1.38 as described above.

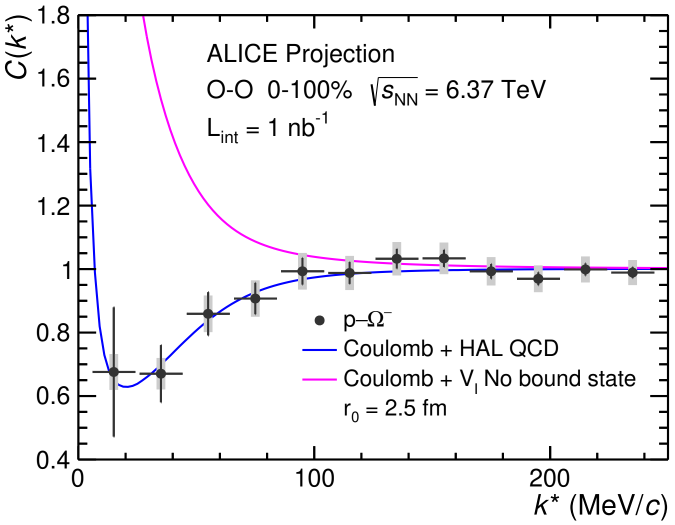

ALI-SIMUL-481172

Fig. 28: Projected correlations for the $L_{\text{int}} = 1$ nb^{-1} O–O data sample at $\sqrt{s_{\text{NN}}}$ = 6.37 TeV for p–Ω^- pairs. The projected data follows the blue line, that represents the expected correlation function considering the Coulomb interaction plus a strong attractive interaction as predicted by the HAL QCD collaboration [113]. The noticeable depletion of the correlation function is produced by the presence of a p–Ω^- bound state with a few MeV of binding energy, as predicted by HAL QCD. The magenta line represent, in contrast, the prediction using a strong attractive potential without the presence of the bound state [95].

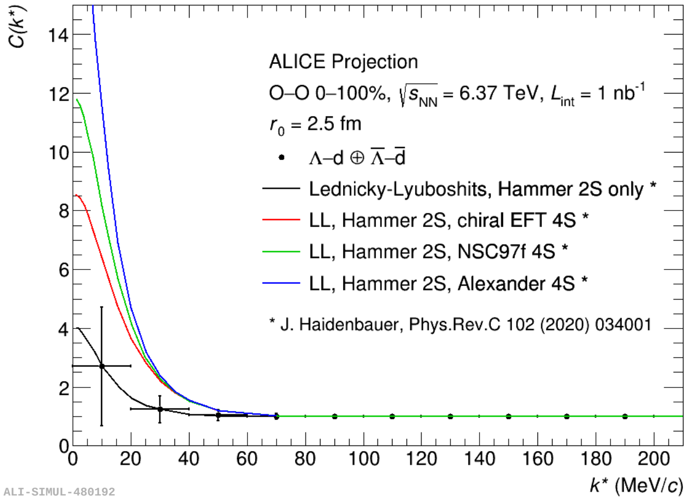

ALI-SIMUL-480192

Fig. 29: Projected correlations for the $L_{\text{int}} = 1$ nb^{-1} O–O data sample at $\sqrt{s_{\text{NN}}}$ = 6.37 TeV for Λ–d pairs. Only the scaled statistical uncertainties are shown. The projected data points are centred at the spin-doublet prediction obtained using an Lednický–Lyuboshits calculation [116]. The other theoretical curves including the spin-quartet state are as well taken from [116].

10 Photoproduction and diffraction

From the standpoint of ultra-peripheral collisions (photoproduction) and diffractive interactions, oxygen is a very interesting 'intermediate' nucleus, placed between protons and lead. An O–O run with an integrated luminosity of 0.5–1 nb^{-1} will allow ALICE to study a few key physics topics. Here, we focus on three topics: oxygen photodissociation, coherent and incoherent ρ photoproduction, and double-diffractive production of a few well-defined resonances: the $f_2(1270)$ and the $f_0(980)$. Two-photon production of dileptons could also be studied.

10.1 Photodissociation

The total cross section of electromagnetic dissociation (EMD) of oxygen in ^{16}O–^{16}O collisions at the LHC is estimated by the RELDIS model [117] as 126.6 mb and 133.5 mb at $\sqrt{s_{\mathrm{NN}}} = 5$ TeV and 7 TeV, respectively. It is about 11% of the hadronic cross section. According to RELDIS one can expect a variety of EMD channels represented by secondary neutrons, protons, as well as He, Li, Be, B, C and N nuclei. The fragments with $Z = A/2$ are a significant consideration for LHC operation, since they may, to same extent, remain in the beam, and subsequently collide with oxygen. Detailed estimates from beam simulations are in preparation by the LHC accelerator team.

10.2 Photoproduction of vector mesons

Coherent and incoherent photoproduction of vector mesons are interesting probes of nuclear targets. The cross sections are sensitive to nuclear PDF shadowing [118–120]. In the Good-Walker paradigm, measurements of $\mathrm{d}\sigma/\mathrm{d}t$ for coherent photoproduction probes the average target configuration, while incoherent photoproduction probes event-by-event fluctuations, including in nucleon positions, and, of greater interest, gluonic hotspots [121,122]. Incoherent photoproduction of vector mesons is of particular interest, since it has not yet been studied at high energies.

The STARlight Monte Carlo event generator [123] predicts a cross section for coherent J/ψ photoproduction in O–O collisions at $\sqrt{s_{NN}} = 6.37$ TeV of 26 μb. This is based on HERA data on $\gamma p \rightarrow \mathrm{J}/\psi p$ and a Glauber calculation [124]. It does not include gluon shadowing, so for lead targets, it overestimates the J/ψ cross section by about 30% [125]. For oxygen, the shadowing is expected to be much smaller. The incoherent J/ψ cross section is found to be 29 μb, a bit larger than the coherent cross section. The expected acceptance (including the 5.97% branching ratio to $\mathrm{e}^+\mathrm{e}^-$) is about 0.50% for $\mathrm{J}/\psi \rightarrow \mathrm{ee}$ in the central detector. A similar acceptance is expected for $\mathrm{J}/\psi \rightarrow \mu\mu$. The acceptance plus branching ratio for $J/\psi \rightarrow \mu\mu$ in the forward muon spectrometer is 0.21%. A run with integrated luminosity of 1 nb^{-1} would yield about 300 J/ψ candidates each for coherent and incoherent production, which are not sufficient for a significant estimate of shadowing effects.

The photoproduction cross sections for ρ mesons are expected to be almost three orders of magnitude larger than for J/ψ. STARlight predicts cross sections of 9.2 mb and 6.8 mb for coherent and incoherent photoproduction, respectively. STARlight has been shown to provide accurate coherent ρ^0 photoproduction predictions on lead and xenon targets at the LHC [126], and on lead targets at RHIC energies [127]. Figure 30 (left) shows how the oxygen measurement fits in with the existing measurements on proton, xenon and lead targets. The incoherent cross sections have been much less studied.

The large cross sections and the nearly-100% branching ratio to $\pi^+\pi^-$ lead to large signals. Including direct $\pi^+\pi^-$ production will boost these cross sections by about 7% and will alter the shape of $M_{\pi\pi}$. The expected acceptance in the ALICE central detector is about 7.0%, so a 1 nb^{-1} integrated luminosity would produce a signal of about 650,000 coherent events and 470,000 incoherent events within the ALICE central detector. Figure 30 (right) shows the predicted p_{T} spectra for coherent and incoherent photoproduction, within the ALICE central detector acceptance. The coherent component has a larger $\langle p_{\mathrm{T}} \rangle$ than in the lead data, since the photoproduction p_{T} scales roughly as $\hbar/R_A$. This signal is large enough so that it should be possible to measure the destructive interference between emission from the two nuclei [128, 129]. It should also be possible to make a precision measurement of the ratio of direct $\pi^+\pi^-$ to ρ production. Because of the larger p_{T} scale for oxygen targets compared to lead, this measurement should extend to higher p_{T} than the lead measurement.

This signal presents a unique opportunity to study incoherent photoproduction on a nuclear target. Inco-

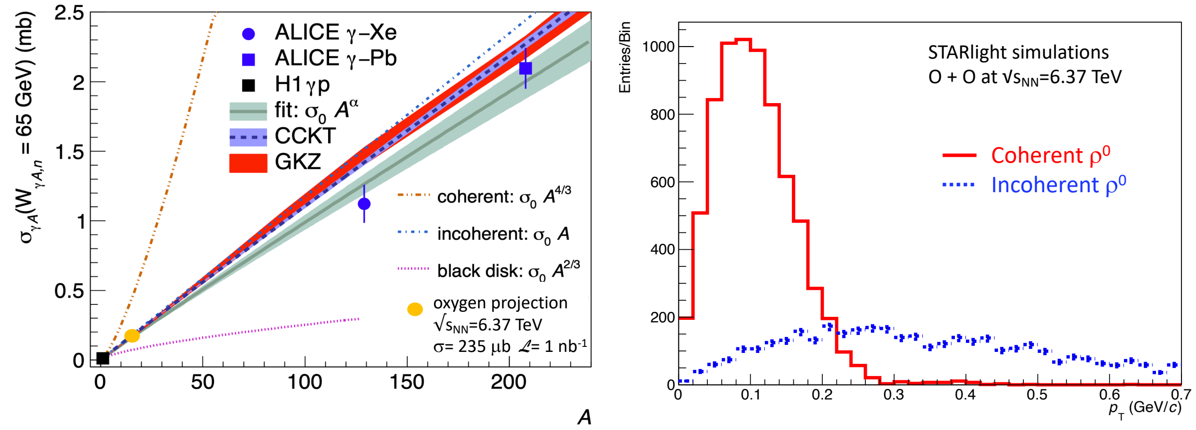

Fig. 30: Left: Cross sections for $\gamma A \rightarrow \rho A$, showing the predicted oxygen cross section along with existing ALICE measurements on xenon and lead targets. The absolute normalization is arbitrary. Adapted from Ref. [126]. Right: p_T spectra for coherent and incoherent photoproduction, for events within the ALICE central detector acceptance, obtained with the STARlight event generator.

herent photoproduction studies are challenging in lead, for a couple of reasons. The usual way to separate coherent and incoherent photoproduction is by observing neutron or proton emission from the excited target. However, lead is heavy enough so that that two ions involved in ρ photoproduction are relatively likely to exchange one or more additional photons which will break up one or both nuclei, even for a coherent photoproduction. Also, for lead, coherent production dominates over incoherent. Oxygen has a much lower Z, so additional photon exchange is rare. And, within the ALICE central acceptance, the ratio of coherent to incoherent ρ photoproduction is similar, so isolating the incoherent component should be easier. As Fig. 30 (right) shows, even at its maximum, the coherent is only about 10 times the incoherent contribution. Therefore, signals from the ALICE neutron and proton Zero Degree Calorimeters (ZDC) are expected to provide adequate rejection of coherent photoproduction to allow a measurement of $\mathrm{d}\sigma/\mathrm{d}t$ for incoherent production over the full t range. In short, ALICE should be well-placed to make the first high-energy measurement of incoherent ρ photoproduction, and thereby probe event-by-event fluctuations in the nuclear configuration.

10.3 Double-Pomeron fusion

In double Pomeron fusion, two Pomerons fuse to produce a meson, usually spin 0 or spin 2. Double-Pomeron fusion has been extensively studied with proton beams at fixed-target experiments, most notably at the SPS. However, much less is known about the process in ion-ion collisions. Cross section calculations are complicated by the fact that the Pomeron is believed to be short-ranged. Observable diffractive reactions require double-Pomeron exchange and nothing else to occur. The ‘nothing else’ criteria can be accounted for including a survival factor to account for possible additional interactions. In one calculation, the survival factor reduces the A-dependence of the cross section from $A^{8/3}$ before corrections to A^0 after corrections [130]. The same calculation finds that, for p–A collisions, the cross section should go as $A^{2/3}$, i.e. as the frontal surface area of the larger nucleus. Another approach is to assume that, since the Pomeron is short-ranged, and since ‘nothing else’ requires that the two nuclei do not interact, the cross section for ions with atomic numbers A_1 and A_2 might scale with their circumferences, as $A_1^{1/3} A_2^{1/3}$.

There is little relevant data to shed light on this A-dependence. The HELIOS collaboration studied p–A collisions with a variety of targets at the CERN SPS and observed that the single-diffractive cross section scaled as $A^{0.35\pm0.02}$ [131], i.e. as the nuclear circumference. The only high-energy data involving ions comes from a run at the CERN Intersecting Storage Ring facility, where α–α collisions were studied. The group found that the cross section for double-Pomeron interactions comprised the same fraction of the total cross section in pp and α–α collisions [132].

Additional ion-ion studies can shed light on the A-dependence of Pomeron interactions, and, from that, on the range of the Pomeron. They also probe Pomeron interactions involving neutrons. O–O collisions are well suited for these studies. Oxygen provides a good lever-arm in A, but has a small-enough Z to avoid an overwhelming background of photoproduction and two-photon interactions. The cross sections to produce the $f_2(1270)$ and $f_0(980)$ are high enough so that both could be detected with good precision with an integrated luminosity of 1 nb^{-1}.

An additional, albeit speculative, topic that could be studied: interference between double-Pomeron channels, photonuclear channels and possibly even two-photon processes. All of these channels produce resonances which decay to $\pi^+\pi^-$ final states. If the final states are indistinguishable, then the amplitudes add, leading to the possibility of interference. If the amplitudes are similar, then this interference could be visible in $\mathrm{d}\sigma/\mathrm{d}M_{\pi\pi}$ and/or the angular distributions. In pp collisions, events with two rapidity gaps come dominantly from double-diffraction, while in Pb–Pb they come mostly from photoproduction; in O–O the two processes should have comparable rates, a well-suited situation to address their interference.

11 Summary

This document reports the ALICE performance studies for a selection of measurements that could be carried out with a short O–O run during the LHC Run 3. The baseline centre-of-mass energy per nucleon–nucleon collision is taken as $\sqrt{s_{\mathrm{NN}}} = 6.37$ TeV and the projections are made for an integrated luminosity $L_{\mathrm{int}} = 1\ \mathrm{nb}^{-1}$.

- Jet quenching effects will be searched for using the charged-particle nuclear modification factor and semi-inclusive hadron–jet recoil. For the former, a systematic uncertainty of 4–5% is projected, for p_{T} up to about 40 GeV/c, for both the 0–100% and 0–30% centrality classes. This includes an uncertainty of about 3% on normalisation (which requires a van der Meer scan for O–O) and an uncertainty of about 3% for the scaling of the pp reference measured at 5.02 TeV. The semi-inclusive hadron–jet recoil measurement is projected to be sensitive to a jet energy shift as small as about 160 MeV, which are dominated by the uncertainty introduced by pp reference scaling in energy.
- The D-meson nuclear modification factor is sensitive to charm quark energy loss and in-medium diffusion. It is projected to have a systematic uncertainty of about 8–12%, with much smaller statistical uncertainty from p_{T} =0 to 30 GeV/c, and pp reference scaling uncertainty of 5% below 2 GeV/c and 2% at higher p_{T}. The elliptic flow coefficient of D mesons is projected to have an absolute statistical uncertainty of about 0.02 between 1 and 10 GeV/c.
- The measurement of the J/ψ nuclear modification factor is sensitive to dissociation and possible regeneration effects if a deconfined medium is formed in O–O collisions. Measurements at both central and forward rapidity could disentangle the role of these two effects. The projected statistical and systematic uncertainties are similar and they range range from 5–10% at low p_{T} to 20% at 10 GeV/c.
- Production measurements of strange hadrons, light nuclei and hypernuclei in multiplicity classes in O–O collisions cover a range in multiplicity that overlap both with pp collisions, on the low side, and with peripheral Pb–Pb collisions, on the high side. The statistical precision for strange hadrons, deuteron and ^{3}He will enable detailed comparisons with the other colliding systems.
- The pilot O–O run offers a unique possibility to investigate the origin of the particle flow in small collision systems. The advantage of O–O collisions is the wide coverage at low event multiplicities ($20 < N_{\mathrm{ch}}(|\eta| < 0.8) < 250$) combined with a well-controlled initial-state geometry. The

measurements allow quantitative comparisons with both the results in pp, p–Pb and Pb–Pb collisions, and hydrodynamic models. The measurement of the correlation between v_2^2 and $\langle p_{\mathrm{T}} \rangle$ is of particular interest, because the expected precision can be sufficient to elucidate the role of possible initial-state momentum correlations arising from gluon saturation effects.

- O–O collisions can provide important insight on the study of the strong interaction potential between pairs of hadrons, using momentum correlations of pairs produced with small spatial and momentum distance. With respect to pp and p–Pb collisions, O–O collisions provide a larger hadron source size (typically 2–3 fm, compared to 1 fm for pp and p–Pb). For example, this feature gives access, for p–K pairs, to the role of coupled channels (which open up as the interaction distance increases), for baryon–antibaryon pairs to the annihilation dynamics, and for p–Ω^- pairs to the possible existence of a bound state.
- Measurements of the photoproduction of ρ^0 vector mesons can be carried out with high precision and the small size of oxygen enables the separation of the incoherent production from the coherent production, which is instead completely dominant for lead and xenon. In addition, measurements of the $f_2(1270)$ and $f_0(980)$ states in diffractive O–O collisions provide insight on the A-dependence of the double-Pomeron fusion process.

Acknowledgements

The ALICE Collaboration would like to thank all its engineers and technicians for their invaluable contributions to the construction of the experiment and the CERN accelerator teams for the outstanding performance of the LHC complex. The ALICE Collaboration gratefully acknowledges the resources and support provided by all Grid centres and the Worldwide LHC Computing Grid (WLCG) collaboration. The ALICE Collaboration acknowledges the following funding agencies for their support in building and running the ALICE detector: A. I. Alikhanyan National Science Laboratory (Yerevan Physics Institute) Foundation (ANSL), State Committee of Science and World Federation of Scientists (WFS), Armenia; Austrian Academy of Sciences, Austrian Science Fund (FWF): [M 2467-N36] and Nationalstiftung für Forschung, Technologie und Entwicklung, Austria; Ministry of Communications and High Technologies, National Nuclear Research Center, Azerbaijan; Conselho Nacional de Desenvolvimento Científico e Tecnológico (CNPq), Financiadora de Estudos e Projetos (Finep), Fundação de Amparo à Pesquisa do Estado de São Paulo (FAPESP) and Universidade Federal do Rio Grande do Sul (UFRGS), Brazil; Ministry of Education of China (MOEC) , Ministry of Science & Technology of China (MSTC) and National Natural Science Foundation of China (NSFC), China; Ministry of Science and Education and Croatian Science Foundation, Croatia; Centro de Aplicaciones Tecnológicas y Desarrollo Nuclear (CEADEN), Cubaenergía, Cuba; Ministry of Education, Youth and Sports of the Czech Republic, Czech Republic; The Danish Council for Independent Research | Natural Sciences, the VILLUM FONDEN and Danish National Research Foundation (DNRF), Denmark; Helsinki Institute of Physics (HIP), Finland; Commissariat à l'Energie Atomique (CEA) and Institut National de Physique Nucléaire et de Physique des Particules (IN2P3) and Centre National de la Recherche Scientifique (CNRS), France; Bundesministerium für Bildung und Forschung (BMBF) and GSI Helmholtzzentrum für Schwerionenforschung GmbH, Germany; General Secretariat for Research and Technology, Ministry of Education, Research and Religions, Greece; National Research, Development and Innovation Office, Hungary; Department of Atomic Energy Government of India (DAE), Department of Science and Technology, Government of India (DST), University Grants Commission, Government of India (UGC) and Council of Scientific and Industrial Research (CSIR), India; Indonesian Institute of Science, Indonesia; Istituto Nazionale di Fisica Nucleare (INFN), Italy; Institute for Innovative Science and Technology , Nagasaki Institute of Applied Science (IIST), Japanese Ministry of Education, Culture, Sports, Science and Technology (MEXT) and Japan Society for the Promotion of Science (JSPS) KAKENHI, Japan; Consejo Nacional de Ciencia (CONACYT) y Tecnología, through Fondo de Cooperación Internacional en Ciencia y Tecnología (FONCICYT) and Dirección General de Asuntos del Personal Academico (DGAPA), Mexico; Nederlandse Organisatie voor Wetenschappelijk Onderzoek (NWO), Netherlands; The Research Council of Norway, Norway; Commission on Science and Technology for Sustainable Development in the South (COMSATS), Pakistan; Pontificia Universidad Católica del Perú, Peru; Ministry of Education and Science, National Science Centre and WUT ID-UB, Poland; Korea Institute of Science and Technology Information and National Research Foundation of Korea (NRF), Republic of Korea; Ministry of Education and Scientific Research, Institute of Atomic Physics and Ministry of Research and Innovation and Institute of Atomic Physics, Romania; Joint Institute for Nuclear Research (JINR), Ministry of Education and Science of the Russian Federation, National Research Centre Kurchatov Institute, Russian Science Foundation and Russian Foundation for Basic Research, Russia; Ministry of Education, Science, Research and Sport of the Slovak Republic, Slovakia; National Research Foundation of South Africa, South Africa; Swedish Research Council (VR) and Knut & Alice Wallenberg Foundation (KAW), Sweden; European Organization for Nuclear Research, Switzerland; Suranaree University of Technology (SUT), National Science and Technology Development Agency (NSDTA) and Office of the Higher Education Commission under NRU project of Thailand, Thailand; Turkish Energy, Nuclear and Mineral Research Agency (TENMAK), Turkey; National Academy of Sciences of Ukraine, Ukraine; Science and Technology Facilities Council (STFC), United Kingdom; National Science Foundation of the United States of America (NSF) and United States Department of Energy, Office of Nuclear Physics (DOE NP), United States of America.

References

[1] *Opportunities of O–O and p–O collisions at the LHC, CERN, 4-10 February 2021*, `https://indico.cern.ch/event/975877`.

[2] J. Brewer, A. Mazeliauskas, and W. van der Schee 3, 2021. `arXiv:2103.01939 [hep-ph]`.

[3] ALICE Collaboration, J. Adam et al. Nature Physics **13** (2017) .

[4] ALICE Collaboration, S. Acharya et al. Phys. Rev. Lett. **123** (2019) no. 14, 142301, `arXiv:1903.01790 [nucl-ex]`.

[5] ALICE Collaboration, S. Acharya et al. Phys. Lett. B **783** (2018) 95–113, `arXiv:1712.05603 [nucl-ex]`.

[6] ALICE Collaboration, S. Acharya et al. JHEP **11** (2018) 013, `arXiv:1802.09145 [nucl-ex]`.

[7] R. Bruce, *LHC machine scenario for a short oxygen run, 4 February 2021*, `https://indico.cern.ch/event/975877/contributions/4110095/`.

[8] A. Huss, A. Kurkela, A. Mazeliauskas, et al. `arXiv:2007.13758 [hep-ph]`.

[9] M. L. Miller, K. Reygers, S. J. Sanders, and P. Steinberg Ann. Rev. Nucl. Part. Sci. **57** (2007) 205. `https://doi.org/10.1146/annurev.nucl.57.090506.123020`.

[10] A. Huss, A. Kurkela, A. Mazeliauskas, et al. `arXiv:2007.13754 [hep-ph]`.

[11] ALICE Collaboration, B. Abelev et al. CERN-LHCC-2013-019, CERN, 2013. `https://cds.cern.ch/record/1603472/`.

[12] S. van der Meer CERN-ISR-PO-68-31. ISR-PO-68-31, CERN, Geneva, 1968. `http://cds.cern.ch/record/296752`.

[13] ALICE Collaboration, S. Acharya et al. ALICE-PUBLIC-2018-002, CERN, 2018. `https://cds.cern.ch/record/2314660/`.

[14] ALICE Collaboration, S. Acharya et al. ALICE-PUBLIC-2021-001, CERN, 2021. `https://cds.cern.ch/record/2749127/`.

[15] C. Bierlich, G. Gustafson, L. Lönnblad, and H. Shah JHEP **10** (2018) 134, `arXiv:1806.10820 [hep-ph]`.

[16] H. De Vries, C. De Jager, and C. De Vries Atomic Data and Nuclear Data Tables **36** (1987) no. 3, 495–536. `https://www.sciencedirect.com/science/article/pii/0092640X87900131`.

[17] ALICE Collaboration, S. Acharya et al. ALICE-PUBLIC-2018-002, 2018. `https://cds.cern.ch/record/2636623`.

[18] D. d'Enterria and C. Loizides `arXiv:2011.14909 [hep-ph]`.

[19] C. Loizides, J. Kamin, and D. d'Enterria Phys. Rev. C **97** (2018) no. 5, 054910, `arXiv:1710.07098 [nucl-ex]`. [Erratum: Phys.Rev.C 99, 019901 (2019)].

[20] ALICE Collaboration, S. Acharya et al. Phys. Lett. B **790** (2019) 35–48, `arXiv:1805.04432 [nucl-ex]`.

[21] ALICE Collaboration, J. Adam et al. Phys. Rev. Lett. **116** (2016) no. 22, 222302, `arXiv:1512.06104 [nucl-ex]`.

[22] C. Loizides and A. Morsch Phys. Lett. B **773** (2017) 408–411, `arXiv:1705.08856 [nucl-ex]`.

[23] ALICE Collaboration, B. Abelev et al. Eur. Phys. J. C **73** (2013) no. 12, 2662, `arXiv:1307.1093 [nucl-ex]`.

[24] M. Cacciari, G. P. Salam, and G. Soyez JHEP **04** (2008) 063, `arXiv:0802.1189 [hep-ph]`.

[25] M. Cacciari and G. P. Salam Phys.Lett.B **659** (2008) 119–126, `arXiv:0707.1378 [hep-ph]`.

[26] ALICE Collaboration, J. Adam et al. JHEP **09** (2015) 170, `arXiv:1506.03984 [nucl-ex]`.

[27] P. Skands, S. Carrazza, and J. Rojo (2014) , `arXiv:1404.5630 [hep-ph]`.

[28] ALICE Collaboration, S. Acharya et al. ALICE-PUBLIC-2019-001, CERN, 2019. `http://cds.cern.ch/record/2661798`.

[29] ALICE Collaboration, S. Acharya et al. JHEP **10** (2018) 174, `arXiv:1804.09083 [nucl-ex]`.

[30] ALICE Collaboration, S. Acharya et al. JHEP **12** (2019) 092, `arXiv:1906.03425 [nucl-ex]`.

[31] R. Katz, C. A. G. Prado, J. Noronha-Hostler, and A. A. P. Suaide Phys. Rev. C **102** (2020) no. 4, 041901, `arXiv:1907.03308 [nucl-th]`.

[32] C. A. G. Prado, J. Noronha-Hostler, R. Katz, et al. Phys. Rev. C **96** (2017) no. 6, 064903, `arXiv:1611.02965 [nucl-th]`.

[33] J. S. Moreland, J. E. Bernhard, and S. A. Bass Phys. Rev. C **92** (2015) no. 1, 011901, `arXiv:1412.4708 [nucl-th]`.

[34] J. Noronha-Hostler, G. S. Denicol, J. Noronha, R. P. G. Andrade, and F. Grassi Phys. Rev. C **88** (2013) no. 4, 044916, `arXiv:1305.1981 [nucl-th]`.

[35] J. Noronha-Hostler, J. Noronha, and F. Grassi Phys. Rev. C **90** (2014) no. 3, 034907, `arXiv:1406.3333 [nucl-th]`.

[36] ALICE Collaboration, B. Abelev et al. J. Phys. G **41** (2014) 087002.

[37] ALICE Collaboration, S. Acharya et al. `arXiv:2102.13601 [nucl-ex]`.

[38] ALICE Collaboration, S. Acharya et al. Eur. Phys. J. C **79** (2019) no. 5, 388, `arXiv:1901.07979 [nucl-ex]`.

[39] ALICE Collaboration, S. Acharya et al. Eur. Phys. J. C **77** (2017) no. 8, 550, `arXiv:1702.00766 [hep-ex]`.

[40] M. Cacciari, M. Greco, and P. Nason JHEP **05** (1998) 007, `arXiv:hep-ph/9803400 [hep-ph]`.

[41] M. Cacciari, S. Frixione, and P. Nason JHEP **03** (2001) 006, `arXiv:hep-ph/0102134 [hep-ph]`.

[42] ALICE Collaboration, B. Abelev et al. JHEP **07** (2012) 191, `arXiv:1205.4007 [hep-ex]`.

[43] LHCb Collaboration, R. Aaij et al. JHEP **06** (2017) 147, `arXiv:1610.02230 [hep-ex]`.

[44] LHCb Collaboration, R. Aaij et al. Nucl. Phys. B **871** (2013) 1–20, `arXiv:1302.2864 [hep-ex]`.

[45] LHCb Collaboration, R. Aaij et al. JHEP **03** (2016) 159, `arXiv:1510.01707 [hep-ex]`.

[Erratum: JHEP 09, 013 (2016), Erratum: JHEP 05, 074 (2017)].

[46] T. Sjöstrand, S. Ask, J. R. Christiansen, et al. Comput. Phys. Commun. **191** (2015) 159–177, `arXiv:1410.3012 [hep-ph]`.

[47] ALICE Collaboration, J. Adam et al. Eur. Phys. J. C **77** (2017) no. 4, 245, `arXiv:1605.06963 [nucl-ex]`.

[48] ALICE Collaboration, S. Acharya et al. Eur. Phys. J. C **80** (2020) no. 10, 979, `arXiv:1910.14403 [nucl-ex]`.

[49] T. Matsui and H. Satz Physics Letters B **178** (1986) no. 4, 416–422. `https://www.sciencedirect.com/science/article/pii/0370269386914048`.

[50] M. Laine, O. Philipsen, P. Romatschke, and M. Tassler JHEP **03** (2007) 054, `arXiv:hep-ph/0611300`.

[51] P. Braun-Munzinger and J. Stachel Phys. Lett. B **490** (2000) 196–202, `arXiv:nucl-th/0007059`.

[52] R. L. Thews, M. Schroedter, and J. Rafelski Phys. Rev. C **63** (2001) 054905. `https://link.aps.org/doi/10.1103/PhysRevC.63.054905`.

[53] ALICE Collaboration, S. Acharya et al. JHEP **10** (2020) 141, `arXiv:2005.14518 [nucl-ex]`.

[54] F. Bossu, Z. C. del Valle, A. de Falco, et al. `arXiv:1103.2394 [nucl-ex]`.

[55] ALICE Collaboration, S. Acharya et al. Phys. Lett. B **805** (2020) 135434, `arXiv:1910.14404 [nucl-ex]`.

[56] PHENIX Collaboration, A. Adare et al. Phys. Rev. Lett. **98** (2007) 232002. `https://link.aps.org/doi/10.1103/PhysRevLett.98.232002`.

[57] CDF Collaboration, D. Acosta et al. Phys. Rev. D **71** (2005) 032001. `https://link.aps.org/doi/10.1103/PhysRevD.71.032001`.

[58] ALICE Collaboration, B. Abelev et al. Phys. Lett. B **718** (2012) 295–306, `arXiv:1203.3641 [hep-ex]`. [Erratum: Phys.Lett.B 748, 472–473 (2015)].

[59] ALICE Collaboration, S. Acharya et al. JHEP **10** (2019) 084, `arXiv:1905.07211 [nucl-ex]`.

[60] ALICE Collaboration, K. Aamodt et al. Phys. Lett. B **704** (2011) 442–455. 14 p.

[61] A. Andronic, P. Braun-Munzinger, M. K. Köhler, K. Redlich, and J. Stachel Phys. Lett. B **797** (2019) 134836, `arXiv:1901.09200 [nucl-th]`.

[62] ALICE Collaboration, B. Abelev et al. Eur. Phys. J. C **74** (2014) no. 8, 2974, `arXiv:1403.3648 [nucl-ex]`.

[63] ALICE Collaboration, S. Acharya et al. JHEP **07** (2018) 160, `arXiv:1805.04381 [nucl-ex]`.

[64] ALICE Collaboration, S. Acharya et al. JHEP **02** (2020) 041, `arXiv:1909.03158 [nucl-ex]`.

[65] ALICE Collaboration, S. Acharya et al. Eur. Phys. J. C **77** (2017) no. 6, 392, `arXiv:1702.00557 [hep-ex]`.

[66] ALICE Collaboration, S. Acharya et al. Phys.Rev.C **91** (2019(2)) .

[67] S. Acharya et al. The European Physical Journal C **80** (2020) no. 167, .

[68] ALICE Collaboration, S. Acharya et al. The European Physical Journal C **80** (2020) .

[69] ALICE Collaboration, S. Acharya et al. Physics Letters B **807** (2020) and others01. `https://www.sciencedirect.com/science/article/pii/S0370269320303051`.

[70] ALICE Collaboration, J. Adam et al. Physics Letters B **760** (2016) 720–735. `https://www.sciencedirect.com/science/article/pii/S0370269316303914`.

[71] ALICE Collaboration, J. Adam et al. Physics Letters B **758** (2016) 389–401. `https://www.sciencedirect.com/science/article/pii/S0370269316301745`.

[72] ALICE Collaboration, J. Adam et al. The European Physical Journal C **76** (2016) 245.

[73] ALICE Collaboration, B. Abelev et al.Phys. Rev. C **88** (Oct, 2013) 044910.

https://link.aps.org/doi/10.1103/PhysRevC.88.044910.

[74] ALICE Collaboration, B. Abelev et al.Phys. Rev. Lett. **111** (Nov, 2013) 222301. https://link.aps.org/doi/10.1103/PhysRevLett.111.222301.

[75] ALICE Collaboration, B. Abelev et al. Physics Letters B **728** (2014) 216–227. https://www.sciencedirect.com/science/article/pii/S0370269313009544.

[76] ALICE Collaboration, J. Adam et al.Phys. Rev. C **95** (Jun, 2017) 064606. https://link.aps.org/doi/10.1103/PhysRevC.95.064606.

[77] V. Vovchenko, B. Dönigus, and H. Stoecker Phys. Lett. B **785** (2018) 171–174, arXiv:1808.05245 [hep-ph].

[78] K.-J. Sun, C. M. Ko, and B. Dönigus Phys. Lett. B **792** (2019) 132–137, arXiv:1812.05175 [nucl-th].

[79] ALICE Collaboration, B. Abelev et al. Phys. Lett. B **726** (2013) 164–177, arXiv:1307.3237 [nucl-ex].

[80] P. Huovinen, P. F. Kolb, U. W. Heinz, P. V. Ruuskanen, and S. A. Voloshin Phys. Lett. B **503** (2001) 58–64, arXiv:hep-ph/0101136.

[81] A. Bilandzic, C. H. Christensen, K. Gulbrandsen, A. Hansen, and Y. Zhou Phys. Rev. C **89** (2014) no. 6, 064904, arXiv:1312.3572 [nucl-ex].

[82] B. Schenke, C. Shen, and P. Tribedy Phys. Rev. C **102** (2020) no. 4, 044905, arXiv:2005.14682 [nucl-th].

[83] Z. Moravcova, K. Gulbrandsen, and Y. Zhou Phys. Rev. C **103** (2021) no. 2, 024913, arXiv:2005.07974 [nucl-th].

[84] W. Zhao, C. M. Ko, Y.-X. Liu, G.-Y. Qin, and H. Song Phys. Rev. Lett. **125** (2020) no. 7, 072301, arXiv:1911.00826 [nucl-th].

[85] P. Huo, K. Gajdošová, J. Jia, and Y. Zhou Phys. Lett. B **777** (2018) 201–206, arXiv:1710.07567 [nucl-ex].

[86] P. Bozek Phys. Rev. C **93** (2016) no. 4, 044908, arXiv:1601.04513 [nucl-th].

[87] B. Schenke, P. Tribedy, and R. Venugopalan Phys. Rev. Lett. **108** (2012) 252301, arXiv:1202.6646 [nucl-th].

[88] C. Zhang, A. Behera, S. Bhatta, and J. Jia arXiv:2102.05200 [nucl-th].

[89] S. H. Lim and J. L. Nagle arXiv:2103.01348 [nucl-th].

[90] ALICE Collaboration, S. Acharya et al. Phys. Lett. B **797** (2019) 134822, arXiv:1905.07209 [nucl-ex].

[91] ALICE Collaboration, S. Acharya et al. Phys. Rev. Lett. **124** (2020) 092301, arXiv:1905.13470 [nucl-ex].

[92] ALICE Collaboration, S. Acharya et al. Nature **588** (2020) no. 7837, 232–238.

[93] ALICE Collaboration, S. Acharya et al. Phys. Lett. B **805** (2020) 135419, arXiv:1910.14407 [nucl-ex].

[94] ALICE Collaboration, S. Acharya et al. Phys. Rev. Lett. **123** (2019) 112002, arXiv:1904.12198 [nucl-ex].

[95] K. Morita, A. Ohnishi, F. Etminan, and T. Hatsuda Phys. Rev. C **94** (2016) no. 3, 031901, arXiv:1605.06765 [hep-ph]. [Erratum: Phys.Rev.C 100, 069902 (2019)].

[96] J. Haidenbauer Nucl. Phys. **A981** (2019) 1–16, arXiv:1808.05049 [hep-ph].

[97] Y. Kamiya, T. Hyodo, K. Morita, A. Ohnishi, and W. Weise Phys. Rev. Lett. **124** (2020) no. 13, 132501, arXiv:1911.01041 [nucl-th].

[98] ALICE Collaboration, K. Aamodt et al. Phys. Rev. D **84** (2011) 112004, arXiv:1101.3665 [hep-ex].

[99] ALICE Collaboration, K. Aamodt et al. Phys. Lett. B **696** (2011) 328–337, `arXiv:1012.4035 [nucl-ex]`.

[100] ALICE Collaboration, J. Adam et al. Phys. Rev. C **91** (2015) 034906, `arXiv:1502.00559 [nucl-ex]`.

[101] T. Pierog, I. Karpenko, J. Katzy, E. Yatsenko, and K. Werner Phys. Rev. C **92** (2015) no. 3, 034906, `arXiv:1306.0121 [hep-ph]`.

[102] E. Klempt, F. Bradamante, A. Martin, and J. M. Richard Phys. Rept. **368** (2002) 119–316.

[103] E. Klempt, C. Batty, and J.-M. Richard Phys. Rept. **413** (2005) 197–317, `arXiv:hep-ex/0501020`.

[104] BES Collaboration, J. Z. Bai et al. Phys. Rev. Lett. **91** (2003) 022001, `arXiv:hep-ex/0303006`.

[105] BaBar Collaboration, B. Aubert et al. Phys. Rev. D **72** (2005) 051101, `arXiv:hep-ex/0507012`.

[106] BaBar Collaboration, B. Aubert et al. Phys. Rev. D **73** (2006) 012005, `arXiv:hep-ex/0512023`.

[107] BESIII Collaboration, M. Ablikim et al. Phys. Rev. Lett. **108** (2012) 112003, `arXiv:1112.0942 [hep-ex]`.

[108] J. Haidenbauer, U.-G. Meißner, and A. Nogga Eur. Phys. J. A **56** (2020) 91, `arXiv:1906.11681 [nucl-th]`.

[109] L.-Y. Dai, J. Haidenbauer, and U.-G. Meißner JHEP **07** (2017) 078, `arXiv:1702.02065 [nucl-th]`.

[110] J. Haidenbauer, C. Hanhart, X.-W. Kang, and U.-G. Meißner Phys. Rev. D **92** (2015) no. 5, 054032, `arXiv:1506.08120 [nucl-th]`.

[111] ALICE Collaboration, S. Acharya et al. Phys. Lett. **B802** (2020) 135223, `arXiv:1903.06149 [nucl-ex]`.

[112] ALICE Collaboration, S. Acharya et al. Phys. Rev. Lett. **124** (2020) no. 9, 092301, `arXiv:1905.13470 [nucl-ex]`.

[113] HAL QCD Collaboration, T. Iritani et al. Phys. Lett. B **792** (2019) 284–289.

[114] T. Sekihara, Y. Kamiya, and T. Hyodo Phys. Rev. **C98** (2018) no. 1, 015205, `arXiv:1805.04024 [hep-ph]`.

[115] K. Morita, S. Gongyo, T. Hatsuda, et al. Phys. Rev. C **101** (2020) 015201.

[116] J. Haidenbauer Phys. Rev. C **102** (2020) no. 3, 034001, `arXiv:2005.05012 [nucl-th]`.

[117] I. A. Pshenichnov, I. N. Mishustin, J. P. Bondorf, A. S. Botvina, and A. S. Iljinov Phys. Rev. C **57** (1998) 1920–1926. `http://dx.doi.org/10.1103/PhysRevC.57.1920`.

[118] A. J. Baltz Phys. Rept. **458** (2008) 1–171, `arXiv:0706.3356 [nucl-ex]`.

[119] J. G. Contreras and J. D. Tapia Takaki Int. J. Mod. Phys. A **30** (2015) 1542012.

[120] S. Klein and P. Steinberg Ann. Rev. Nucl. Part. Sci. **70** (2020) 323–354, `arXiv:2005.01872 [nucl-ex]`.

[121] J. Cepila, J. G. Contreras, M. Krelina, and J. D. Tapia Takaki Nucl. Phys. B **934** (2018) 330–340, `arXiv:1804.05508 [hep-ph]`.

[122] S. R. Klein and H. Mäntysaari Nature Rev. Phys. **1** (2019) no. 11, 662–674, `arXiv:1910.10858 [hep-ex]`.

[123] S. R. Klein, J. Nystrand, J. Seger, Y. Gorbunov, and J. Butterworth Comput. Phys. Commun. **212** (2017) 258–268, `arXiv:1607.03838 [hep-ph]`.

[124] S. Klein and J. Nystrand Phys. Rev. C **60** (1999) 014903, `arXiv:hep-ph/9902259`.

[125] ALICE Collaboration, S. Acharya et al. `arXiv:2101.04577 [nucl-ex]`.

[126] ALICE Collaboration, S. Acharya et al. `arXiv:2101.02581 [nucl-ex]`.

[127] STAR Collaboration, B. Abelev et al. Phys. Rev. C **77** (2008) 034910, `arXiv:0712.3320 [nucl-ex]`.

[128] S. R. Klein and J. Nystrand Phys. Rev. Lett. **84** (2000) 2330–2333, `arXiv:hep-ph/9909237`.

[129] STAR Collaboration, B. Abelev et al. Phys. Rev. Lett. **102** (2009) 112301, `arXiv:0812.1063 [nucl-ex]`.

[130] B. Muller and A. J. Schramm Nucl. Phys. A **523** (1991) 677–693.

[131] Helios Collaboration, T. Åkesson et al. Z. Phys. C **49** (1991) 355–366.

[132] V. Cavasinni, T. Del Prete, M. Morganti, et al. Z. Phys. C **28** (1985) 487.

A The ALICE Collaboration

S. Acharya[143], D. Adamová[98], A. Adler[76], J. Adolfsson[83], G. Aglieri Rinella[35], M. Agnello[31], N. Agrawal[55], Z. Ahammed[143], S. Ahmad[16], S.U. Ahn[78], I. Ahuja[39], Z. Akbar[52], A. Akindinov[95], M. Al-Turany[110], S.N. Alam[41], D. Aleksandrov[91], B. Alessandro[61], H.M. Alfanda[7], R. Alfaro Molina[73], B. Ali[16], Y. Ali[14], A. Alici[26], N. Alizadehvandchali[127], A. Alkin[35], J. Alme[21], T. Alt[70], L. Altenkamper[21], I. Altsybeev[115], M.N. Anaam[7], C. Andrei[49], D. Andreou[93], A. Andronic[146], M. Angeletti[35], V. Anguelov[107], F. Antinori[58], P. Antonioli[55], C. Anuj[16], N. Apadula[82], L. Aphecetche[117], H. Appelshäuser[70], S. Arcelli[26], R. Arnaldi[61], I.C. Arsene[20], M. Arslandok[148,107], A. Augustinus[35], R. Averbeck[110], S. Aziz[80], M.D. Azmi[16], A. Badalà[57], Y.W. Baek[42], X. Bai[131,110], R. Bailhache[70], Y. Bailung[51], R. Bala[104], A. Balbino[31], A. Baldisseri[140], B. Balis[2], M. Ball[44], D. Banerjee[4], R. Barbera[27], L. Barioglio[108,25], M. Barlou[87], G.G. Barnaföldi[147], L.S. Barnby[97], V. Barret[137], C. Bartels[130], K. Barth[35], E. Bartsch[70], F. Baruffaldi[28], N. Bastid[137], S. Basu[83], G. Batigne[117], B. Batyunya[77], D. Bauri[50], J.L. Bazo Alba[114], I.G. Bearden[92], C. Beattie[148], I. Belikov[139], A.D.C. Bell Hechavarria[146], F. Bellini[26,35], R. Bellwied[127], S. Belokurova[115], V. Belyaev[96], G. Bencedi[71], S. Beole[25], A. Bercuci[49], Y. Berdnikov[101], A. Berdnikova[107], D. Berenyi[147], L. Bergmann[107], M.G. Besoiu[69], L. Betev[35], P.P. Bhaduri[143], A. Bhasin[104], M.A. Bhat[4], B. Bhattacharjee[43], P. Bhattacharya[23], L. Bianchi[25], N. Bianchi[53], J. Bielčík[38], J. Bielčíková[98], J. Biernat[120], A. Bilandzic[108], G. Biro[147], S. Biswas[4], J.T. Blair[121], D. Blau[91], M.B. Blidaru[110], C. Blume[70], G. Boca[29,59], F. Bock[99], A. Bogdanov[96], S. Boi[23], J. Bok[63], L. Boldizsár[147], A. Bolozdynya[96], M. Bombara[39], P.M. Bond[35], G. Bonomi[142,59], H. Borel[140], A. Borissov[84], H. Bossi[148], E. Botta[25], L. Bratrud[70], P. Braun-Munzinger[110], M. Bregant[123], M. Broz[38], G.E. Bruno[109,34], M.D. Buckland[130], D. Budnikov[111], H. Buesching[70], S. Bufalino[31], O. Bugnon[117], P. Buhler[116], Z. Buthelezi[74,134], J.B. Butt[14], S.A. Bysiak[120], D. Caffarri[93], M. Cai[28,7], H. Caines[148], A. Caliva[110], E. Calvo Villar[114], J.M.M. Camacho[122], R.S. Camacho[46], P. Camerini[24], F.D.M. Canedo[123], F. Carnesecchi[35,26], R. Caron[140], J. Castillo Castellanos[140], E.A.R. Casula[23], F. Catalano[31], C. Ceballos Sanchez[77], P. Chakraborty[50], S. Chandra[143], S. Chapeland[35], M. Chartier[130], S. Chattopadhyay[143], S. Chattopadhyay[112], A. Chauvin[23], T.G. Chavez[46], C. Cheshkov[138], B. Cheynis[138], V. Chibante Barroso[35], D.D. Chinellato[124], S. Cho[63], P. Chochula[35], P. Christakoglou[93], C.H. Christensen[92], P. Christiansen[83], T. Chujo[136], C. Cicalo[56], L. Cifarelli[26], F. Cindolo[55], M.R. Ciupek[110], G. Clai[II,55], J. Cleymans[I,126], F. Colamaria[54], J.S. Colburn[113], D. Colella[109,54,34,147], A. Collu[82], M. Colocci[35,26], M. Concas[III,61], G. Conesa Balbastre[81], Z. Conesa del Valle[80], G. Contin[24], J.G. Contreras[38], M.L. Coquet[140], T.M. Cormier[99], P. Cortese[32], M.R. Cosentino[125], F. Costa[35], S. Costanza[29,59], P. Crochet[137], E. Cuautle[71], P. Cui[7], L. Cunqueiro[99], A. Dainese[58], F.P.A. Damas[117,140], M.C. Danisch[107], A. Danu[69], I. Das[112], P. Das[89], P. Das[4], S. Das[4], S. Dash[50], S. De[89], A. De Caro[30], G. de Cataldo[54], L. De Cilladi[25], J. de Cuveland[40], A. De Falco[23], D. De Gruttola[30], N. De Marco[61], C. De Martin[24], S. De Pasquale[30], S. Deb[51], H.F. Degenhardt[123], K.R. Deja[144], L. Dello Stritto[30], S. Delsanto[25], W. Deng[7], P. Dhankher[19], D. Di Bari[34], A. Di Mauro[35], R.A. Diaz[8], T. Dietel[126], Y. Ding[138,7], R. Divià[35], D.U. Dixit[19], Ø. Djuvsland[21], U. Dmitrieva[65], J. Do[63], A. Dobrin[69], B. Dönigus[70], O. Dordic[20], A.K. Dubey[143], A. Dubla[110,93], S. Dudi[103], M. Dukhishyam[89], P. Dupieux[137], N. Dzalaiova[13], T.M. Eder[146], R.J. Ehlers[99], V.N. Eikeland[21], D. Elia[54], B. Erazmus[117], F. Ercolessi[26], F. Erhardt[102], A. Erokhin[115], M.R. Ersdal[21], B. Espagnon[80], G. Eulisse[35], D. Evans[113], S. Evdokimov[94], L. Fabbietti[108], M. Faggin[28], J. Faivre[81], F. Fan[7], A. Fantoni[53], M. Fasel[99], P. Fecchio[31], A. Feliciello[61], G. Feofilov[115], A. Fernández Téllez[46], A. Ferrero[140], A. Ferretti[25], V.J.G. Feuillard[107], J. Figiel[120], S. Filchagin[111], D. Finogeev[65], F.M. Fionda[56,21], G. Fiorenza[35,109], F. Flor[127], A.N. Flores[121], S. Foertsch[74], P. Foka[110], S. Fokin[91], E. Fragiacomo[62], E. Frajna[147], U. Fuchs[35], N. Funicello[30], C. Furget[81], A. Furs[65], J.J. Gaardhøje[92], M. Gagliardi[25], A.M. Gago[114], A. Gal[139], C.D. Galvan[122], P. Ganoti[87], C. Garabatos[110], J.R.A. Garcia[46], E. Garcia-Solis[10], K. Garg[117], C. Gargiulo[35], A. Garibli[90], K. Garner[146], P. Gasik[110], E.F. Gauger[121], A. Gautam[129], M.B. Gay Ducati[72], M. Germain[117], J. Ghosh[112], P. Ghosh[143],

S.K. Ghosh[4], M. Giacalone[26], P. Gianotti[53], P. Giubellino[110,61], P. Giubilato[28], A.M.C. Glaenzer[140], P. Glässel[107], D.J.Q. Goh[85], V. Gonzalez[145], L.H. González-Trueba[73], S. Gorbunov[40], M. Gorgon[2], L. Görlich[120], S. Gotovac[36], V. Grabski[73], L.K. Graczykowski[144], L. Greiner[82], A. Grelli[64], C. Grigoras[35], V. Grigoriev[96], A. Grigoryan[I,1], S. Grigoryan[77,1], O.S. Groettvik[21], F. Grosa[35,61], J.F. Grosse-Oetringhaus[35], R. Grosso[110], G.G. Guardiano[124], R. Guernane[81], M. Guilbaud[117], K. Gulbrandsen[92], T. Gunji[135], A. Gupta[104], R. Gupta[104], S.P. Guzman[46], L. Gyulai[147], M.K. Habib[110], C. Hadjidakis[80], G. Halimoglu[70], H. Hamagaki[85], G. Hamar[147], M. Hamid[7], R. Hannigan[121], M.R. Haque[144,89], A. Harlenderova[110], J.W. Harris[148], A. Harton[10], J.A. Hasenbichler[35], H. Hassan[99], D. Hatzifotiadou[55], P. Hauer[44], L.B. Havener[148], S. Hayashi[135], S.T. Heckel[108], E. Hellbär[70], H. Helstrup[37], T. Herman[38], E.G. Hernandez[46], G. Herrera Corral[9], F. Herrmann[146], K.F. Hetland[37], H. Hillemanns[35], C. Hills[130], B. Hippolyte[139], B. Hofman[64], B. Hohlweger[93,108], J. Honermann[146], G.H. Hong[149], D. Horak[38], S. Hornung[110], A. Horzyk[2], R. Hosokawa[15], P. Hristov[35], C. Huang[80], C. Hughes[133], P. Huhn[70], T.J. Humanic[100], H. Hushnud[112], L.A. Husova[146], A. Hutson[127], D. Hutter[40], J.P. Iddon[35,130], R. Ilkaev[111], H. Ilyas[14], M. Inaba[136], G.M. Innocenti[35], M. Ippolitov[91], A. Isakov[38,98], M.S. Islam[112], M. Ivanov[110], V. Ivanov[101], V. Izucheev[94], M. Jablonski[2], B. Jacak[82], N. Jacazio[35], P.M. Jacobs[82], S. Jadlovska[119], J. Jadlovsky[119], S. Jaelani[64], C. Jahnke[124,123], M.J. Jakubowska[144], A. Jalotra[104], M.A. Janik[144], T. Janson[76], M. Jercic[102], O. Jevons[113], F. Jonas[99,146], P.G. Jones[113], J.M. Jowett [35,110], J. Jung[70], M. Jung[70], A. Junique[35], A. Jusko[113], J. Kaewjai[118], P. Kalinak[66], A. Kalweit[35], V. Kaplin[96], S. Kar[7], A. Karasu Uysal[79], D. Karatovic[102], O. Karavichev[65], T. Karavicheva[65], P. Karczmarczyk[144], E. Karpechev[65], A. Kazantsev[91], U. Kebschull[76], R. Keidel[48], D.L.D. Keijdener[64], M. Keil[35], B. Ketzer[44], Z. Khabanova[93], A.M. Khan[7], S. Khan[16], A. Khanzadeev[101], Y. Kharlov[94], A. Khatun[16], A. Khuntia[120], B. Kileng[37], B. Kim[17,63], C. Kim[17], D. Kim[149], D.J. Kim[128], E.J. Kim[75], J. Kim[149], J.S. Kim[42], J. Kim[107], J. Kim[149], J. Kim[75], M. Kim[107], S. Kim[18], T. Kim[149], S. Kirsch[70], I. Kisel[40], S. Kiselev[95], A. Kisiel[144], J.P. Kitowski[2], J.L. Klay[6], J. Klein[35], S. Klein[82], C. Klein-Bösing[146], M. Kleiner[70], T. Klemenz[108], A. Kluge[35], A.G. Knospe[127], C. Kobdaj[118], M.K. Köhler[107], T. Kollegger[110], A. Kondratyev[77], N. Kondratyeva[96], E. Kondratyuk[94], J. Konig[70], S.A. Konigstorfer[108], P.J. Konopka[35,2], G. Kornakov[144], S.D. Koryciak[2], L. Koska[119], A. Kotliarov[98], O. Kovalenko[88], V. Kovalenko[115], M. Kowalski[120], I. Králik[66], A. Kravčáková[39], L. Kreis[110], M. Krivda[113,66], F. Krizek[98], K. Krizkova Gajdosova[38], M. Kroesen[107], M. Krüger[70], E. Kryshen[101], M. Krzewicki[40], V. Kučera[35], C. Kuhn[139], P.G. Kuijer[93], T. Kumaoka[136], D. Kumar[143], L. Kumar[103], N. Kumar[103], S. Kundu[35,89], P. Kurashvili[88], A. Kurepin[65], A.B. Kurepin[65], A. Kuryakin[111], S. Kushpil[98], J. Kvapil[113], M.J. Kweon[63], J.Y. Kwon[63], Y. Kwon[149], S.L. La Pointe[40], P. La Rocca[27], Y.S. Lai[82], A. Lakrathok[118], M. Lamanna[35], R. Langoy[132], K. Lapidus[35], P. Larionov[53], E. Laudi[35], L. Lautner[35,108], R. Lavicka[38], T. Lazareva[115], R. Lea[142,24,59], J. Lehrbach[40], R.C. Lemmon[97], I. León Monzón[122], E.D. Lesser[19], M. Lettrich[35,108], P. Lévai[147], X. Li[11], X.L. Li[7], J. Lien[132], R. Lietava[113], B. Lim[17], S.H. Lim[17], V. Lindenstruth[40], A. Lindner[49], C. Lippmann[110], A. Liu[19], J. Liu[130], I.M. Lofnes[21], V. Loginov[96], C. Loizides[99], P. Loncar[36], J.A. Lopez[107], X. Lopez[137], E. López Torres[8], J.R. Luhder[146], M. Lunardon[28], G. Luparello[62], Y.G. Ma[41], A. Maevskaya[65], M. Mager[35], T. Mahmoud[44], A. Maire[139], M. Malaev[101], N.M. Malik[104], Q.W. Malik[20], L. Malinina[IV,77], D. Mal'Kevich[95], N. Mallick[51], P. Malzacher[110], G. Mandaglio[33,57], V. Manko[91], F. Manso[137], V. Manzari[54], Y. Mao[7], J. Mareš[68], G.V. Margagliotti[24], A. Margotti[55], A. Marín[110], C. Markert[121], M. Marquard[70], N.A. Martin[107], P. Martinengo[35], J.L. Martinez[127], M.I. Martínez[46], G. Martínez García[117], S. Masciocchi[110], M. Masera[25], A. Masoni[56], L. Massacrier[80], A. Mastroserio[141,54], A.M. Mathis[108], O. Matonoha[83], P.F.T. Matuoka[123], A. Matyja[120], C. Mayer[120], A.L. Mazuecos[35], F. Mazzaschi[25], M. Mazzilli[35], M.A. Mazzoni[60], J.E. Mdhluli[134], A.F. Mechler[70], F. Meddi[22], Y. Melikyan[65], A. Menchaca-Rocha[73], E. Meninno[116,30], A.S. Menon[127], M. Meres[13], S. Mhlanga[126,74], Y. Miake[136], L. Micheletti[61,25], L.C. Migliorin[138], D.L. Mihaylov[108], K. Mikhaylov[77,95], A.N. Mishra[147], D. Miśkowiec[110], A. Modak[4], A.P. Mohanty[64], B. Mohanty[89], M. Mohisin Khan[16], Z. Moravcova[92], C. Mordasini[108], D.A. Moreira De Godoy[146], L.A.P. Moreno[46], I. Morozov[65], A. Morsch[35], T. Mrnjavac[35], V. Muccifora[53], E. Mudnic[36], D. Mühlheim[146],

S. Muhuri[143], J.D. Mulligan[82], A. Mulliri[23], M.G. Munhoz[123], R.H. Munzer[70], H. Murakami[135], S. Murray[126], L. Musa[35], J. Musinsky[66], J.W. Myrcha[144], B. Naik[134,50], R. Nair[88], B.K. Nandi[50], R. Nania[55], E. Nappi[54], M.U. Naru[14], A.F. Nassirpour[83], A. Nath[107], C. Nattrass[133], A. Neagu[20], L. Nellen[71], S.V. Nesbo[37], G. Neskovic[40], D. Nesterov[115], B.S. Nielsen[92], S. Nikolaev[91], S. Nikulin[91], V. Nikulin[101], F. Noferini[55], S. Noh[12], P. Nomokonov[77], J. Norman[130], N. Novitzky[136], P. Nowakowski[144], A. Nyanin[91], J. Nystrand[21], M. Ogino[85], A. Ohlson[83], V.A. Okorokov[96], J. Oleniacz[144], A.C. Oliveira Da Silva[133], M.H. Oliver[148], A. Onnerstad[128], C. Oppedisano[61], A. Ortiz Velasquez[71], T. Osako[47], A. Oskarsson[83], J. Otwinowski[120], K. Oyama[85], Y. Pachmayer[107], S. Padhan[50], D. Pagano[142,59], G. Paić[71], A. Palasciano[54], J. Pan[145], S. Panebianco[140], P. Pareek[143], J. Park[63], J.E. Parkkila[128], S.P. Pathak[127], R.N. Patra[104,35], B. Paul[23], J. Pazzini[142,59], H. Pei[7], T. Peitzmann[64], X. Peng[7], L.G. Pereira[72], H. Pereira Da Costa[140], D. Peresunko[91], G.M. Perez[8], S. Perrin[140], Y. Pestov[5], V. Petráček[38], M. Petrovici[49], R.P. Pezzi[72], S. Piano[62], M. Pikna[13], P. Pillot[117], O. Pinazza[55,35], L. Pinsky[127], C. Pinto[27], S. Pisano[53], M. Płoskoń[82], M. Planinic[102], F. Pliquett[70], M.G. Poghosyan[99], B. Polichtchouk[94], S. Politano[31], N. Poljak[102], A. Pop[49], S. Porteboeuf-Houssais[137], J. Porter[82], V. Pozdniakov[77], S.K. Prasad[4], R. Preghenella[55], F. Prino[61], C.A. Pruneau[145], I. Pshenichnov[65], M. Puccio[35], S. Qiu[93], L. Quaglia[25], R.E. Quishpe[127], S. Ragoni[113], A. Rakotozafindrabe[140], L. Ramello[32], F. Rami[139], S.A.R. Ramirez[46], A.G.T. Ramos[34], T.A. Rancien[81], R. Raniwala[105], S. Raniwala[105], S.S. Räsänen[45], R. Rath[51], I. Ravasenga[93], K.F. Read[99,133], A.R. Redelbach[40], K. Redlich[V,88], A. Rehman[21], P. Reichelt[70], F. Reidt[35], H.A. Reme-ness[37], R. Renfordt[70], Z. Rescakova[39], K. Reygers[107], A. Riabov[101], V. Riabov[101], T. Richert[83,92], M. Richter[20], W. Riegler[35], F. Riggi[27], C. Ristea[69], S.P. Rode[51], M. Rodríguez Cahuantzi[46], K. Røed[20], R. Rogalev[94], E. Rogochaya[77], T.S. Rogoschinski[70], D. Rohr[35], D. Röhrich[21], P.F. Rojas[46], P.S. Rokita[144], F. Ronchetti[53], A. Rosano[33,57], E.D. Rosas[71], A. Rossi[58], A. Rotondi[29,59], A. Roy[51], P. Roy[112], S. Roy[50], N. Rubini[26], O.V. Rueda[83], R. Rui[24], B. Rumyantsev[77], P.G. Russek[2], A. Rustamov[90], E. Ryabinkin[91], Y. Ryabov[101], A. Rybicki[120], H. Rytkonen[128], W. Rzesa[144], O.A.M. Saarimaki[45], R. Sadek[117], S. Sadovsky[94], J. Saetre[21], K. Šafařík[38], S.K. Saha[143], S. Saha[89], B. Sahoo[50], P. Sahoo[50], R. Sahoo[51], S. Sahoo[67], D. Sahu[51], P.K. Sahu[67], J. Saini[143], S. Sakai[136], S. Sambyal[104], V. Samsonov[I,101,96], D. Sarkar[145], N. Sarkar[143], P. Sarma[43], V.M. Sarti[108], M.H.P. Sas[148], J. Schambach[99,121], H.S. Scheid[70], C. Schiaua[49], R. Schicker[107], A. Schmah[107], C. Schmidt[110], H.R. Schmidt[106], M.O. Schmidt[107], M. Schmidt[106], N.V. Schmidt[99,70], A.R. Schmier[133], R. Schotter[139], J. Schukraft[35], Y. Schutz[139], K. Schwarz[110], K. Schweda[110], G. Scioli[26], E. Scomparin[61], J.E. Seger[15], Y. Sekiguchi[135], D. Sekihata[135], I. Selyuzhenkov[110,96], S. Senyukov[139], J.J. Seo[63], D. Serebryakov[65], L. Šerkšnytė[108], A. Sevcenco[69], T.J. Shaba[74], A. Shabanov[65], A. Shabetai[117], R. Shahoyan[35], W. Shaikh[112], A. Shangaraev[94], A. Sharma[103], H. Sharma[120], M. Sharma[104], N. Sharma[103], S. Sharma[104], U. Sharma[104], O. Sheibani[127], K. Shigaki[47], M. Shimomura[86], S. Shirinkin[95], Q. Shou[41], Y. Sibiriak[91], S. Siddhanta[56], T. Siemiarczuk[88], T.F. Silva[123], D. Silvermyr[83], G. Simonetti[35], B. Singh[108], R. Singh[89], R. Singh[104], R. Singh[51], V.K. Singh[143], V. Singhal[143], T. Sinha[112], B. Sitar[13], M. Sitta[32], T.B. Skaali[20], G. Skorodumovs[107], M. Slupecki[45], N. Smirnov[148], R.J.M. Snellings[64], C. Soncco[114], J. Song[127], A. Songmoolnak[118], F. Soramel[28], S. Sorensen[133], I. Sputowska[120], J. Stachel[107], I. Stan[69], P.J. Steffanic[133], S.F. Stiefelmaier[107], D. Stocco[117], I. Storehaug[20], M.M. Storetvedt[37], C.P. Stylianidis[93], A.A.P. Suaide[123], T. Sugitate[47], C. Suire[80], M. Suljic[35], R. Sultanov[95], M. Šumbera[98], V. Sumberia[104], S. Sumowidagdo[52], S. Swain[67], A. Szabo[13], I. Szarka[13], U. Tabassam[14], S.F. Taghavi[108], G. Taillepied[137], J. Takahashi[124], G.J. Tambave[21], S. Tang[137,7], Z. Tang[131], M. Tarhini[117], M.G. Tarzila[49], A. Tauro[35], G. Tejeda Muñoz[46], A. Telesca[35], L. Terlizzi[25], C. Terrevoli[127], G. Tersimonov[3], S. Thakur[143], D. Thomas[121], R. Tieulent[138], A. Tikhonov[65], A.R. Timmins[127], M. Tkacik[119], A. Toia[70], N. Topilskaya[65], M. Toppi[53], F. Torales-Acosta[19], T. Tork[80], R.C. Torres[82], S.R. Torres[38], A. Trifiró[33,57], S. Tripathy[55,71], T. Tripathy[50], S. Trogolo[35,28], G. Trombetta[34], V. Trubnikov[3], W.H. Trzaska[128], T.P. Trzcinski[144], B.A. Trzeciak[38], A. Tumkin[111], R. Turrisi[58], T.S. Tveter[20], K. Ullaland[21], A. Uras[138], M. Urioni[59,142], G.L. Usai[23], M. Vala[39], N. Valle[59,29], S. Vallero[61], N. van der Kolk[64], L.V.R. van Doremalen[64], M. van Leeuwen[93], P. Vande

Vyvre[35], D. Varga[147], Z. Varga[147], M. Varga-Kofarago[147], A. Vargas[46], M. Vasileiou[87], A. Vasiliev[91], O. Vázquez Doce[108], V. Vechernin[115], E. Vercellin[25], S. Vergara Limón[46], L. Vermunt[64], R. Vértesi[147], M. Verweij[64], L. Vickovic[36], Z. Vilakazi[134], O. Villalobos Baillie[113], G. Vino[54], A. Vinogradov[91], T. Virgili[30], V. Vislavicius[92], A. Vodopyanov[77], B. Volkel[35], M.A. Völkl[107], K. Voloshin[95], S.A. Voloshin[145], G. Volpe[34], B. von Haller[35], I. Vorobyev[108], D. Voscek[119], N. Vozniuk[65], J. Vrláková[39], B. Wagner[21], C. Wang[41], D. Wang[41], M. Weber[116], R.J.G.V. Weelden[93], A. Wegrzynek[35], S.C. Wenzel[35], J.P. Wessels[146], J. Wiechula[70], J. Wikne[20], G. Wilk[88], J. Wilkinson[110], G.A. Willems[146], B. Windelband[107], M. Winn[140], W.E. Witt[133], J.R. Wright[121], W. Wu[41], Y. Wu[131], R. Xu[7], S. Yalcin[79], Y. Yamaguchi[47], K. Yamakawa[47], S. Yang[21], S. Yano[47], Z. Yin[7], H. Yokoyama[64], I.-K. Yoo[17], J.H. Yoon[63], S. Yuan[21], A. Yuncu[107], V. Zaccolo[24], A. Zaman[14], C. Zampolli[35], H.J.C. Zanoli[64], N. Zardoshti[35], A. Zarochentsev[115], P. Závada[68], N. Zaviyalov[111], H. Zbroszczyk[144], M. Zhalov[101], S. Zhang[41], X. Zhang[7], Y. Zhang[131], V. Zherebchevskii[115], Y. Zhi[11], D. Zhou[7], Y. Zhou[92], J. Zhu[7,110], Y. Zhu[7], A. Zichichi[26], G. Zinovjev[3], N. Zurlo[142,59]

Affiliation Notes

[I] Deceased
[II] Also at: Italian National Agency for New Technologies, Energy and Sustainable Economic Development (ENEA), Bologna, Italy
[III] Also at: Dipartimento DET del Politecnico di Torino, Turin, Italy
[IV] Also at: M.V. Lomonosov Moscow State University, D.V. Skobeltsyn Institute of Nuclear, Physics, Moscow, Russia
[V] Also at: Institute of Theoretical Physics, University of Wroclaw, Poland

Collaboration Institutes

[1] A.I. Alikhanyan National Science Laboratory (Yerevan Physics Institute) Foundation, Yerevan, Armenia
[2] AGH University of Science and Technology, Cracow, Poland
[3] Bogolyubov Institute for Theoretical Physics, National Academy of Sciences of Ukraine, Kiev, Ukraine
[4] Bose Institute, Department of Physics and Centre for Astroparticle Physics and Space Science (CAPSS), Kolkata, India
[5] Budker Institute for Nuclear Physics, Novosibirsk, Russia
[6] California Polytechnic State University, San Luis Obispo, California, United States
[7] Central China Normal University, Wuhan, China
[8] Centro de Aplicaciones Tecnológicas y Desarrollo Nuclear (CEADEN), Havana, Cuba
[9] Centro de Investigación y de Estudios Avanzados (CINVESTAV), Mexico City and Mérida, Mexico
[10] Chicago State University, Chicago, Illinois, United States
[11] China Institute of Atomic Energy, Beijing, China
[12] Chungbuk National University, Cheongju, Republic of Korea
[13] Comenius University Bratislava, Faculty of Mathematics, Physics and Informatics, Bratislava, Slovakia
[14] COMSATS University Islamabad, Islamabad, Pakistan
[15] Creighton University, Omaha, Nebraska, United States
[16] Department of Physics, Aligarh Muslim University, Aligarh, India
[17] Department of Physics, Pusan National University, Pusan, Republic of Korea
[18] Department of Physics, Sejong University, Seoul, Republic of Korea

[19] Department of Physics, University of California, Berkeley, California, United States
[20] Department of Physics, University of Oslo, Oslo, Norway
[21] Department of Physics and Technology, University of Bergen, Bergen, Norway
[22] Dipartimento di Fisica dell'Università 'La Sapienza' and Sezione INFN, Rome, Italy
[23] Dipartimento di Fisica dell'Università and Sezione INFN, Cagliari, Italy
[24] Dipartimento di Fisica dell'Università and Sezione INFN, Trieste, Italy
[25] Dipartimento di Fisica dell'Università and Sezione INFN, Turin, Italy
[26] Dipartimento di Fisica e Astronomia dell'Università and Sezione INFN, Bologna, Italy
[27] Dipartimento di Fisica e Astronomia dell'Università and Sezione INFN, Catania, Italy
[28] Dipartimento di Fisica e Astronomia dell'Università and Sezione INFN, Padova, Italy
[29] Dipartimento di Fisica e Nucleare e Teorica, Università di Pavia, Pavia, Italy
[30] Dipartimento di Fisica 'E.R. Caianiello' dell'Università and Gruppo Collegato INFN, Salerno, Italy
[31] Dipartimento DISAT del Politecnico and Sezione INFN, Turin, Italy
[32] Dipartimento di Scienze e Innovazione Tecnologica dell'Università del Piemonte Orientale and INFN Sezione di Torino, Alessandria, Italy
[33] Dipartimento di Scienze MIFT, Università di Messina, Messina, Italy
[34] Dipartimento Interateneo di Fisica 'M. Merlin' and Sezione INFN, Bari, Italy
[35] European Organization for Nuclear Research (CERN), Geneva, Switzerland
[36] Faculty of Electrical Engineering, Mechanical Engineering and Naval Architecture, University of Split, Split, Croatia
[37] Faculty of Engineering and Science, Western Norway University of Applied Sciences, Bergen, Norway
[38] Faculty of Nuclear Sciences and Physical Engineering, Czech Technical University in Prague, Prague, Czech Republic
[39] Faculty of Science, P.J. Šafárik University, Košice, Slovakia
[40] Frankfurt Institute for Advanced Studies, Johann Wolfgang Goethe-Universität Frankfurt, Frankfurt, Germany
[41] Fudan University, Shanghai, China
[42] Gangneung-Wonju National University, Gangneung, Republic of Korea
[43] Gauhati University, Department of Physics, Guwahati, India
[44] Helmholtz-Institut für Strahlen- und Kernphysik, Rheinische Friedrich-Wilhelms-Universität Bonn, Bonn, Germany
[45] Helsinki Institute of Physics (HIP), Helsinki, Finland
[46] High Energy Physics Group, Universidad Autónoma de Puebla, Puebla, Mexico
[47] Hiroshima University, Hiroshima, Japan
[48] Hochschule Worms, Zentrum für Technologietransfer und Telekommunikation (ZTT), Worms, Germany
[49] Horia Hulubei National Institute of Physics and Nuclear Engineering, Bucharest, Romania
[50] Indian Institute of Technology Bombay (IIT), Mumbai, India
[51] Indian Institute of Technology Indore, Indore, India
[52] Indonesian Institute of Sciences, Jakarta, Indonesia
[53] INFN, Laboratori Nazionali di Frascati, Frascati, Italy
[54] INFN, Sezione di Bari, Bari, Italy
[55] INFN, Sezione di Bologna, Bologna, Italy
[56] INFN, Sezione di Cagliari, Cagliari, Italy
[57] INFN, Sezione di Catania, Catania, Italy
[58] INFN, Sezione di Padova, Padova, Italy
[59] INFN, Sezione di Pavia, Pavia, Italy
[60] INFN, Sezione di Roma, Rome, Italy
[61] INFN, Sezione di Torino, Turin, Italy

[62] INFN, Sezione di Trieste, Trieste, Italy
[63] Inha University, Incheon, Republic of Korea
[64] Institute for Gravitational and Subatomic Physics (GRASP), Utrecht University/Nikhef, Utrecht, Netherlands
[65] Institute for Nuclear Research, Academy of Sciences, Moscow, Russia
[66] Institute of Experimental Physics, Slovak Academy of Sciences, Košice, Slovakia
[67] Institute of Physics, Homi Bhabha National Institute, Bhubaneswar, India
[68] Institute of Physics of the Czech Academy of Sciences, Prague, Czech Republic
[69] Institute of Space Science (ISS), Bucharest, Romania
[70] Institut für Kernphysik, Johann Wolfgang Goethe-Universität Frankfurt, Frankfurt, Germany
[71] Instituto de Ciencias Nucleares, Universidad Nacional Autónoma de México, Mexico City, Mexico
[72] Instituto de Física, Universidade Federal do Rio Grande do Sul (UFRGS), Porto Alegre, Brazil
[73] Instituto de Física, Universidad Nacional Autónoma de México, Mexico City, Mexico
[74] iThemba LABS, National Research Foundation, Somerset West, South Africa
[75] Jeonbuk National University, Jeonju, Republic of Korea
[76] Johann-Wolfgang-Goethe Universität Frankfurt Institut für Informatik, Fachbereich Informatik und Mathematik, Frankfurt, Germany
[77] Joint Institute for Nuclear Research (JINR), Dubna, Russia
[78] Korea Institute of Science and Technology Information, Daejeon, Republic of Korea
[79] KTO Karatay University, Konya, Turkey
[80] Laboratoire de Physique des 2 Infinis, Irène Joliot-Curie, Orsay, France
[81] Laboratoire de Physique Subatomique et de Cosmologie, Université Grenoble-Alpes, CNRS-IN2P3, Grenoble, France
[82] Lawrence Berkeley National Laboratory, Berkeley, California, United States
[83] Lund University Department of Physics, Division of Particle Physics, Lund, Sweden
[84] Moscow Institute for Physics and Technology, Moscow, Russia
[85] Nagasaki Institute of Applied Science, Nagasaki, Japan
[86] Nara Women’s University (NWU), Nara, Japan
[87] National and Kapodistrian University of Athens, School of Science, Department of Physics , Athens, Greece
[88] National Centre for Nuclear Research, Warsaw, Poland
[89] National Institute of Science Education and Research, Homi Bhabha National Institute, Jatni, India
[90] National Nuclear Research Center, Baku, Azerbaijan
[91] National Research Centre Kurchatov Institute, Moscow, Russia
[92] Niels Bohr Institute, University of Copenhagen, Copenhagen, Denmark
[93] Nikhef, National institute for subatomic physics, Amsterdam, Netherlands
[94] NRC Kurchatov Institute IHEP, Protvino, Russia
[95] NRC «Kurchatov»Institute - ITEP, Moscow, Russia
[96] NRNU Moscow Engineering Physics Institute, Moscow, Russia
[97] Nuclear Physics Group, STFC Daresbury Laboratory, Daresbury, United Kingdom
[98] Nuclear Physics Institute of the Czech Academy of Sciences, Řež u Prahy, Czech Republic
[99] Oak Ridge National Laboratory, Oak Ridge, Tennessee, United States
[100] Ohio State University, Columbus, Ohio, United States
[101] Petersburg Nuclear Physics Institute, Gatchina, Russia
[102] Physics department, Faculty of science, University of Zagreb, Zagreb, Croatia
[103] Physics Department, Panjab University, Chandigarh, India
[104] Physics Department, University of Jammu, Jammu, India
[105] Physics Department, University of Rajasthan, Jaipur, India
[106] Physikalisches Institut, Eberhard-Karls-Universität Tübingen, Tübingen, Germany
[107] Physikalisches Institut, Ruprecht-Karls-Universität Heidelberg, Heidelberg, Germany

[108] Physik Department, Technische Universität München, Munich, Germany
[109] Politecnico di Bari and Sezione INFN, Bari, Italy
[110] Research Division and ExtreMe Matter Institute EMMI, GSI Helmholtzzentrum für Schwerionenforschung GmbH, Darmstadt, Germany
[111] Russian Federal Nuclear Center (VNIIEF), Sarov, Russia
[112] Saha Institute of Nuclear Physics, Homi Bhabha National Institute, Kolkata, India
[113] School of Physics and Astronomy, University of Birmingham, Birmingham, United Kingdom
[114] Sección Física, Departamento de Ciencias, Pontificia Universidad Católica del Perú, Lima, Peru
[115] St. Petersburg State University, St. Petersburg, Russia
[116] Stefan Meyer Institut für Subatomare Physik (SMI), Vienna, Austria
[117] SUBATECH, IMT Atlantique, Université de Nantes, CNRS-IN2P3, Nantes, France
[118] Suranaree University of Technology, Nakhon Ratchasima, Thailand
[119] Technical University of Košice, Košice, Slovakia
[120] The Henryk Niewodniczanski Institute of Nuclear Physics, Polish Academy of Sciences, Cracow, Poland
[121] The University of Texas at Austin, Austin, Texas, United States
[122] Universidad Autónoma de Sinaloa, Culiacán, Mexico
[123] Universidade de São Paulo (USP), São Paulo, Brazil
[124] Universidade Estadual de Campinas (UNICAMP), Campinas, Brazil
[125] Universidade Federal do ABC, Santo Andre, Brazil
[126] University of Cape Town, Cape Town, South Africa
[127] University of Houston, Houston, Texas, United States
[128] University of Jyväskylä, Jyväskylä, Finland
[129] University of Kansas, Lawrence, Kansas, United States
[130] University of Liverpool, Liverpool, United Kingdom
[131] University of Science and Technology of China, Hefei, China
[132] University of South-Eastern Norway, Tonsberg, Norway
[133] University of Tennessee, Knoxville, Tennessee, United States
[134] University of the Witwatersrand, Johannesburg, South Africa
[135] University of Tokyo, Tokyo, Japan
[136] University of Tsukuba, Tsukuba, Japan
[137] Université Clermont Auvergne, CNRS/IN2P3, LPC, Clermont-Ferrand, France
[138] Université de Lyon, CNRS/IN2P3, Institut de Physique des 2 Infinis de Lyon , Lyon, France
[139] Université de Strasbourg, CNRS, IPHC UMR 7178, F-67000 Strasbourg, France, Strasbourg, France
[140] Université Paris-Saclay Centre d'Etudes de Saclay (CEA), IRFU, Départment de Physique Nucléaire (DPhN), Saclay, France
[141] Università degli Studi di Foggia, Foggia, Italy
[142] Università di Brescia, Brescia, Italy
[143] Variable Energy Cyclotron Centre, Homi Bhabha National Institute, Kolkata, India
[144] Warsaw University of Technology, Warsaw, Poland
[145] Wayne State University, Detroit, Michigan, United States
[146] Westfälische Wilhelms-Universität Münster, Institut für Kernphysik, Münster, Germany
[147] Wigner Research Centre for Physics, Budapest, Hungary
[148] Yale University, New Haven, Connecticut, United States
[149] Yonsei University, Seoul, Republic of Korea